2012

Numerical simulation of electric double layers in a helicon plasma device

Sathyanarayan N. Rao

NUMERICAL SIMULATION OF ELECTRIC DOUBLE LAYERS IN A HELICON PLASMA DEVICE

by

SATHYANARAYAN N. RAO

A THESIS

Submitted in partial fulfillment of the requirements
for the degree of Master of Science in Engineering
in
The Department of Electrical and Computer Engineering
to
The School of Graduate Studies
of
The University of Alabama in Huntsville

HUNTSVILLE, ALABAMA

2012

In presenting this thesis in partial fulfillment of the requirements for a master's degree from The University of Alabama in Huntsville, I agree that the Library of this University shall make it freely available for inspection. I further agree that permission for extensive copying for scholarly purposes may be granted by my advisor or, in his/her absence, by the Chair of the Department or the Dean of the School of Graduate Studies. It is also understood that due recognition shall be given to me and to The University of Alabama in Huntsville in any scholarly use which may be made of any material in this thesis.

Nirav

(student signature)

04/11/2012

(date)

THESIS APPROVAL FORM

Submitted by Sathyanarayan N. Rao in partial fulfillment of the requirements for the degree of Master of Science in Engineering in Electrical Engineering and accepted on behalf of the Faculty of the School of Graduate Studies by the thesis committee.

We, the undersigned members of the Graduate Faculty of The University of Alabama in Huntsville, certify that we have advised and/or supervised the candidate on the work described in this thesis. We further certify that we have reviewed the thesis manuscript and approve it in partial fulfillment of the requirements for the degree of Master of Science in Engineering in Electrical Engineering.

May 11, 2012
Committee Chair
(Date)

4/11/2012

4/12/12

4/19/12 Department Chair

College Dean

Rhonda Kay Faede 5/7/12 Graduate Dean

ABSTRACT

The School of Graduate Studies
The University of Alabama in Huntsville

Degree: Master of Science in Engineering College/Dept: Engineering/Electrical and Computer Engineering

Name of Candidate: Sathyanarayan N. Rao

Title: Numerical Simulation of Electric Double Layers in a Helicon Plasma Device

We have studied formation of Current Free Double Layers (CFDLs) in a highly diverging magnetic field by means of two-dimensional electrostatic particle in cell simulations. This study is motivated by laboratory experiments on CFDLs in Helicon Plasma Device. Since CFDLs accelerate ions, the experimental work has led to design of a new generation of plasma thrusters known as Helicon Double Layer Thrusters. CFDL structure consists of U-shaped equipotentials and a conical plasma density structures. The physical processes leading to these structures are critically studied. We found that the difference in the magnetization of electrons and ions in the plasma plays key role in the generation of the density and potential structures. Features of ion acceleration responsible for thrust generation are studied. The potential and the density structures and the electric field strengths in the CFDL are in good agreements with the laboratory experiments.

Abstract Approval: Committee Chair _____ April 11, 2012

Department Chair _____ 4/19/12

Graduate Dean _____ Rhonda Kay Shede 5/7/12

ACKNOWLEDGMENTS

The work described in this thesis would not have been possible without the assistance of a number of people who deserve special mention. First, I would like to thank Dr. Nagendra Singh for his suggestion of the research topic and for his guidance throughout all the stages of the work. I would like to thank Dr. Reza Adhami and Dr. Mark Tillman for serving as my thesis committee member.

I thank Salmon Library for proving me access to the books and journals that were very useful in completing this work.

This work was made possible in part by a grant of high performance computing resources and technical support from the Alabama Supercomputer Authority. This work was also financially supported by a NSF grant ATM0647157.

Finally, I am thankful to my parents for their support.

TABLE OF CONTENTS

Page

List of Figures viii
List of Tables xii
List of Symbols xiii
CHAPTER
1 INTRODUCTION 1
1.1 INTRODUCTION 1
1.2 THESIS OBJECTIVE 3
1.3 ORGANIZATION OF THESIS 3
2 THEORITICAL BACKGROUND 5
2.1 PLASMA BASICS 5
2.2 PARTICLE RESPONSE TO STATIC FIELDS 8
2.3 ELECTRIC DOUBLE LAYERS IN PLASMAS 9
2.4 HELICON PLASMA DEVICE AT ANU 11
3 NUMERICAL IMPLEMENTATION 13
3.1 GEOMETRY OF THE PROBLEM 13
3.2 NORMALIZATION IN PIC SIMULATION 14
3.3 PARTICLE IN CELL ALGORITHM 17
3.4 MAGNETIC FIELD CALCULATION 19
3.5 CHARGE DENSITY CALCULATION 24
3.6 POISSON SOLVER 26
3.7 ELECTRIC FIELD COMPUTATION 28
3.8 PARTICLE MOVER 29
3.9 SIMULATION PARAMETERS AND INITIAL CONDITIONS 30
4 NUMERICAL RESULTS 31
4.1 SIMULATION RESULTS 31
4.2 VARYING THE DIVERGENCE OF MAGNETIC FIELD 52

4.3 VARYING THE WIDTH OF PIW 55
4.4 COMPARISONS WITH ANU EXPERIMENTS 57

5 CONCLUSIONS 63
5.1 DISCUSSION AND CONCLUSION 63
5.2 RECOMMENDATIONS FOR FUTURE WORK 65
APPENDIX A: 2D ELECTROSTATIC PIC CODE 66
APPENDIX B: ELECTRON ENERGY DISTRIBUTION M-FILE 91
REFERENCES 93

LIST OF FIGURES

Page

Figure

2.1 Schematic picture of a double layer 10

2.2 Electric potential and electric field distribution through a double layer 10

2.3 Simplified schematic of a HPD 12

3.1 Simulation geometry 13

3.2 Particle-in-Cell algorithm 19

3.3 Magnetic field calculation using Biot Savart's law 20

3.4 Weighting scheme used for magnetic field 22

3.5 B_X in the simulation box ($N_X = N_Z = 201$, w=60 and r=66) 23

3.6 B_Z in the simulation box ($N_X = N_Z = 201$, w=60 and r=66). 24

3.7 Distribution of charge density 25

3.8 Five point stencil for solving Poisson equation. 26

3.9 Boundary conditions ($N_X = N_Z = 201$ and w=60) 28

4.1 Equipotential contour map of ϕ at t=11300 ω_{pe}^{-1} 33

4.2 $\phi(X = 0, Z)$ at t=11300 ω_{pe}^{-1} 33

4.3 Contour map of $E_\perp$ at t=11300 ω_{pe}^{-1} 34

4.4 $E_\perp$ (X, Z=20) at t=11300 ω_{pe}^{-1} 34

4.5 Color map of ion density n_i at t=11300 ω_{pe}^{-1} 35

4.6 Color map of electron density n_e at t=11300 ω_{pe}^{-1} 35

4.7 (a) $n_i(X)$ along Z = 5, 10, 50, 100, and175 and (b) integral of $n_i(X)$ and $n_e(X)$ (dashed line) for 20<Z<150. 36

4.8 Time history of electric potential ϕ at selected points. 38

4.9 Frequency spectrum of $\phi(t)$: (a) before reaching steady state and (b) after reaching steady state. 39

4.10 (a) $\phi(t)$ at X=0,Z=5 for 0<t<13500 ω_{pe}^{-1} , (b) $\phi(t)$ at X=0,Z=5 for 12800<t<13000 ω_{pe}^{-1} and (c) Frequency spectrum of Figure 4.10 (b). 40

4.11 Evolution of electric potential ϕ at different times. Left panels show color map of ϕ and right panels show axial profile of ϕ at X=0. 42

4.12 Comparison of instantaneous electric potential ϕ (left panels) and averaged electric potential ϕ_a (right panels) at different times. 43

4.13 Spatial distribution of electrons and ions before reaching steady state. 44

4.14 Spatial distribution of electrons and ions after reaching steady state. 45

4.15 Z-V_X phase plot for (a) electrons and (b) ions at t=13000 ω_{pe}^{-1} for |X|<30. 47

4.16 X-V_X phase plot for ions (blue) and electrons (red) at different axial regions. 49

4.17 Z-V_Z phase plot for ions (blue) and electrons (red) at different times for the region |X|<10. 50

4.18 X-V_Z phase plot for ions (blue) and electrons (red) at different times for the region |X|<10. 51

4.19 Comparison of V_Z -V_X phase space for ions in the region (a) below the DL (0 < Z < 50), (b) above the DL (80 < Z < 120); both for | X| < 10. 52

4.20 ϕ for high divergence in magnetic field $(N_X = N_Z = 100)$. 53

4.21 n_i for high divergence in magnetic field $(N_X = N_Z = 100)$. 54

4.22 ϕ for low divergence in magnetic field $(N_X = N_Z = 100)$. 54

4.23 n_i for low divergence in magnetic field $(N_X = N_Z = 100)$. 55

4.24 (a) Color map of ϕ for w=40 at t=11300 and (b) $\phi(X = 0, Z)$ 56

4.25 (a) Color map of ϕ for w=60 at t=11300 and (b) $\phi(X = 0, Z)$ 56

4.26 Equipotential contours observed in the Helicon Plasma Device. Reprinted Figure 2 with permission from C. Charles, High density conics in a magnetically expanding helicon plasma, Vol. 96, 051502, 2010. Copyright 2010, American Institute of Physics.....58

4.27 Equipotential contour map of ϕ near the PIW. 59

4.28 Contours of ion density observed in the HPD. Reprinted Figure3 with permission from C. Charles, High density conics in a magnetically expanding helicon plasma, Vol. 96, 051502, 2010. Copyright 2010, American Institute of Physics... 60

4.29 Radial electric field derived from the measured electric potential. Reprinted Figure 4(b) with permission from [C. Charles, R.W. Boswell and R. Hawkins, Oblique Double Layers: A Comparison between Terrestrial and Auroral Measurements, PRL 103, 095001, 2009]. Copyright (2009) by the American Physical Society. ... 60

4.30 Parallel Electric Field derived from the measured Electric Potential. Reprinted Figure 4(d) with permission from [C. Charles, R.W. Boswell and R. Hawkins, Oblique Double Layers: A Comparison between Terrestrial and Auroral Measurements, PRL 103, 095001, 2009]. Copyright (2009) by the American Physical Society. 61

4.31 (a) $\phi(X, Z = 10)$,(b) $E_{\perp}(X, Z = 10)$,(c) $\phi(X = 0, Z)$ and (d) $E_Z(X = 0, Z)$; all at time=11300 ω_{pe}^{-1} 61

4.32 Electron energy distribution functions at the surface of the cone (30 < X <50 and 30 < Z < 70) for w=60, d=65 and $N_X = N_Z = 201$. 62

4.33 Electron Energy Distribution in the high density conic. Reprinted Figure 4 with permission from C. Charles, High density conics in a magnetically expanding helicon plasma, Vol. 96, 051502, 2010. Copyright 2010, American Institute of Physics..... 62

LIST OF TABLES

Page

Table

3.1 Simulation parameters and initial conditions..... 30

LIST OF SYMBOLS

B: Magnetic field vector

ϕ : Electric Potential

N_x: Number of grids in X-axis

N_z: Number of grids in Z-axis

w: Width of the Plasma Injection Window

r: Radius of the solenoid

$E_\perp$: Radial or Perpendicular Electric field

E_Z : Axial Electric Field

B_X: X-component of the Magnetic Field

B_Z: Z-component of the Magnetic Field

n_i : Normalized Ion Density

n_e : Normalized Electron Density

PIW: Plasma Injection Window

DL: Double Layer

HPD: Helicon Plasma Device

HDLT: Helicon Double Layer Thruster

t: time

V_X: Radial Velocity Component

V_Z: Axial Velocity Component

λ_{do} : Plasma Debye Length

V_T : Thermal Velocity of the particle

V_{Ti} : Ion Thermal Velocity

T_e : Electron Temperature

ω_{pe} : Electron Plasma Frequency

V_{Te} : Electron Thermal Velocity

T_i : Ion Temperature

PIC: Particle-in-Cell

Δt : Time Step

CHAPTER 1

INTRODUCTION

1.1 INTRODUCTION

A plasma thruster offers promising features such as low fuel consumption and high exhaust velocity, which are essential for long duration space travel. These features can reduce the round trip flight time of a spacecraft during interplanetary missions. Plasma thrusters rely on electric power which can be produced in space by a solar array or a nuclear reactor.

In 2003, Charles and Boswell found that the expansion of plasma in the Helicon Plasma Device (HPD) creates an electric potential structure which then accelerates ions in axial direction producing net thrust [4, 5]. The electric potential structure which accelerates charged particles is referred as Double Layer (DL). Similar experiments on the plasma expansion in HPD also reported Double Layers [6, 7]. This discovery of Double Layer in the Helicon Plasma Device by Charles and Boswell led to the development of a new type of electrode-less plasma thruster known as Helicon Double Layer Thruster (HDLT).

In this thesis, we study the kinetic processes that lead to double layer formation in HPD [4, 5]. HPD uses radio frequency electromagnetic waves to ionize neutral gas to form plasma. Plasma is then allowed to expand into a wider geometry in the presence of

a diverging magnetic field. The expansion of plasma in the diverging magnetic field creates an electric potential structure interpreted as double layer. Double layer, thus formed accelerates ions to supersonic velocities.

The HDLT is a low thrust device [8], but its features like requiring no electrodes and capability of working with hydrogen and carbon dioxide as the propellant gas makes it very distinct. Based on the work of Charles and Boswell, a prototype thruster was built by Australian National University group, and was tested in CORONA space simulation chambers at the European Space Agency development center [5].

The Double layers in HPD were first detected by the one–dimensional measurements of the axial profiles of potential and density and the ion beam velocity distribution functions on the low potential side of the DL [4]. These one-dimensional measurements led to the theoretical explanation for the DL formation as seen in [11] and [12]. Charles suggested that DL forms in the HPD due to a reduction in plasma density when the dense plasma generated in the source chamber expands into the diffusion chamber. Simulations based on density reduction scheme were performed [13, 21]. Recent measurements by Charles show that the plasma density in the HPD is in the shape of cone and the electric potential has a U-shaped structure [3, 14]. Prior one-dimensional simulation failed to account for these variations in density and electric potential. These two-dimensional measurement indicates that plasma expansion modeled by density reduction schemes as in [13, 21] is insufficient to describe the physics of DL formation in HPD. Based on two-dimensional measurements by Charles, Singh pointed out the significance of difference in motion of electrons and ions due to diverging magnetic field [1, 2]. He suggested that magnetized electrons move along the diverging magnetic field and unmagnetized ions

tend to move straight, thus, creating radial charge separation and radial electric fields. He pointed out that the generation of radial electric field is the source of DL formation in the HPD [1].

Even though HDLT is a successful device, the mechanism of DL formation is not clearly understood. Therefore, we attempt to understand the physics of DL formation in the HPD by performing a two-dimensional computer simulation. HPD is a cylindrical geometry, but we simulate the plasma flow in Cartesian coordinate system. This approximation will not change the basic physics involved in the HPD such as conical density structure and U-shaped Double Layer formation.

1.2 THESIS OBJECTIVE

The main objective of this thesis is to understand the basic physics involved in the formation of DL in the HPD. To simulate the plasma, we adopt particle-in-cell (PIC) method which is described in Chapter 3. We treat electrons and ions as macro particles having Maxwellian distribution. We assume that plasma is collisionless and electrostatic. This allows us to use electrostatic PIC code. Finite difference method is adopted to solve Poisson's equation. Diverging magnetic field of a solenoid is calculated using Biot Savart's law. All the quantities in the simulation are normalized as described in Chapter 3.

1.3 ORGANIZATION OF THESIS

The remaining part of this thesis report is organized as follows. Chapter 2 presents theoretical background. The numerical methods and algorithms used in the computer

code are described in Chapter 3. Numerical results of our simulation are presented in Chapter 4. Chapter 5 contains summary of this work, concluding remarks, and the recommendations for the future work.

CHAPTER 2

THEORITICAL BACKGROUND

2.1 PLASMA BASICS

At sufficiently high temperatures, atoms and molecules decompose into positive ions and negative electrons giving rise to an electrified gas. This electrified gas is called plasma in physics, if it satisfies the following two conditions:

- It must be quasi neutral which means, number of ions should be equal to number of electrons.
- Its movement should be predominantly controlled by electric and magnetic forces rather than ordinary collisions. Hence it should have more ionized particles than neutral particles.

Each particle in the plasma is controlled simultaneously by large number of other particles by long range coulomb forces. This is known as collective behavior of plasma [15]. Only when particle density is high enough and collective behavior are observed, we can call the ionized gas as plasma. The amount of atoms or molecules ionized in thermal equilibrium is given by the Saha equation:

$$\frac{n_{Io}}{n_n} \approx 2.4 \times 10^{21} \times \frac{T^{3/2}}{n_{Io}} e^{-U_{Io}/KT} \tag{2.1}$$

We can easily observe that if the temperature is sufficiently high, then n_{Io} outnumber n_n. Since much of the matters in the observable universe are at the temperatures of millions of degrees, it is often said that, plasma constitutes about 95% of the total matter in the known universe. Naturally existing terrestrial plasma is very rare since temperature of a planet is much colder compared to that of a star.

There are few parameters that are essential in understanding plasma mechanism and are discussed as follows:

- Any external perturbation in the plasma medium such as a charge separation creates oscillations in electrons and ions. Frequency at which electrons oscillate is known as electron plasma frequency and is much higher than the frequency at which ions oscillate. Electron plasma frequency ω_{pe} is given by

$$\omega_{pe} = \sqrt{\left(\frac{ne^2}{m\varepsilon_0}\right)}, \tag{2.2}$$

  where n is the plasma density, that is, number of electrons or ions found in volume of $1\, meter^3$, m is the mass of electron, e is the charge of electron, and ε_0 is the permittivity of free space. Plasma oscillation will only be observed, if the plasma is studied over time period longer than the plasma period $\tau_p = 1/\omega_{pe}$ and if external actions change the system at a rate much slower than ω_{pe}.

- Particle speed in the plasma medium is commonly described by Maxwell-Boltzmann distribution given by

$$f(v_x, v_y, v_z) = \left(\frac{n_0 m}{2\pi KT}\right)^{1.5} \exp\left(\frac{-m(v_x{}^2 + v_y{}^2 + v_z{}^2)}{2KT}\right), \tag{2.3}$$

where v_x, v_y, v_z are the velocity components along x , y and z coordinates, K is the Boltzmann constant , m is the mass of the particle , T is the temperature in Kelvin and n is the plasma density. Equation (2.3) in one-dimensional form is given by

$$f(u) = \sqrt{\frac{nm}{2\pi KT}} \exp\left(\frac{-mu^2}{2KT}\right). \tag{2.4}$$

- Thermal speed of a particle is given by

$$V_T = \sqrt{\frac{KT}{m}}. \tag{2.5}$$

Ion thermal speed V_{Ti} is related to electron thermal speed V_{Te} by

$$V_{Ti} = \sqrt{\frac{m_e}{m_i}} V_{Te}, \tag{2.6}$$

where m_e is the mass of the electron and m_i is the mass of the ion.

- The distance by which particles in the plasma medium travels with the thermal velocity V_T in time=$1/\omega_{pe}$ is called the Debye length denoted by λ_d and is given by

$$\lambda_d = \frac{V_T}{\omega_{pe}} = \sqrt{\frac{\varepsilon_0 KT}{ne^2}}. \tag{2.7}$$

Any electric potential applied externally to plasma is shielded by charge movements. This is known as Debye shielding. Debye length can also be thought

as a measure of this shielding distance. Since Debye length is same for electrons and ions, it is referred as the characteristic length of the plasma medium.

2.2 PARTICLE RESPONSE TO STATIC FIELDS

In this section, we will consider the motion of charged particles in presence of electric and magnetic fields that are stationary in time. Further, we assume that the magnetic field is prescribed and is not affected by the movement of charged particles.

The force F acting on a charged particle of charge q and mass m in an electric field E and magnetic field B is given by Lorentz force equation,

$$F = m\frac{dv}{dt} = q(E + v \times B) \qquad ; \; v \ll c, \tag{2.8}$$

where v is the instantaneous velocity of the particle , c is the velocity of light in vacuum, and $\times$ represents the vector cross product. From Equation 2.8, we can notice that force due to E on the charged particle is in the direction of E and because of the vector cross product, force due to B on the charged particle is in the direction perpendicular to B. Charged particles experience acceleration in presence of electric field alone and exhibits gyration in presence of magnetic field alone. The frequency of gyration of the particle around the magnetic field B is known as cyclotron frequency ω_c and is given by

$$\omega_c = \frac{|q|B}{m}, \tag{2.9}$$

where q is the charge of the particle and m is the mass of the particle. The radius of such gyration is called Larmor radius and is given by

$$r_L = \frac{mV_\perp}{|q|B}, \tag{2.10}$$

where $V_\perp$ is the velocity of the particle in the plane perpendicular to B. If B is in Z-direction, then $V_\perp = \sqrt{V_X{}^2 + V_Y{}^2}$, where V_X and V_Y are the velocity in X and Y direction. Electrons have smaller Larmor radius compared to ions due to its lighter weight. Electrons and ions gyrate in opposite sense. Direction of gyration is always such that the magnetic field generated by the charged particle is opposite to the externally imposed field making plasma, a diamagnetic medium. However, if the externally imposed magnetic field is stronger than the magnetic field generated by the particles, then the diamagnetic effect can be ignored.

2.3 ELECTRIC DOUBLE LAYERS IN PLASMAS

Electric double layer is a structure in plasma where there is a jump in the profile of electric potential as shown in Figure 2.2. The jump in electric potential is caused due to the localized charge separation. In other words, we can define an electric double layer as two parallel layers of positive and negative space charge in the plasma medium that sustains localized electric field as shown in Figure 2.1. Electric double layers provide the mechanism for the acceleration of particles in the plasma medium. Double layers play a significant role in auroral research and are thought to be responsible for the acceleration

of electrons in the upper atmosphere creating aurora [16]. Double layers are also been reported in the laboratory experiments such as in HPD [3].

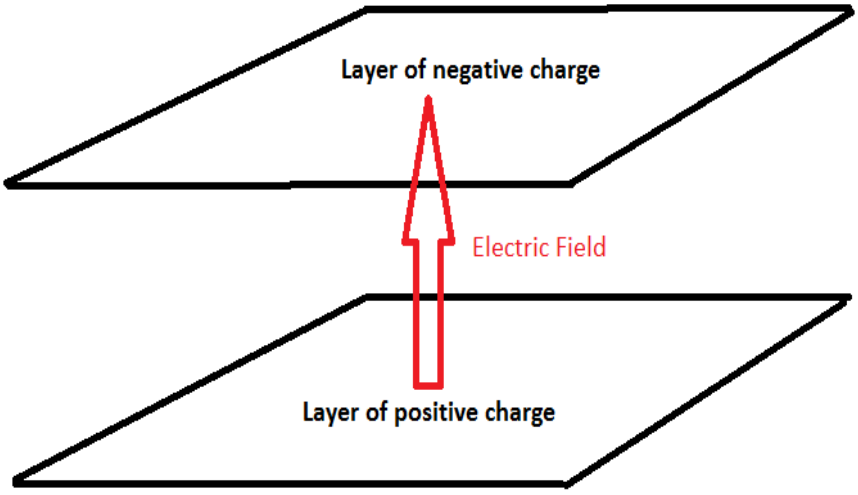

Figure 2.1: Schematic picture of a double layer

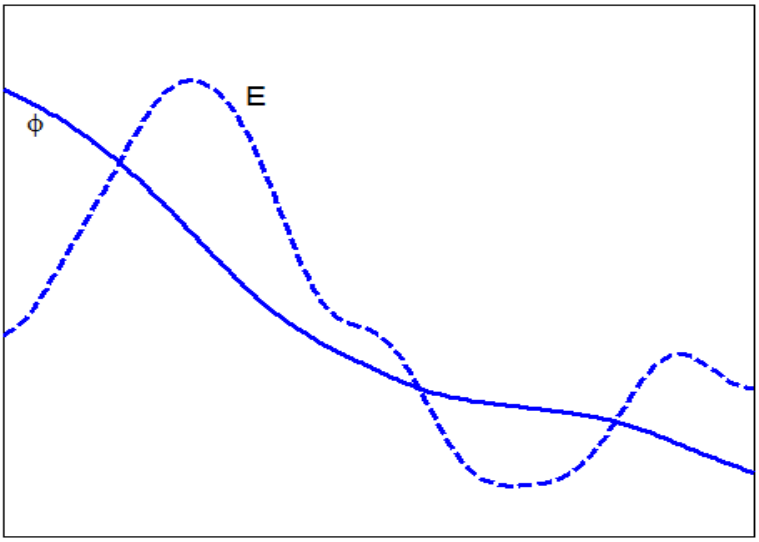

Figure 2.2: Electric potential and electric field distribution through a double layer

Bohm obtained condition for a double layer to exist inside quasi neutral plasma. This condition is known as Bohm sheath condition [15]. According to this condition, ions

entering the double layer must have a velocity greater than the acoustic velocity V_s. The acoustic velocity is given by $V_s = (KT_e / m_i)^{0.5}$, where T_e is the electron temperature, m_i is the mass of ion and, K is the Boltzmann constant. Thus if the ions entering the double layer has a mean velocity u_0, then for the DL to form, we need

$$u_0 > (KT_e / m_i)^{0.5}. \tag{2.11}$$

Double layers can be classified as strong or weak depending on the potential drop ϕ_{DL}. If $e\phi_{DL} / KT_e < 1$, then double layers are referred as weak. If $e\phi_{DL} / KT_e > 1$, then such double layers are referred as strong. Here, e is the electron charge, T_e is the electron temperature and, K is the Boltzmann constant. Double layers can be current driven or current free. In current driven double layers, ions and electrons accelerate in opposite direction producing net current across the double layer. However in current free double layers, there is no net current or very little current across the double layer [1].

2.4 HELICON PLASMA DEVICE AT ANU

Helicon plasma device use helicon waves to ionize the neutral gas to form plasma [4]. Low frequency electromagnetic waves in plasma that exist in presence of magnetic field are known as helicon waves. In this device, helicon waves are produced using helical antenna which is wrapped around the glass source chamber as shown in Figure 2.3. Plasma suddenly expands from a narrow glass source tube to wider expansion chamber in presence of a diverging magnetic field, forming current free double layer near the throat as indicated by curved solid line (Figure 2.3). Current free double layer was discovered in

this device by Charles and Boswell [4]. Their experimental set up consisted of two regions. First region was the source tube made up of Pyrex glass where carbon dioxide gas gets ionized by helicon waves. It is followed by second region known as metal expansion chamber made up of aluminum. Metal expansion chamber is earthed and hence will have zero electric potential. Two solenoids placed around the glass source chamber produce magnetic field which is uniform in source chamber and highly divergent in the metal expansion chamber as indicated by the dotted lines in Figure 2.3.

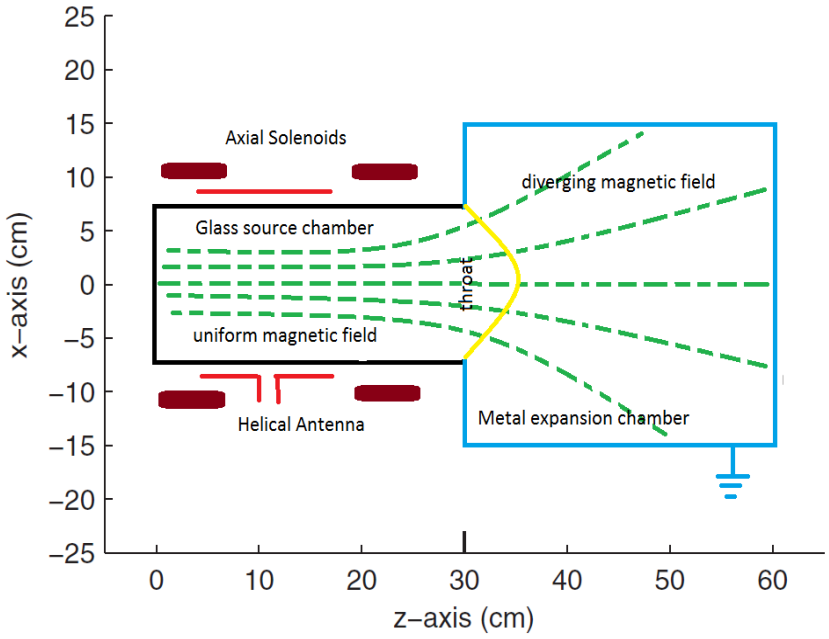

Figure 2.3: Simplified schematic of a HPD

CHAPTER 3

NUMERICAL IMPLEMENTATION

3.1 GEOMETRY OF THE PROBLEM

In our simulations, expansion region of HPD is referred as simulation box and plasma is injected into the simulation box through the plasma injection window (PIW) as shown in Figure3.1. The plasma injected through the PIW expands in the simulation box in presence of a diverging magnetic field. Diverging magnetic field is produced by a solenoid.

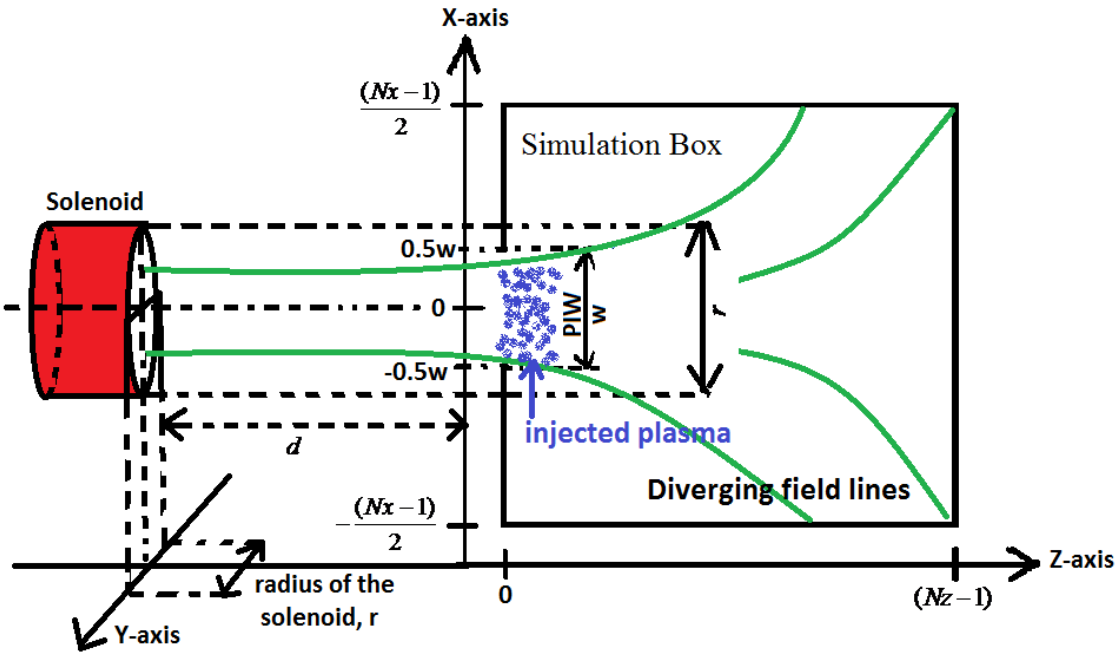

Figure 3.1: Simulation geometry

The simulated plasma occupies the region $0<Z/\lambda_{do}<N_Z$ and $-0.5(N_X-1) <X/ \lambda_{do}<0.5(N_X-1)$, where λ_{do} is the plasma Debye length near the PIW. The PIW occupies the region $-w/2 <X/ \lambda_{do}<w/2$. Radius of the solenoid is r and it consists of eighteen coils with spacing of $0.1\,\lambda_{do}$. In the simulations, we have two dimensions in space (X, Z) and three dimensions in velocity (V_X, V_Y, V_Z). This kind of simulation is said to be in 2.5 dimensions.

3.2 NORMALIZATION IN PIC SIMULATION

Physical quantities in the PIC simulation are usually normalized to reduce simulation time and numerical errors. Normalization replaces the physical quantities in the SI units to non dimensional quantities. Simulation results can be easily un-normalized to get back the physical results. In this section, normalized quantities are represented by tilde superscript.

Mass is normalized by the mass of electron m_e as given by

$$\widetilde{m_e} = \frac{m_e}{m_e} = 1, \tag{3.1}$$

$$\widetilde{m_i} = \frac{m_i}{m_e}. \tag{3.2}$$

Charge q is normalized by elementary charge e as given by

$$\tilde{q} = \frac{q}{e}. \tag{3.3}$$

Hence normalized charge of electron is -1 and normalized charge of ion is +1.

Length is normalized by plasma Debye length near the PIW denoted by λ_{do}. Hence spatial coordinates are given by

$$\widetilde{X} = \frac{X}{\lambda_{do}}, \widetilde{Y} = \frac{Y}{\lambda_{do}}, \widetilde{Z} = \frac{Z}{\lambda_{do}}. \tag{3.4}$$

Time t is normalized by the electron plasma frequency ω_{pe} as given by

$$\tilde{t} = t\omega_{pe}. \tag{3.5}$$

Velocity V is normalized by thermal velocity as given by

$$\widetilde{V} = \frac{V}{\sqrt{\frac{KT}{m}}}. \tag{3.6}$$

Plasma density n is normalized by undisturbed plasma density n_0 as given by

$$\tilde{n} = \frac{n}{n_0}. \tag{3.7}$$

Charge density ρ is normalized by reference charge density as given by

$$\tilde{\rho} = \frac{\rho}{en_0}. \tag{3.8}$$

Normalization of electric potential, ϕ is given by

$$\tilde{\phi} = \frac{e}{KT_e}\phi. \tag{3.9}$$

Normalization of Poisson equation is given by

$$\nabla^2 \tilde{\phi} = -\tilde{\rho}. \tag{3.10}$$

Electric field E which is given in Volt/meter, is normalized as

$$\tilde{E} = \frac{e}{KT_e \lambda_{do}} E. \tag{3.11}$$

Ambient magnetic field B is normalized as

$$\tilde{B} = \frac{e}{m_e \omega_{pe}} B. \tag{3.12}$$

The normalized equation of motion for the electrons becomes

$$\frac{\widetilde{dV}_X}{\widetilde{dt}} = -(\tilde{E}_X + \tilde{V}_Y \times \tilde{B}_Z), \tag{3.13}$$

$$\frac{\widetilde{dV}_Y}{\widetilde{dt}} = -(\tilde{E}_Y + \tilde{V}_Z \times \tilde{B}_X), \text{ and} \tag{3.14}$$

$$\frac{\widetilde{dV}_Z}{\widetilde{dt}} = -(\tilde{E}_Z + \tilde{V}_X \times \tilde{B}_Y). \tag{3.15}$$

Similarly, normalized equation of motion for ions become

$$\frac{\widetilde{dV}_X}{\widetilde{dt}} = -\frac{\widetilde{m_e}}{\widetilde{m_i}}(\widetilde{E}_X + \widetilde{V}_Y \times \widetilde{B}_Z), \tag{3.16}$$

$$\frac{\widetilde{dV}_Y}{\widetilde{dt}} = -\frac{\widetilde{m_e}}{\widetilde{m_i}}(\widetilde{E}_Y + \widetilde{V}_Z \times \widetilde{B}_X), \text{ and} \tag{3.17}$$

$$\frac{\widetilde{dV}_Z}{\widetilde{dt}} = -\frac{\widetilde{m_e}}{\widetilde{m_i}}(\widetilde{E}_Z + \widetilde{V}_X \times \widetilde{B}_Y). \tag{3.18}$$

3.3 PARTICLE IN CELL ALGORITHM

There are various ways to model plasma dynamics depending on the plasma density and the type of problem. Plasma can either be modeled as a fluid or as a collection of discrete particles. In particle approach, we treat plasma as a collection of many microscopic charged particles. Equation of motion is solved for each particle. In general, any code which solves the equation of motion for all the plasma particles (electrons and ions) is called a particle in cell (PIC) code. Electromagnetic PIC code solves whole set of Maxwell's equations while electrostatic PIC code just solves the Poisson equation.

In the PIC simulation, plasma is assumed to be made up of large number of macro particles. Each macro particle represents large number of real plasma particles. The number of real particles in the plasma is extremely large, making PIC simulation impossible even for the best super computers. Therefore, in the PIC simulation, macro particles are simulated instead of real particle. One macro particle may represent millions

of real particle. Macro particle follows the same path as the corresponding real particle because; the ratio of charge to mass is conserved. As a result, plasma simulated via macro particles behaves identical to the plasma simulated via real particle. Equation of motion is solved for each macro particle followed by the charge density and electric field calculations. The part of the code which solves equation of motion should be accurate and fast. One example for such solver is the leap frog method which is adopted in this thesis. Leap frog method is a numerical scheme used to compute particle velocity and position by solving Eq. 3.13 to 3.18.

The PIC code used in this thesis has absorbing boundary condition all along the boundaries of the simulated domain. In absorbing boundary condition, particles that cross the boundaries of the simulation box are removed from the simulation memory. The macro particles are put into the simulation box through particle injection. Injected macro particles are assumed to have Maxwellian distribution in their velocities.

Self induced magnetic field generated by the plasma particle is so low enough to ignore the diamagnetic property of the plasma. We also ignore any time varying electric field generated by the particles. By doing so, we are allowed to use electrostatic code. The PIC algorithm used in our simulations consists of following steps as shown in Figure 3.2.

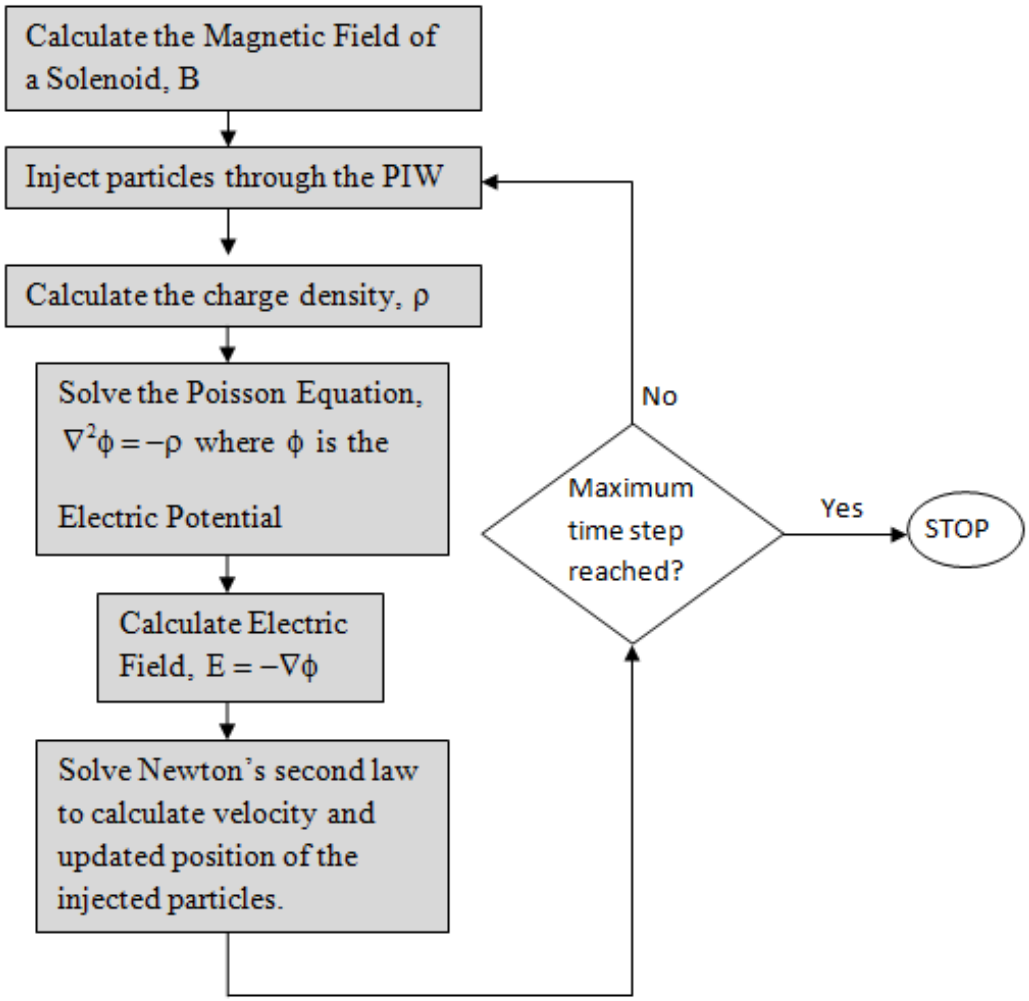

Figure 3.2: Particle-in-Cell algorithm

3.4 MAGNETIC FIELD CALCULATION

Diverging magnetic field of a solenoid is imposed in the simulation box as shown in Figure 3.1. Solenoid is a current carrying wire wound into a helix. If the pitch of the helix is small, then the magnetic field of a solenoid is approximately equal to the magnetic field produced by N circular coils of radius same as that of the helix , where N is the number of turns in the helix. In our simulation, circular coil is approximated by a polygon having 250 sides. Each side of the polygon is treated as a straight wire carrying

current. Then, magnetic field due to a circular coil is approximately equal to magnetic field produced by 250 straight wires arranged in the form of polygon. Magnetic field produced by each side of the polygon is calculated using Biot Savart's law.

Let us denote sides of the polygon by s_i, i=1 to 250. In Figure 3.3, first two sides of the polygon with its coordinates are shown. Coordinates (x_{m1}, y_{m1}, z_{m1}) and (x_{m2}, y_{m2}, z_{m2}) represents the mid points of s_1 and s_2 respectively.

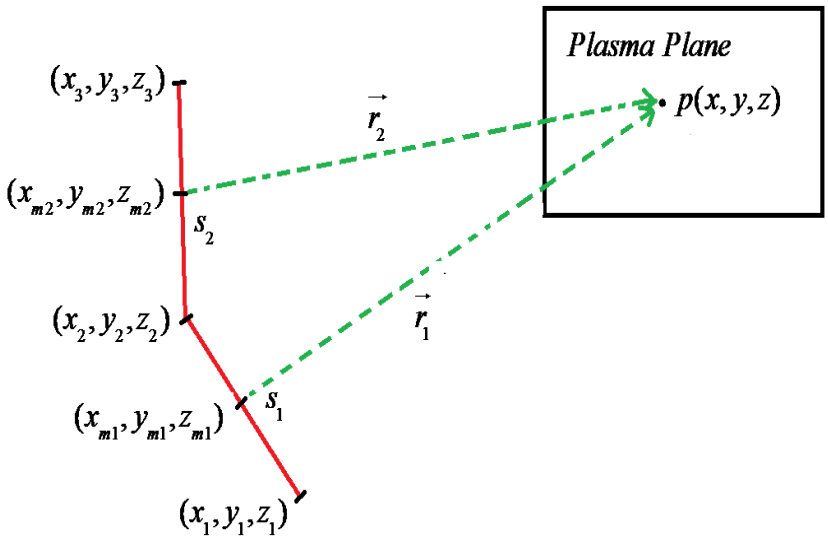

Figure 3.3: Magnetic field calculation using Biot Savart's law

Normalized magnetic field due to s_1 at any point in the simulation box p(x, y, z) is given by

$$B_{s1} = \frac{\vec{dl_1} \times \vec{r_1}}{|\vec{r_1}|^2}, \tag{3.19}$$

where B_{s1} is the normalized magnetic field due to s_1, $\vec{dl_1}$, and $\vec{r_1}$ are the length and the range vector of s_1 given by

$$\vec{r_1} = (x - x_{m1})\hat{a}_x + (y - y_{m1})\hat{a}_y + (z - z_{m1})\hat{a}_z, \tag{3.20}$$

$$\vec{dl_1} = (x_2 - x_1)\hat{a}_x + (y_2 - y_1)\hat{a}_y + (z_2 - z_1)\hat{a}_z. \tag{3.21}$$

In Equation (3.29), $\times$ denotes vector cross product and $\hat{a}$ in Equations (3.20) and (3.21) represents the unit vector. Similarly normalized magnetic field due to side s_2 at any point in simulation box p(x, y, z) is given by

$$B_{s2} = \frac{\vec{dl_2} \times \vec{r_2}}{|\vec{r_2}|^2}. \tag{3.22}$$

Magnetic field due to entire coil, which is made up of 250 current elements is given by

$$B_{coil} = \sum_{i=1}^{250} B_{si}. \tag{3.23}$$

Since solenoid in the simulation consist of eighteen coils, we repeat the above calculation for all the coils and then sum them to get total magnetic field of the solenoid as given below

$$B_{sol} = \sum_{i=1}^{18} B_{coil(i)}, \tag{3.24}$$

where B_{sol} is the total magnetic field in the simulation box due to the solenoid and $B_{coil(i)}$ is the magnetic field produced by i th coil.

B_{sol} is then scaled as given by

$$B_Z(i,j) = \frac{3B_{sol,Z(i,j)}}{B_{sol,Z(X=0,Z=0)}} \quad \text{and} \quad B_X(i,j) = \frac{3B_{sol,X(i,j)}}{B_{sol,Z(X=0,Z=0)}}, \tag{3.25}$$

where $B_X(i,j)$ and $B_Z(i,j)$ are the X and Z component of the scaled magnetic field used in the PIC simulation, i and j are the index along X and Z axis respectively. $B_{sol,X}$ and $B_{sol,Z}$ are the X and Z component of B_{sol}. From the geometry of the problem shown in Figure 3.1 we can observe that Y component of the magnetic field is zero; hence only X and Z components of the scaled magnetic field are shown in Figure 3.5 and 3.6. Once we calculate the magnetic field at all grid points, it is shared at every particle positions by a weighting scheme. To illustrate the weighting scheme used, consider a particle located between four grid points as shown in Figure 3.4.

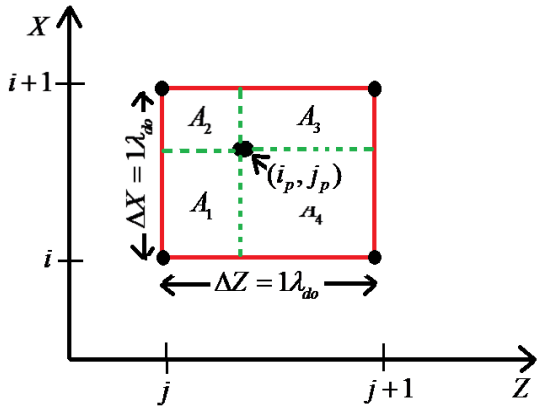

Figure 3.4: Weighting scheme used for magnetic field

Let the particle coordinates be (i_p, j_p) as shown in the Figure 3.4. The magnetic field B at the location (i_p, j_p) is given by

$$B(i_p, j_p) = \frac{A_1(B(i,j)) + A_2(B(i,j+1)) + A_3(B(i+1,j+1)) + A_4(B(i+1,j))}{A}, \tag{3.26}$$

where $A = \Delta X \Delta Z$ is the area of the cell and A_1, A_2, A_3, A_4 are the area of partial squares. The A_1, A_2, A_3, A_4 areas are calculated by using the distances between the coordinates of the particle and grid points (i_p, j_p). Electric field is also shared at all particle locations in a similar way.

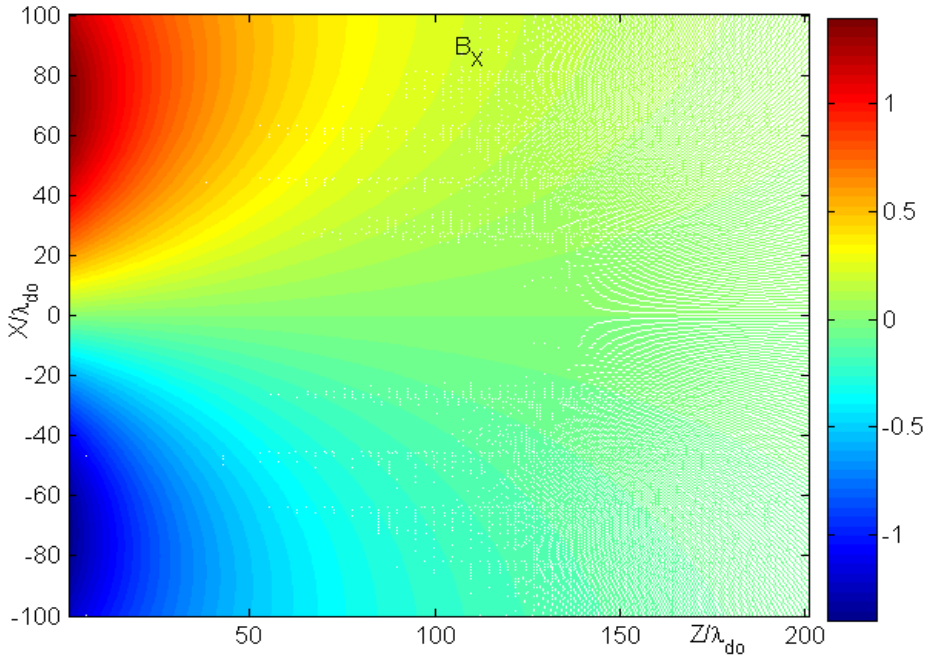

Figure3.5: B_X in the simulation box ($N_X = N_Z = 201$, w=60 and r=66)

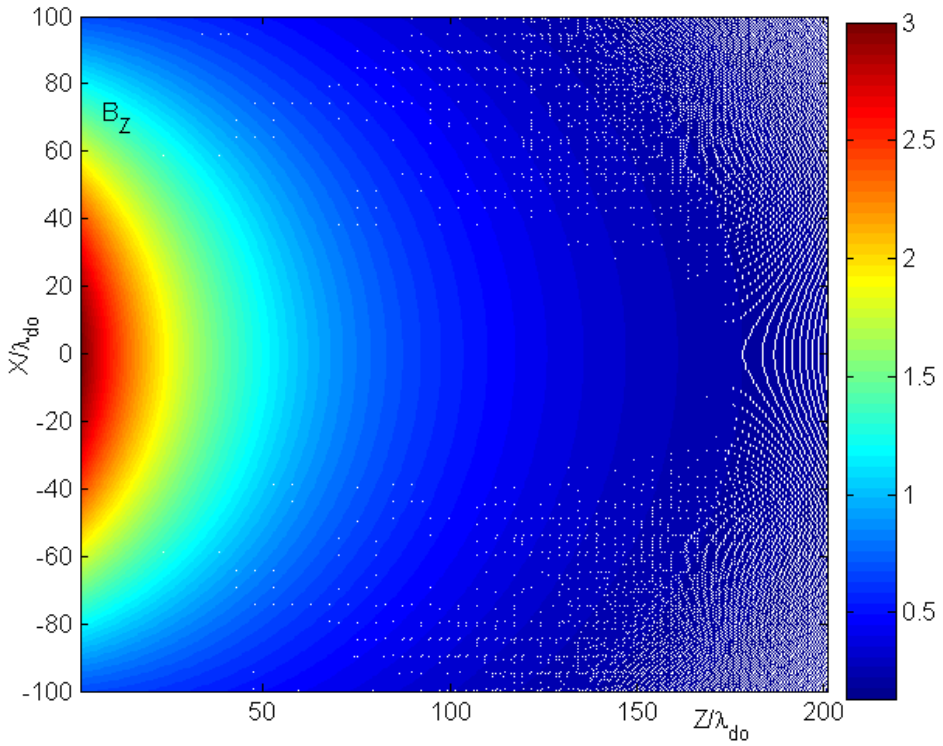

Figure 3.6: B_Z in the simulation box ($N_X = N_Z = 201$, w=60 and r=66)

3.5 CHARGE DENSITY CALCULATION

Each particle in the simulation box contributes some amount of charge to its surrounding grid points. The amount of charge density contributed by the particle depends on its position. Figure 3.7 shows a particle with normalized charge q surrounded by four grid points. The particle contributions to the charge density at the four spatial grid points are given by:

At grid point (i, j): $\rho(i, j) = q\frac{A_1}{A}$

At grid point (i+1, j): $\rho(i+1, j) = q\frac{A_4}{A}$

At grid point (i, j+1): $\rho(i, j+1) = q\frac{A_2}{A}$

At grid point (i+1, j+1): $\rho(i+1, j+1) = q\frac{A_3}{A}$

where $A = \Delta X \Delta Z$ is the area of the cell and A_1, A_2, A_3, A_4 are the area of partial squares. The $A_1, A_2, A_3,$ and A_4 are calculated by using the distances between the coordinates of the particle and the coordinates of surrounding grids. If there are N particles, then total charge density at any point (i, j) is given by summation of charge contributions as given by

$$\rho(i, j) = \sum_{n=1}^{N} q_n(i, j), \tag{3.27}$$

where q_n is the charge density contribution at grid point (i, j) by the n –th charge particle.

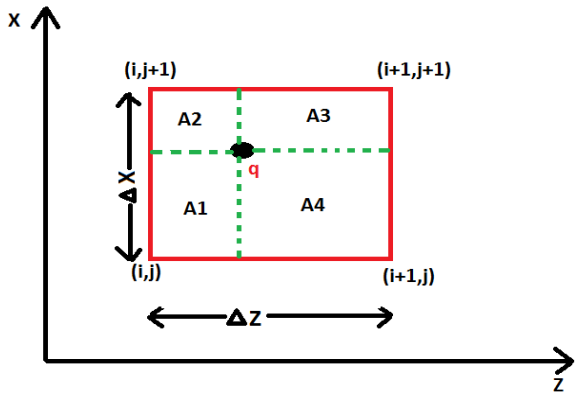

Figure 3.7: Distribution of charge density

3.6 POISSON SOLVER

Electric potential is obtained by solving the Poisson equation. Poisson equation is numerically solved using finite difference method. Normalized Poisson equation in two dimensions is given by

$$\frac{\partial^2 \phi}{\partial X^2} + \frac{\partial^2 \phi}{\partial Z^2} = -\rho. \tag{3.28}$$

Let i denote the index along X-axis and j denote the index along Z-axis as shown in the Figure 3.8. Expressing Equation 3.28 in finite difference form, we get

$$\frac{\phi(i+1,j) - 2\phi(i,j) + \phi(i-1,j)}{(\Delta x)^2} + \frac{\phi(i,j+1) - 2\phi(i,j) + \phi(i,j-1)}{(\Delta z)^2} = -\rho(i,j), \tag{3.29}$$

where $\Delta x = \Delta z = 1\ \lambda_{d0}$ is the step size in space.

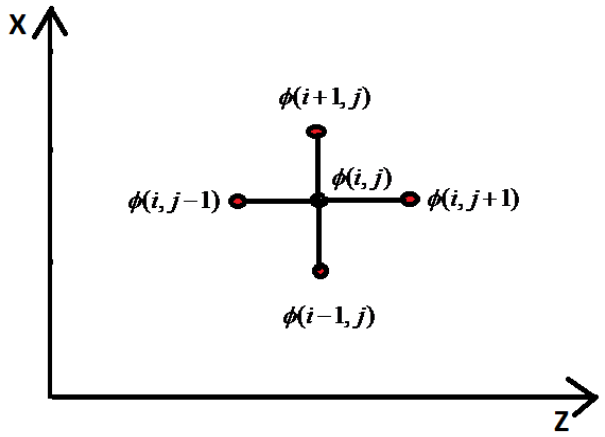

Figure 3.8: Five point stencil for solving Poisson equation

Eq. (3.29) simplifies to

$$4\phi(i,j) = \phi(i+1,j) + \phi(i-1,j) + \phi(i,j-1) + \phi(i,j+1) + \rho(i,j). \tag{3.30}$$

To solve Equation 3.30, we use iterative method known as successive over relaxation method [19]. In this method, we define a residual matrix $R(i,j)$ given by

$$R(i,j) = \phi(i+1,j) + \phi(i-1,j) + \phi(i,j-1) + \phi(i,j+1) + \rho(i,j) - 4\phi(i,j). \tag{3.31}$$

In the iterative loop, $R(i,j)$ weighted with a factor ω_F is added to $\tilde{\phi}(i,j)$. Iteration marches till $R(i,j)$ converges to some predetermined value. For the K- th iteration in the loop, we therefore have

$$\phi_{K+1}(i,j) = \phi_K(i,j) + \omega_F R_K(i,j), \tag{3.32}$$

where ω_F is called the convergence factor. Convergence factor reduces the convergence time of the solution. The optimum value of ω_F is given by [19]

$$\omega_F = \frac{8 - \sqrt{64 - 16t^2}}{t^2}, \tag{3.33}$$

where $t = \cos\frac{\pi}{\mathrm{N_X}} + \cos\frac{\pi}{\mathrm{N_Z}}$, $\mathrm{N_X}$, and $\mathrm{N_Z}$ are the total number of grid points in the X and Z direction. In our simulation, we have $\phi = 0$ boundary condition along the walls of the simulation box except at the PIW. We have floating boundary condition in the PIW. Boundary condition used in our simulation is illustrated in Figure 3.9 for specific parameters such as $\mathrm{N_X} = \mathrm{N_Z} = 201$ and w=60.

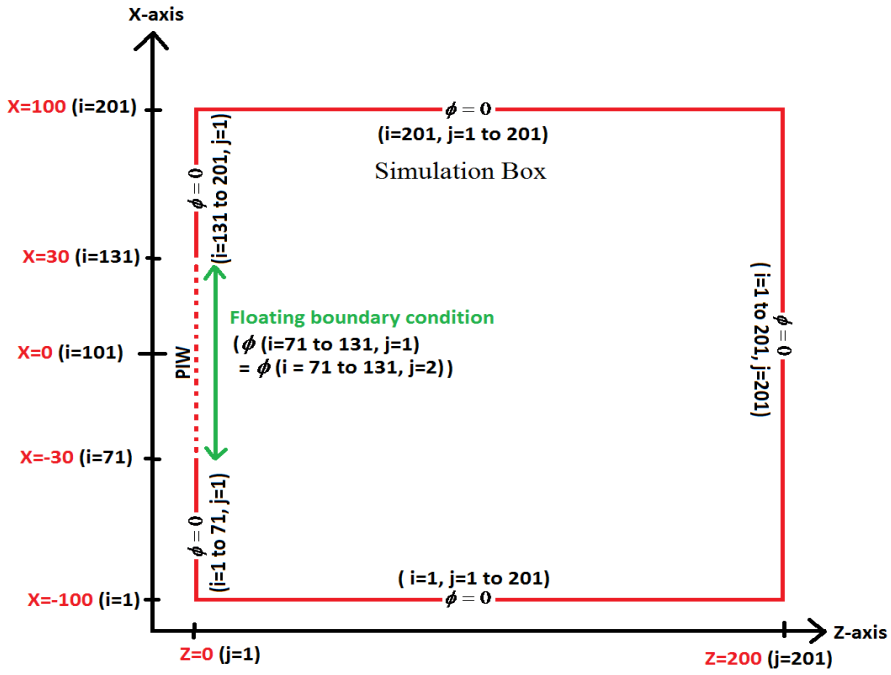

Figure 3.9: Boundary conditions ($N_X = N_Z = 201$ and w=60).

3.7 ELECTRIC FIELD COMPUTATION

Electric field is computed by finite differencing the electric potential as shown below

$$\tilde{E} = -\nabla\tilde{\phi}, \tag{3.34}$$

$$\tilde{E_x} = \frac{-(\tilde{\phi}(i+1,j) - \tilde{\phi}(i-1,j))}{2\Delta x} \text{ , and} \tag{3.35}$$

$$\tilde{E_z} = \frac{-(\tilde{\phi}(i,j+1) - \tilde{\phi}(i,j-1))}{2\Delta z}; \tag{3.36}$$

where $\Delta x = \Delta z = 1\,\lambda_{do}$ is the step size in space. Once we calculate electric field at all grid points, it is then shared at all particle location.

3.8 PARTICLE MOVER

Particles are moved according to Equations 3.13 to 3.18. The equation of motion for each particle is solved by Leap-Frog method [23]. To illustrate leap frog method, we consider Eq.3.13 as given by

$$\frac{dV_X}{dt} = -(E_X + V_Y \times B_Z) = F_X, \tag{3.40}$$

here F_X is the force experienced by the electron in X-direction. The velocity is given by time derivative of position expressed as

$$\frac{dX}{dt} = V_X. \tag{3.41}$$

Eq. 3.40 and 3.41 are replaced by finite difference equations, given by

$$\frac{V_{X(new)} - V_{X(old)}}{\Delta t} = F_{X(old)} \text{ and} \tag{3.42}$$

$$\frac{X_{(new)} - X_{(old)}}{\Delta t} = V_{X(new)}, \tag{3.43}$$

where Δt is the time step used in the simulation.

The velocity vector is advanced using Eq. (3.42). Using this advanced velocity; position vector is advanced using Eq. (3.43).

3.9 SIMULATION PARAMETERS AND INITIAL CONDITIONS

Table below presents important plasma parameters that are used in the simulation.

Time Step Δt :	$0.1/\omega_{pe}$
Axial injection velocity for ions	$12.6V_{Ti}$
Mass ratio: $\frac{m_i}{m_e}$	1600
Temperature ratio: $\frac{T_e}{T_i}$	40

Table 3.1: Simulation parameters and initial conditions

CHAPTER 4

NUMERICAL RESULTS

4.1 SIMULATION RESULTS

In this section, the dynamics of the simulated plasma, for the geometry shown in Figure 3.1, is discussed. We performed simulations with varying simulation size, divergence in magnetic field and the PIW width. Due to limited computational resources, we were able to achieve a maximum simulation size of $0< N_Z <200$ and $-100< N_X <100$. However, with this limited size, simulations yielded results that were close to Charles and Boswell experiments on HPD. We chose PIW width, w=60 and solenoid distance, d=65.

When the simulation reached quasi steady state, a U- shaped DL similar to Charles and Boswell experiment was observed [3]. Figure 4.1 shows that the axial potential drop across the DL is $\phi_{DL} = 3KT_e / e$. Densely populated contours near the throat and radial potential drop indicates perpendicular electric field in the simulation box. Such perpendicular electric field has been reported by Charles in her experiments [14]. The contour plot of the perpendicular electric fields in our simulation is shown in the Figure 4.3. A radial cut of $E_\perp$ near the PIW illustrates the divergence in the axial region and polarity changes in the outer region as shown in Figure 4.4. Generation of $E_\perp$ may be understood as an indication of perpendicular charge separation. Electrons move along

the magnetic field lines and ions are unmagnetized. This creates a tendency for radial charge separation creating large perpendicular electric fields near the source. Color map of ion and electron density are shown in Figure 4.5 and 4.6 respectively. From Figs. 4.5 and 4.6, we can easily see that $n_i \sim n_e$ thereby satisfying quasi-neutrality condition for a plasma. Note the conical structure of these density profiles which has been experimentally observed [3]. Even though, electron and ion density appears to be equal, there is a charge separation as indicated by the large perpendicular electric fields. In Figure 4.7, we present the radial distribution of ion density at some selected axial distance, Z. Near the PIW at Z=5, the density profile is nearly flat and occupies the radial region -30<X<30. At larger axial distance, density profile evolves into conical structure as seen from Figure 4.7 (a). At Z>150, electrons and ions cross the boundary of the simulation box as seen from Figure 4.5 and 4.6 respectively. Therefore, density on the cone surface for Z>150 will be less than that for Z<150. Figure 4.7 (b) shows the integral of $n_i(X)$ and $n_e(X)$ with respect to Z for the region 20<Z<150. We find that the integral of $n_i(X)$ and $n_e(X)$ with respect to Z in Figure 4.7 (b) is approximately conserved for the region Z<150. This means that plasma injected at the source self consistently distributes radially with increasing axial distance in the diverging magnetic field. The slight decrease in integral value of Figure 4.7 (b) indicates a small loss from the side walls.

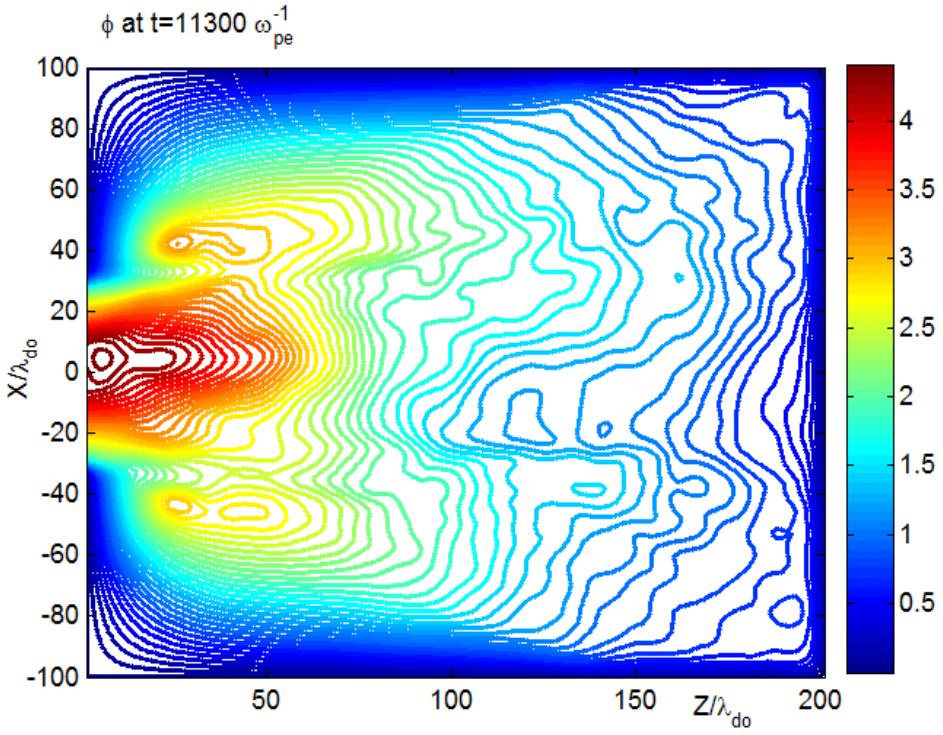

Figure 4.1: Equipotential contour map of ϕ at t=11300 $\omega_{pe}{}^{-1}$

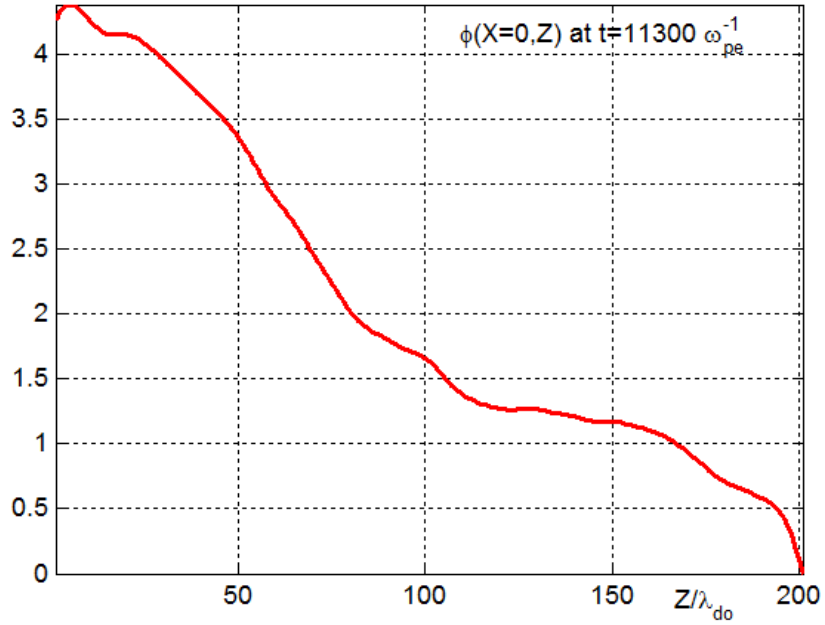

Figure 4.2: $\phi(X=0,Z)$ at t=11300 $\omega_{pe}{}^{-1}$

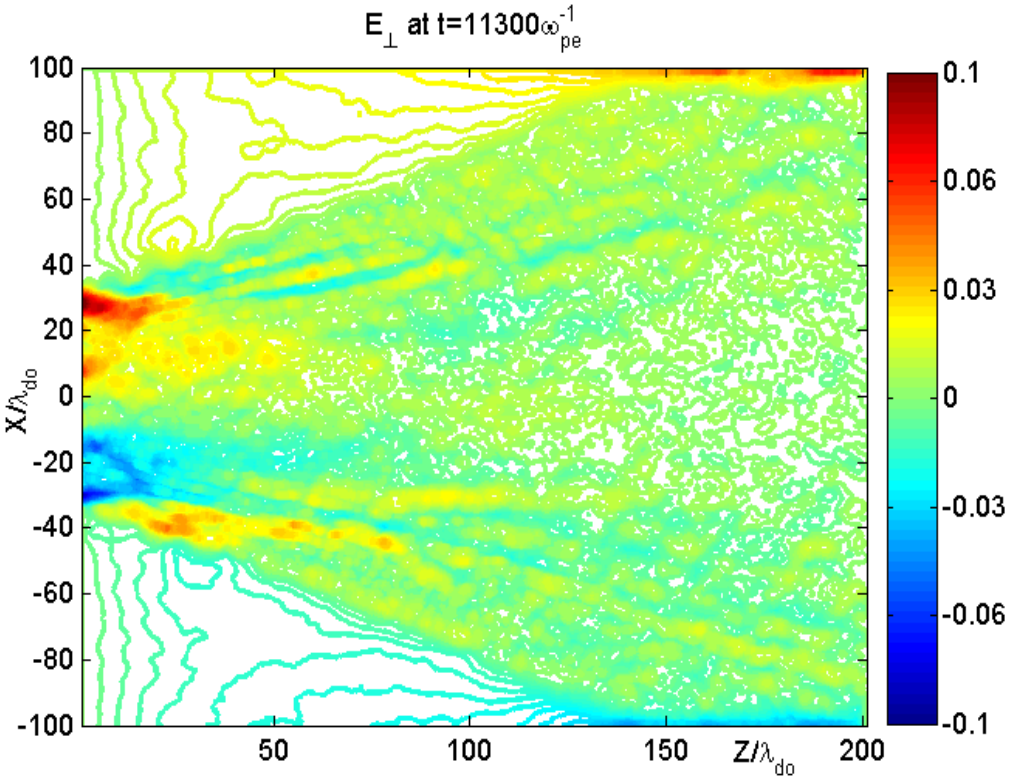

Figure 4.3: Contour map of $E_\perp$ at t=11300 ω_{pe}^{-1}

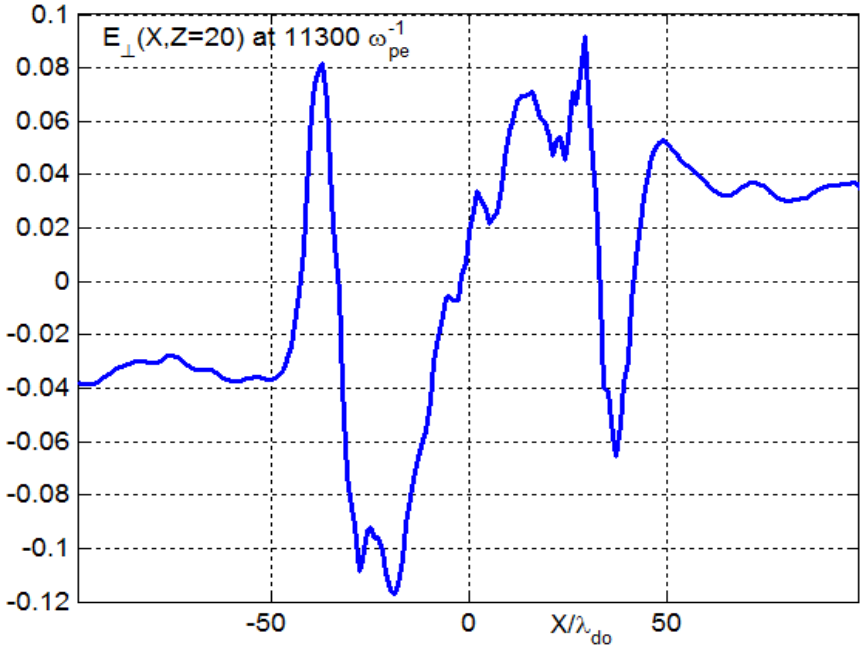

Figure 4.4: $E_\perp$(X, Z=20) at t=11300 ω_{pe}^{-1}

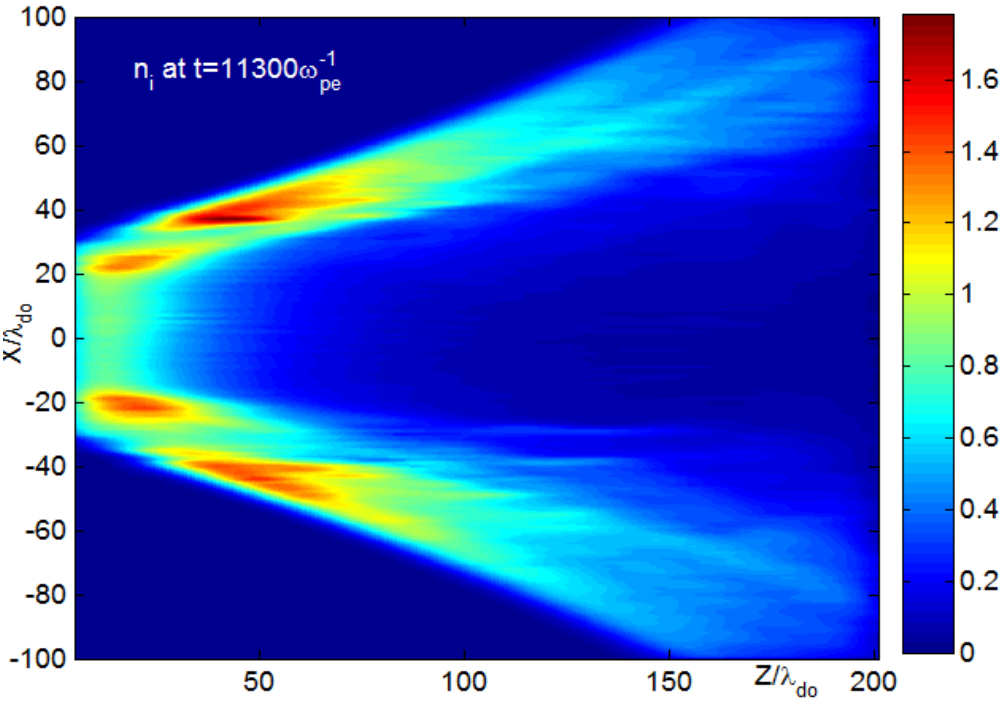

Figure 4.5: Color map of ion density n_i at t=11300 ω_{pe}^{-1}

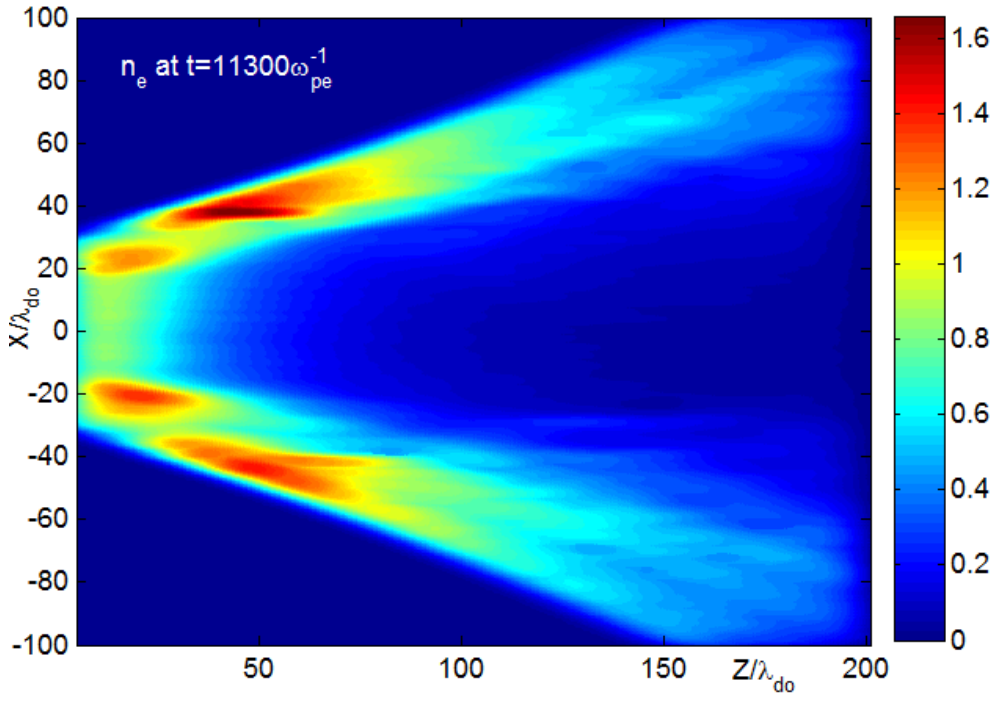

Figure 4.6 Color map of electron density n_e at t=11300 ω_{pe}^{-1}

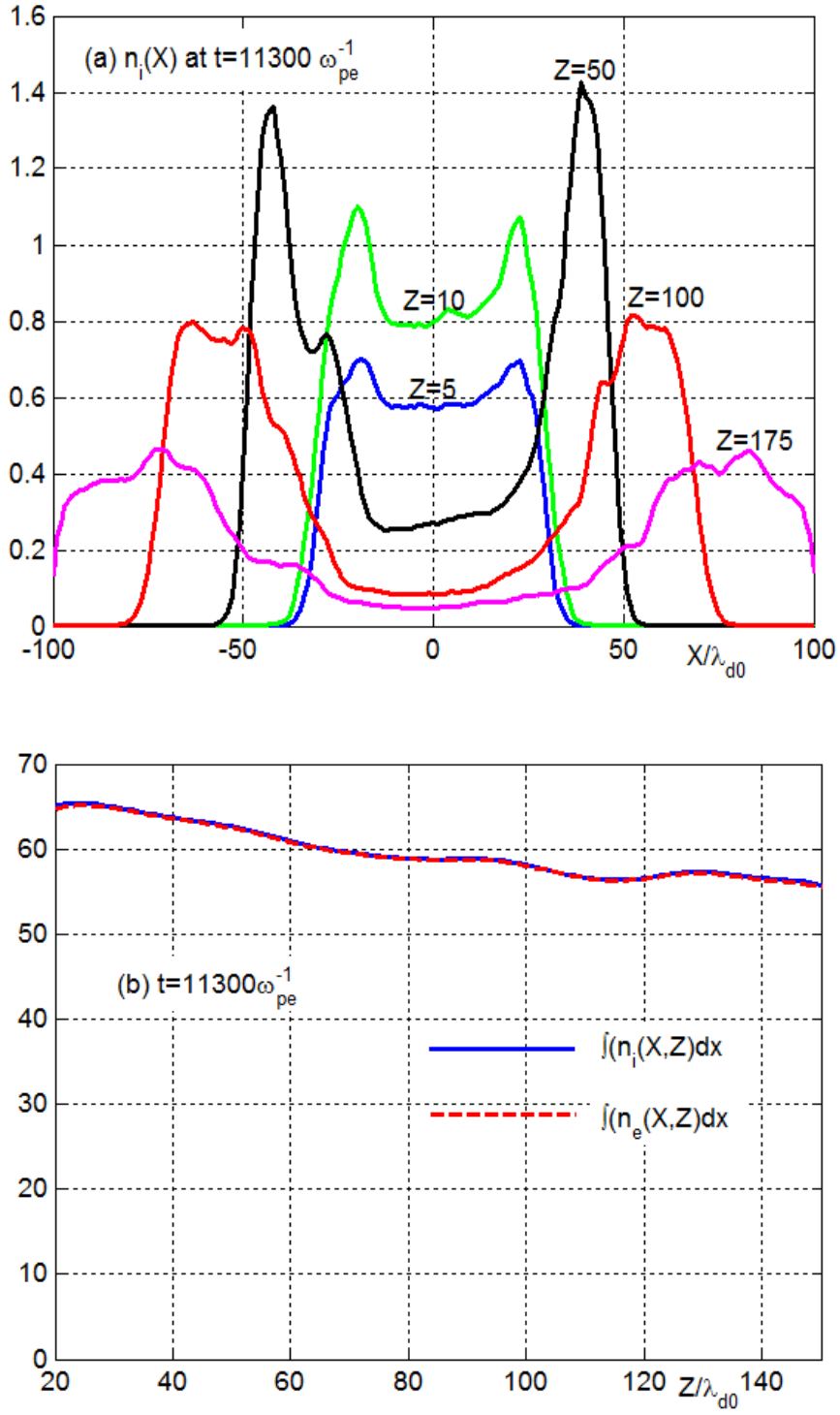

Figure 4.7: (a) $n_i(X)$ along Z = 5, 10, 50, 100, and175 and (b) integral of $n_i(X)$ and $n_e(X)$ (dashed line) for 20<Z<150

Electrons and ions are coupled by electric fields and they move together making plasma a quasi-neutral gas. But, in the PIC simulation, there is always a tendency for some energetic electrons to move ahead of ions in a free manner creating large amplitude fluctuation in the electric potential. This process is unphysical and a numerical artifact. Once electrons and ions achieve steady flow, these large amplitude waves or oscillations reduce in amplitude and have a physical meaning as explained later. The time required for electrons and ions to reach a steady flow is referred as the steady state time. Time taken to reach steady state depends on the size of the simulation box, velocity of the injected particles at the PIW and their subsequent acceleration by the DL. Figure 4.8 shows the time history of electric potential at selected locations. For this particular simulation, steady state is achieved for $t > 4000\,\omega_{pe}^{-1}$ as seen from Figure 4.8. We can see that, the large amplitude oscillations are not just near the source but present even in regions that are away from the source (Figure 4.8). Notice that these waves diminish in amplitude substantially after reaching steady state.

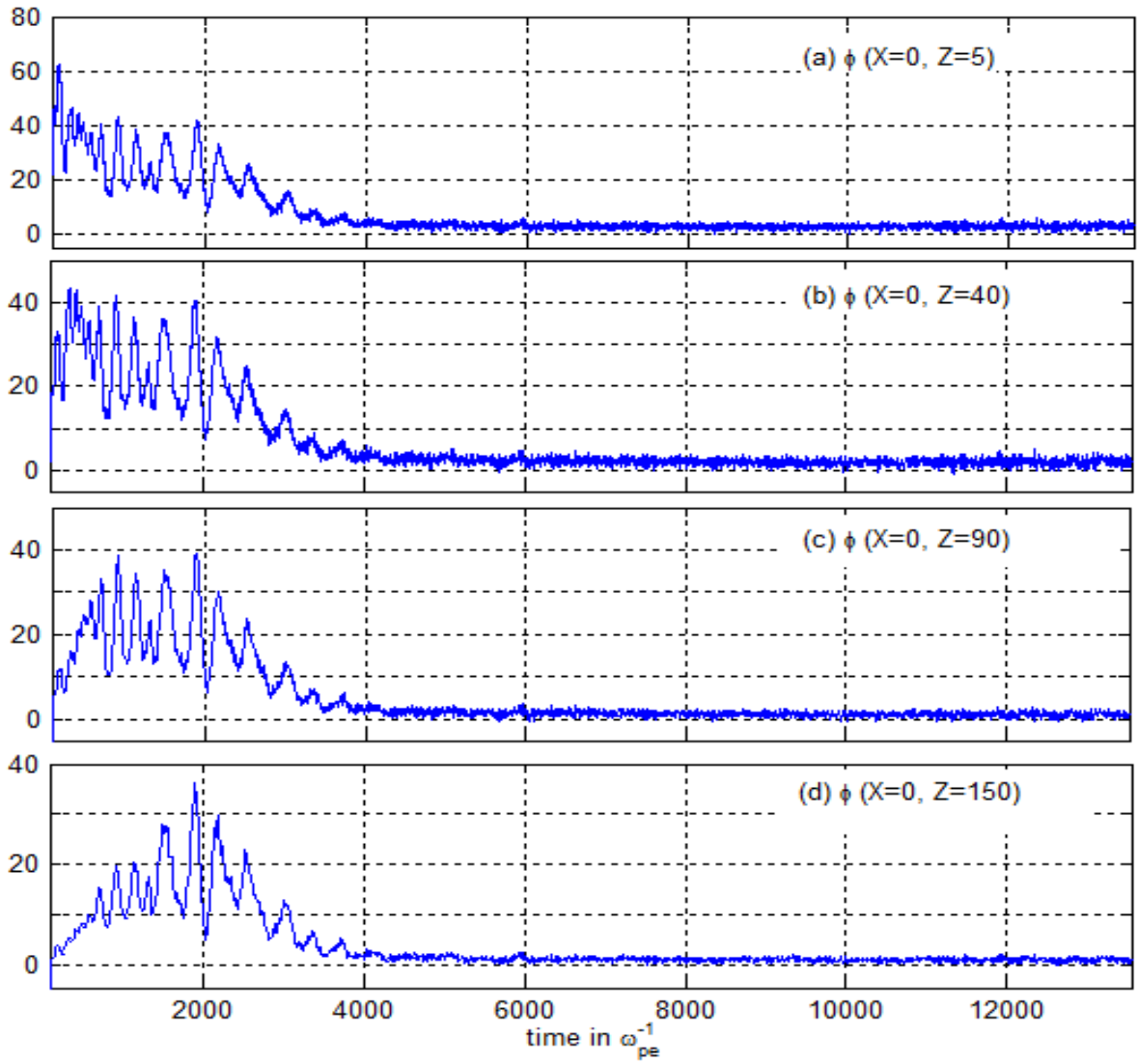

Figure 4.8: Time history of electric potential ϕ at selected points

Figure 4.9 (a) and (b) shows Fourier transform of $\phi(t)$ before and after reaching steady state. Figure 4.9 (a) reveals large amplitude low frequency oscillation which is a numerical artifact, but the spectrum in Figure 4.9 (b) contains both low and high frequency low amplitude oscillations which are caused by electron and ion oscillations.

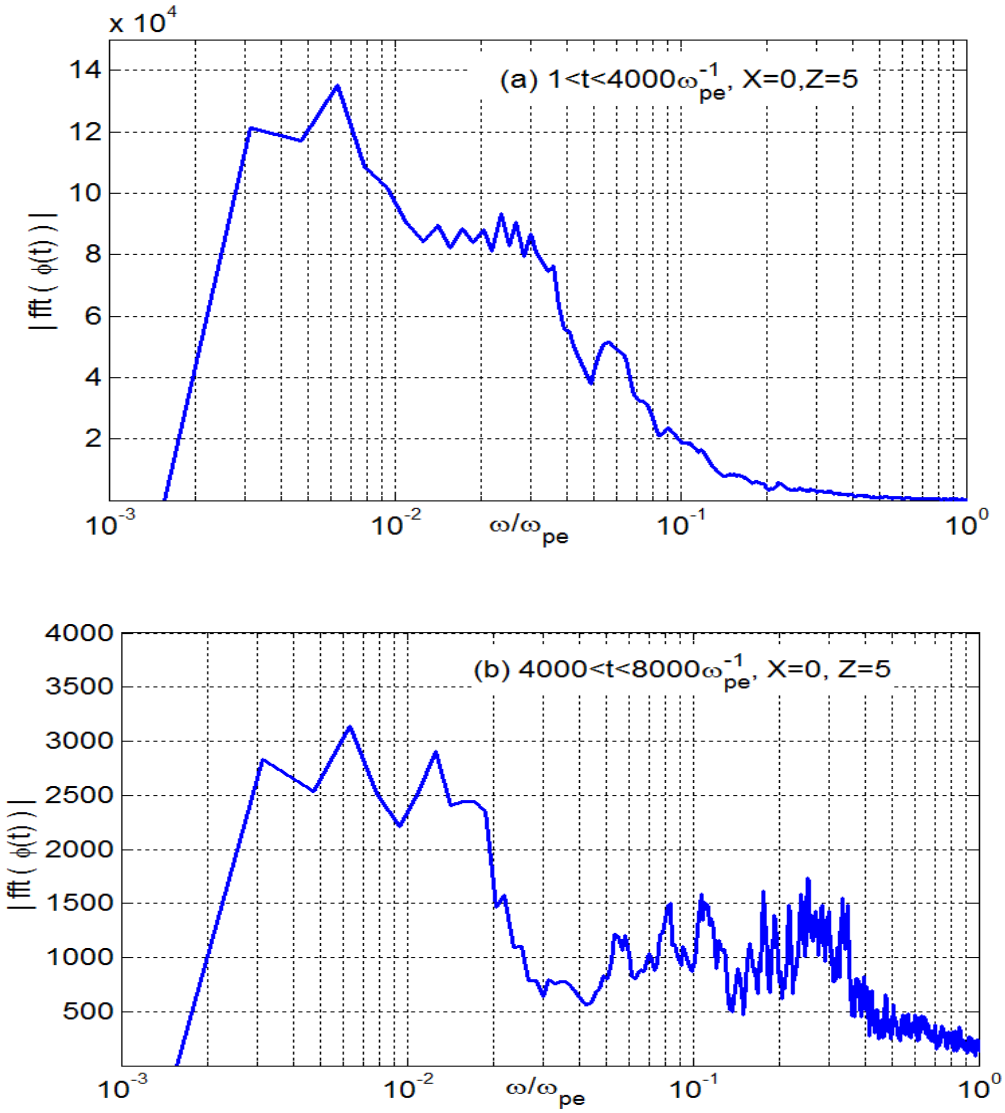

Figure 4.9: Frequency spectrum of $\phi(t)$: (a) before reaching steady state and (b) after reaching steady state

Whenever there is a tendency for a charge separation as in the HPD, electric field develops within the plasma which try to restore neutrality of the plasma. This process of restoring usually creates oscillations. Since electrons respond to the electric field at a rate much faster than the ions, they oscillate at a higher frequency. Ions being heavy oscillate at a much lower frequency compared to the electrons. Depending on the magnitude of

charge separation and other factors such as temperature of the particles, these oscillations can create plasma instabilities creating fluctuations in electric potential ϕ. Figure 4.10 (b) depicts the fast oscillations in the electric potential created by electrons.

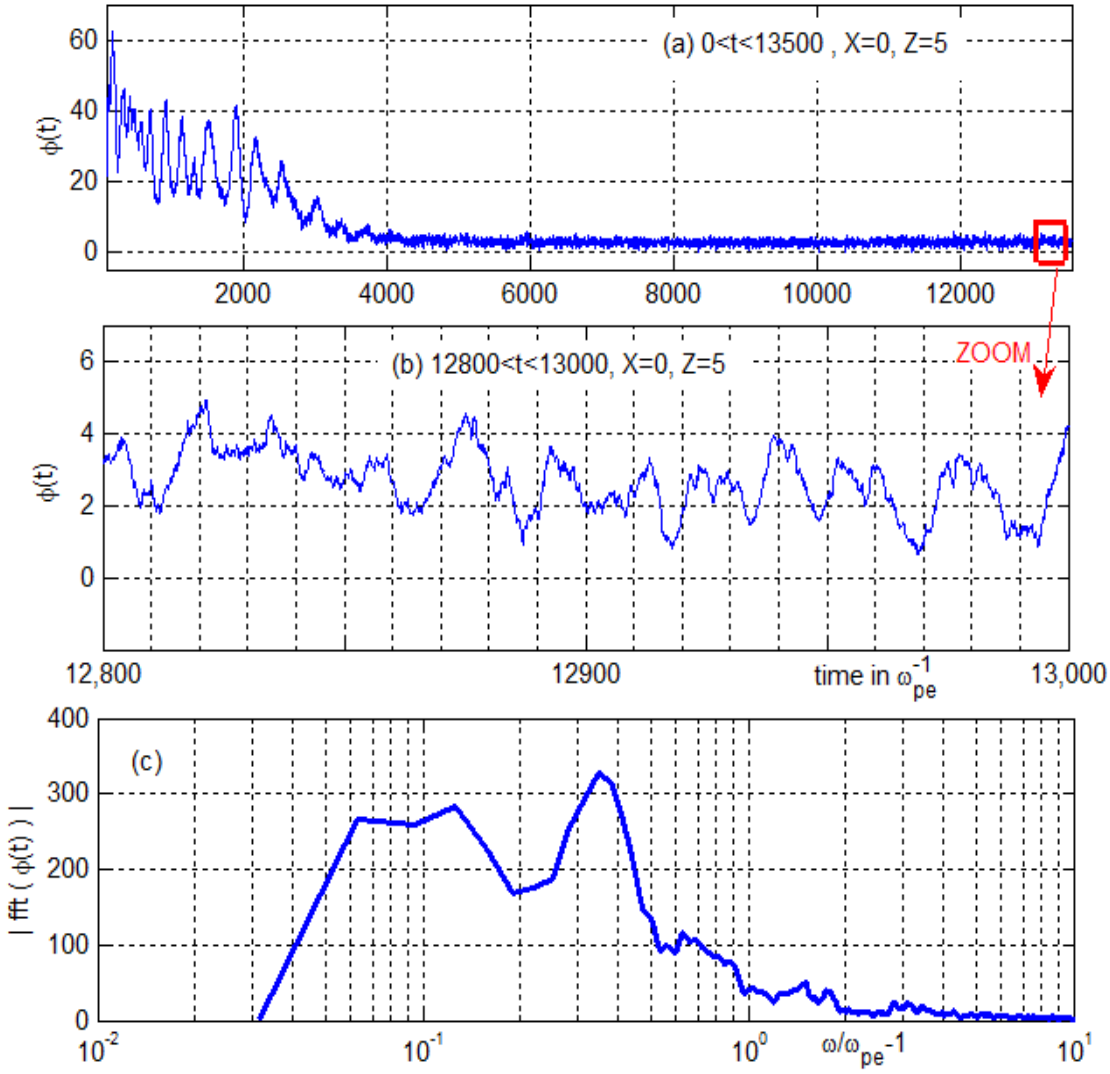

Figure 4.10: (a) $\phi(t)$ at X=0, Z=5 for 0<t<13500 ω_{pe}^{-1} , (b) $\phi(t)$ at X=0, Z=5 for 12800<t<13000 ω_{pe}^{-1} and (c) Frequency spectrum of Figure 4.10 (b)

Evolution of double layer in the simulation box is presented in Figure 4.11. The upper four panels of Figure 4.11 show ϕ at times before steady state. Figure 4.11 (e) and (f)

present ϕ in the transition state and Figure 4.11 (g) and (h) shows steady state ϕ. The perturbation caused due to plasma oscillation as in Figure 4.11 (e) can be removed by averaging ϕ over one ion oscillation period which is roughly $200\,\omega_{pe}^{-1}$. For example, the averaged ϕ denoted by ϕ_a at $12200\,\omega_{pe}^{-1}$ is the average value of 200 instantaneous ϕ values from $12000\,\omega_{pe}^{-1}$ to $12200\,\omega_{pe}^{-1}$. Figure 4.12 shows the instantaneous electric potential ϕ and averaged electric potential ϕ_a at different times. Figure 4.12 (a) and (b) clearly illustrates the removal of ion and electron oscillations by the averaging process. We can notice that the perturbation is greatly reduced in averaged electric potential ϕ_a compared to instantaneous electric potential ϕ. Averaging also results in a steady potential structure. The simulated double layer as in Figure 4.12 contains three interesting structures which are a) U shaped high potential region anchored to the central region of PIW which we will call the main lobe region and b) two high potential regions near the edge of the PIW which we will refer as side lobe regions. Notice that the side lobe region is absent at the early times as shown in Figure 4.11 (a). The maximum potential in the side lobe region could be higher than the maximum main lobe potential in the unsteady state due to unphysical oscillations. Once the simulation reaches a steady state, the maximum side lobe potential is always less than or equal to the maximum main lobe potential as seen from Figure 4.12.

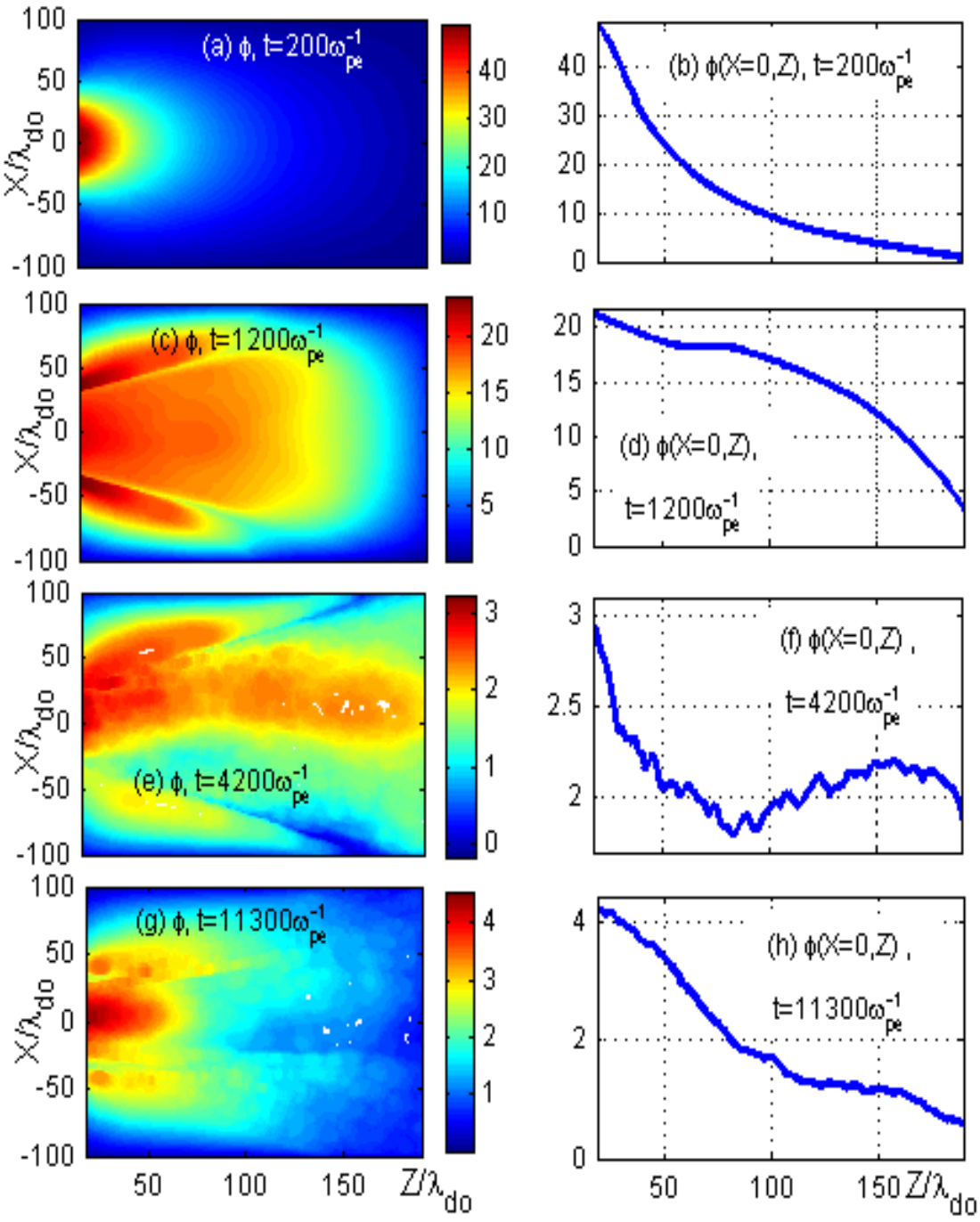

Figure 4.11: Evolution of electric potential at different times. Left panels show color map of ϕ and right panels show axial profile of ϕ at X=0

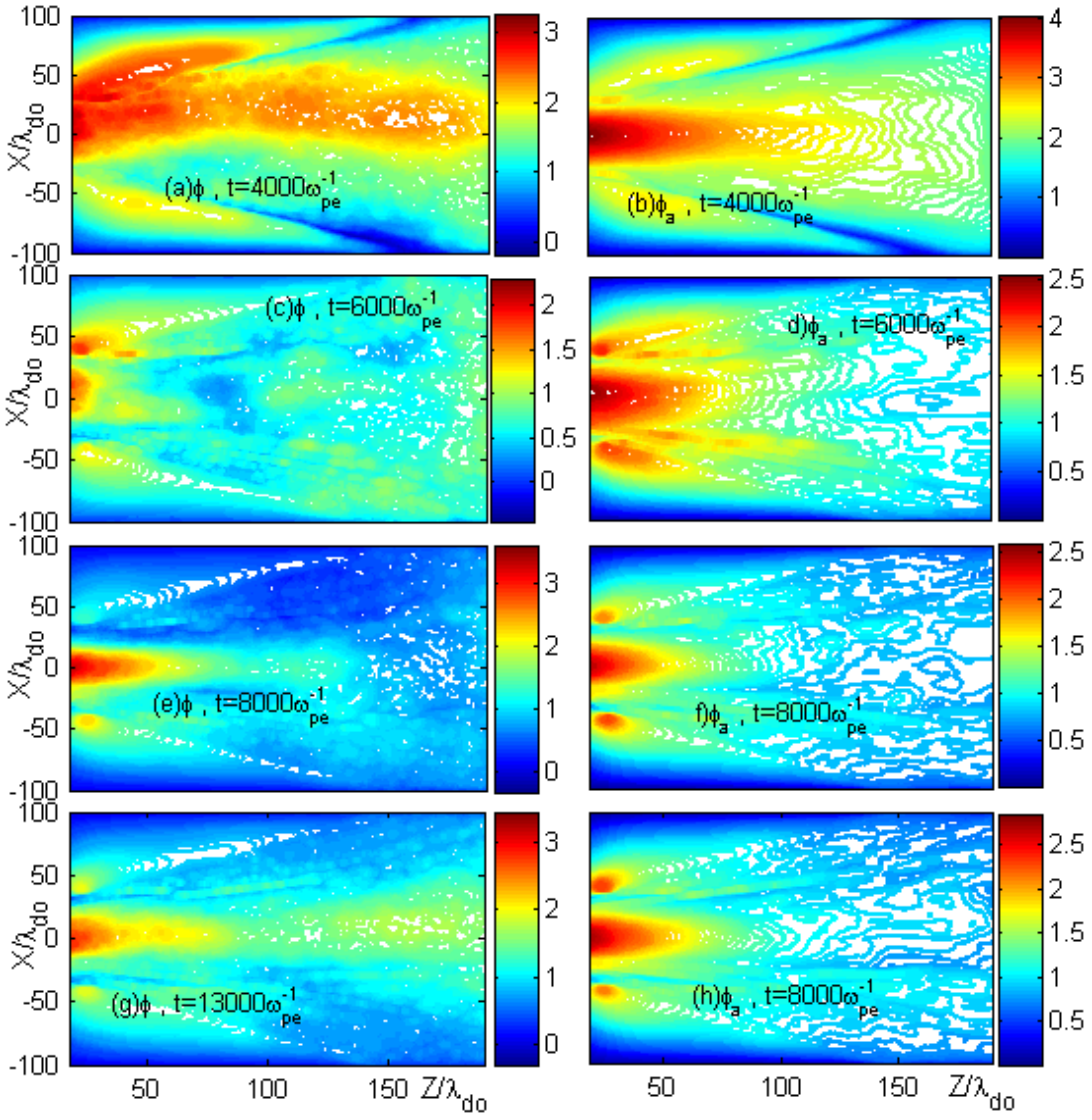

Figure 4.12: Comparison of instantaneous electric potential ϕ (left panels) and averaged electric potential ϕ_a (right panels) at different times

We next investigate the temporal evolution of spatial distribution of electrons and ions as shown in Figure 4.13 and Figure 4.14. In Figures 4.13 and 4.14, red dots represent electrons and ions are over plotted on them as blue dots. Due to over plotting, some regions appear violet. Violet region is just the result of mixing red and blue colors.

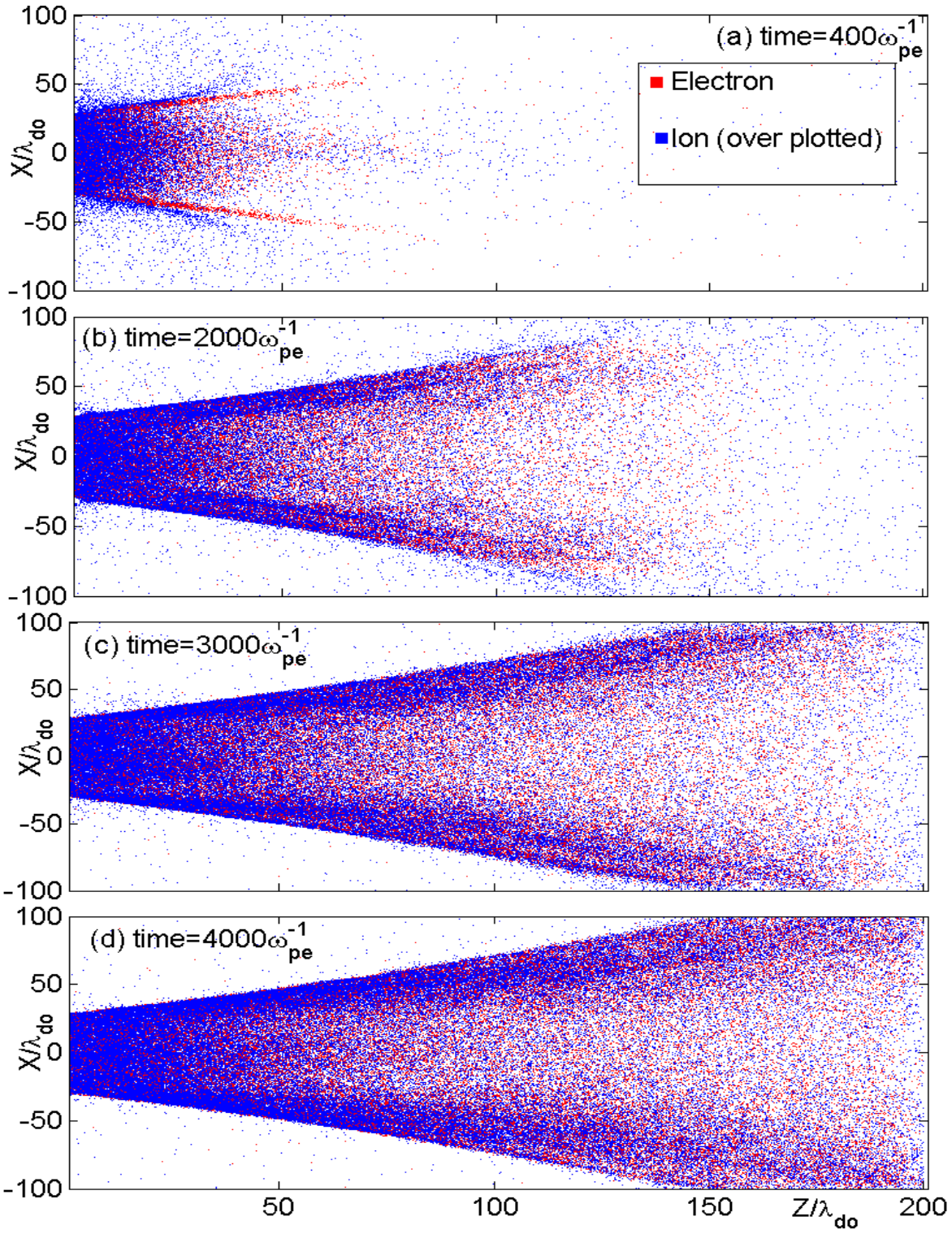

Figure 4.13: Spatial distributions of electrons and ions at different times before reaching steady state

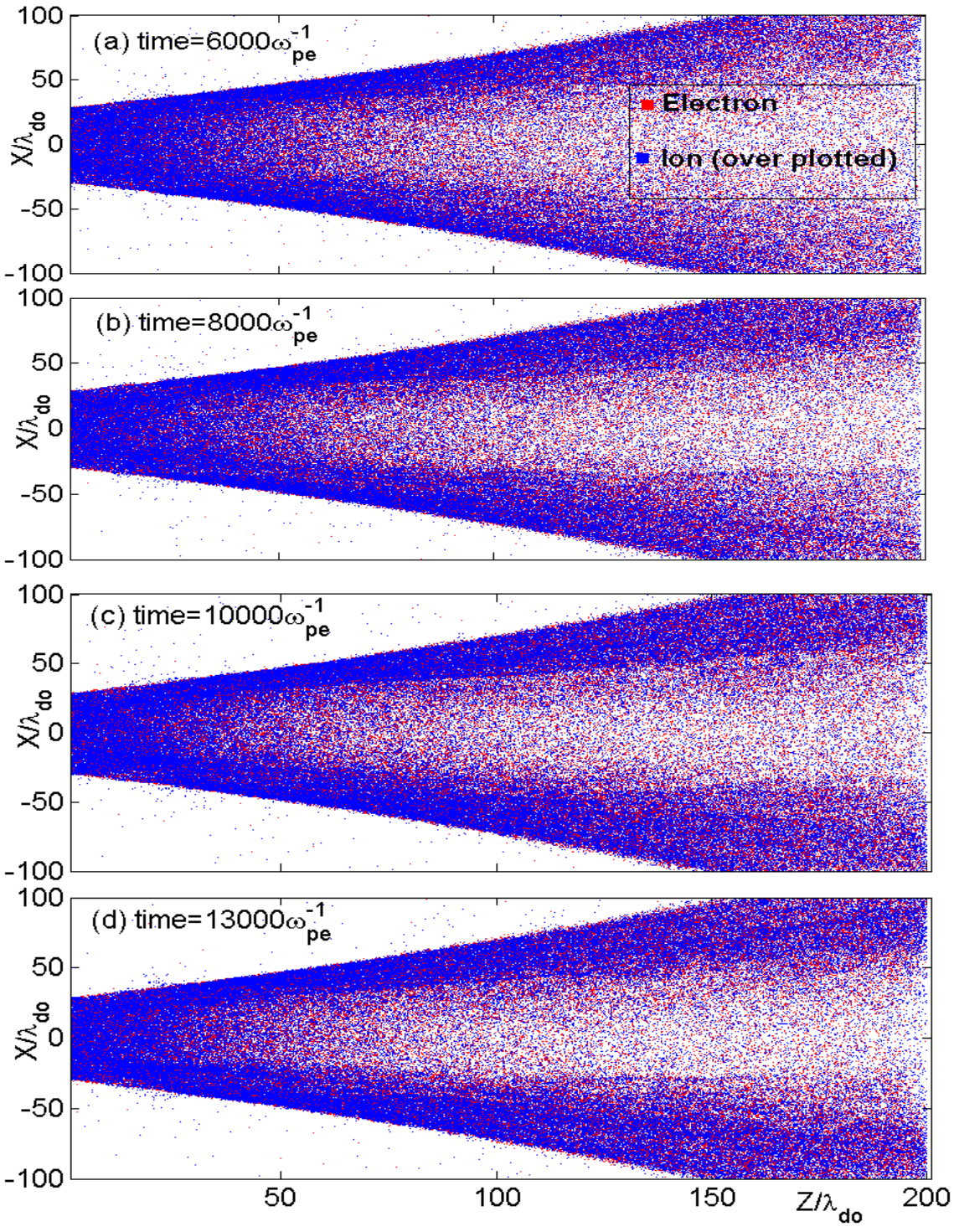

Figure 4.14: Spatial distributions of electrons and ions at different time after reaching steady state

In Figures 4.13 and 4.14, continuous patches of blue color forming the conical structure indicate large number of electrons and ions overlapping. Violet dots indicate that ions and electrons are very close to each other with minute separation, due to which these regions appear as a blend of blue and red color. In between the cone ($Z>50$, $|X|<30$), we have both red and blue dots with white background indicating low density particles. In Figure 4.13 (a), electrons begin to flow in a constricted conical path ahead of the ions. This large difference in motion of electrons and ions is unphysical and is the reason for the large amplitude fluctuation in electric potential seen in the Figure 4.8. Electrons being strongly magnetized flow along the B-field lines first populating the conical region, generating perpendicular electric fields, $E_{\perp}$. Ions are then pulled by $E_{\perp}$, forming conical structure in the plasma. In steady flow, the number of particles present in the simulation box is very large and hence the tendency for charge separation in the plasma is difficult to observe. By inspecting the velocity-position phase space of electrons and ion, we can detect the difference in electron and ion motion or the tendency for charge separation in the steady flow state.

In the unsteady state as in Figure 4.13 (a), there are not enough ions in the simulation box to control or hold back the electrons that are moving ahead of them. This creates unphysical large amplitude oscillation as discussed earlier. When the plasma flow reaches steady state, ions and electrons move together as in Figure 4.14. However, we notice that, even in the steady state there is a tendency for electrons to diverge and ions to move straight creating perpendicular electric field as shown in Figure 4.3. Z-V_X phase plot of electrons and ions are shown in Figure 4.15. We can see the ions that are accelerated by the perpendicular electric field are in the region $Z<40$. These phase plots reveals the

difference in electron and ion movement. We find that Electrons which are near the PIW develop $E_{\perp}$x B_Z drift. This drift is along the negative Y direction for X>0 and along positive Y direction for X<0. Such a drift constitutes a current J_d (carried by the electron). Thus J_d x B force develops which then transports source electrons radially outward from the central region into the cone, where J_d is the current density. This results in electrons forming conical structure. The electric field pull makes ions to follow electrons resulting in a conical plasma flow as shown in Figure 4.14.

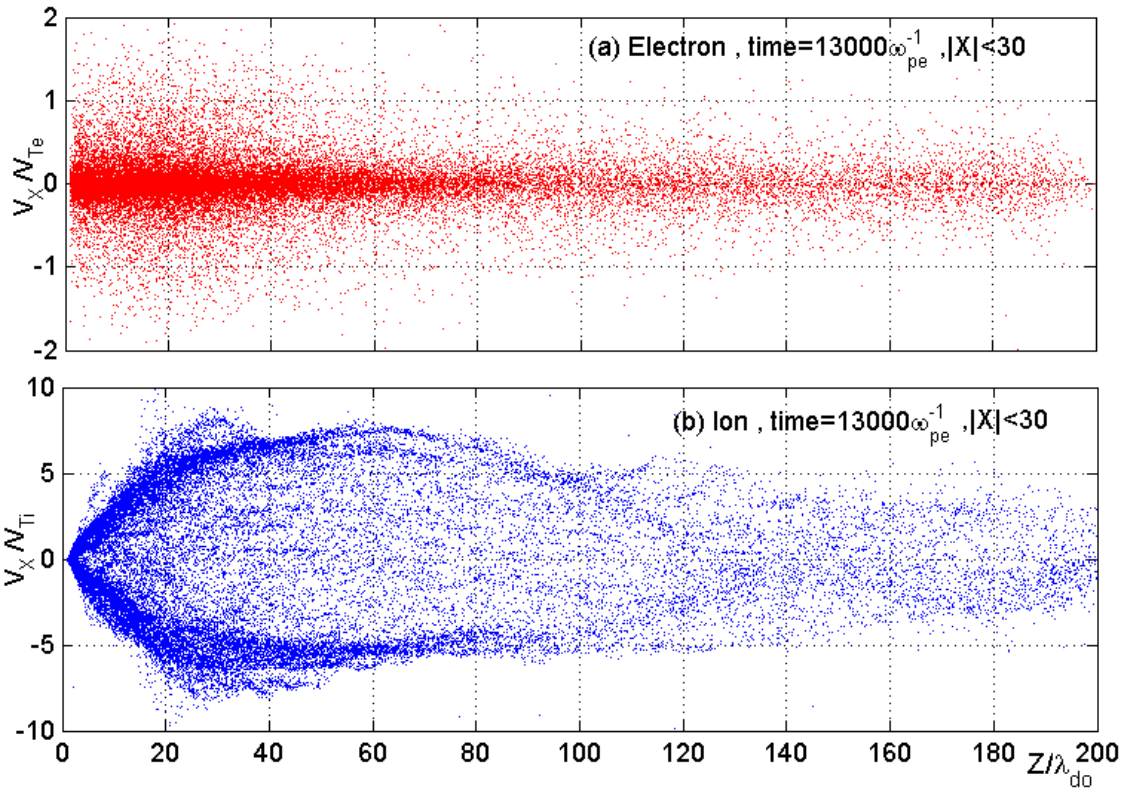

Figure 4.15: Z-V_X phase plot for (a) electrons and (b) ions at t=13000 ω_{pe}^{-1} for |X|<30

We also note that the radial velocity, V_X, for ions in the region Z>40 gradually decrease indicating a reduction in the temperature and it remains constant for the region 40<Z<80 where the double layer is situated. Ions below the double layer are radially

heated and ions above the double layer are getting cooled in X direction forming fish like structure as seen in Figure 4.15 (b). Radially heated ions below the double layer (Z<40) flow along the cone, while the cold ions above the double layer (Z>40) flow along the axial direction. Since electrons are highly magnetized, they do not form fish like structure.

We next examine the X-V_X phase plots of ions and electrons as shown in Figure 4.16. Ions initially get accelerated by the perpendicular electric field but however, once they cross the conical surface, they are stopped by the reversed polarity of $E_\perp$ forming vortex like structures. Hence, ions accelerated by $E_\perp$ are not lost to the boundaries of the simulation box, instead confined in the cone. This vortex formation may be the reason for the side lobe structures in electric potential in Figure 4.1. From Figure 4.16 (a) to (d), we find that electrons in the cone have large spread in radial velocity V_X forming dumbbell-shaped structure in X-V_X space. This indicates that conical surface comprises of heated particles. Heating of the particles is due to the generation of electrostatic plasma waves.

In Figure 4.17, Z-V_Z phase plot at different times is shown for the region -10<X<10. Note the sudden axial acceleration of ions in the Figures 4.17 (e) to (f). Such axial acceleration of the ions due by the double layer is the essence of Helicon Double Layer Thruster (HDLT). We also note that there is decrease in ion numbers with increasing axial distance due to the conical distribution of electrons and ions. This can be verified by examining X-V_Z phase plot as discussed next.

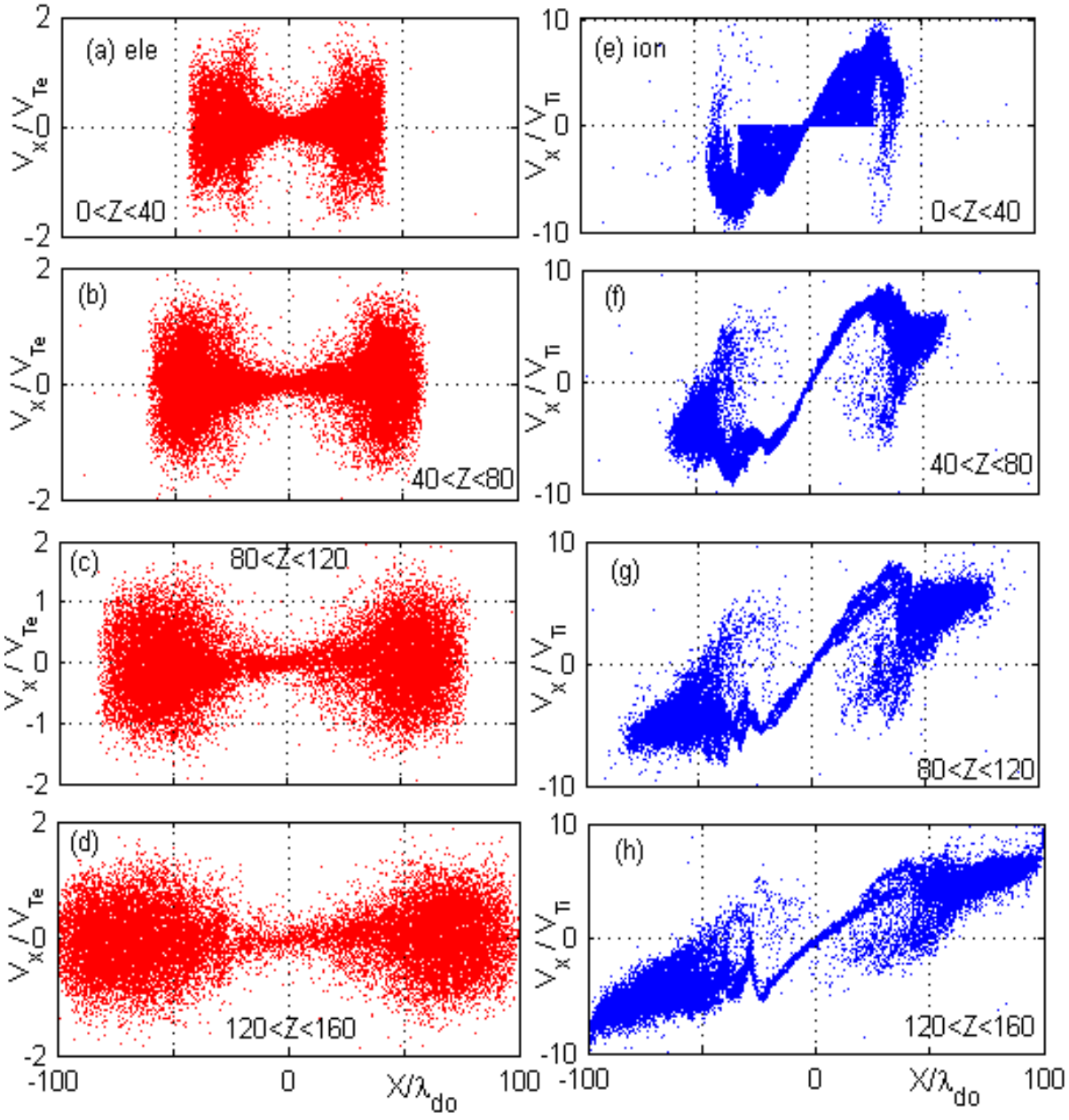

Figure 4.16: X-V_X phase plots for ions (blue) and electrons (red) at different axial regions

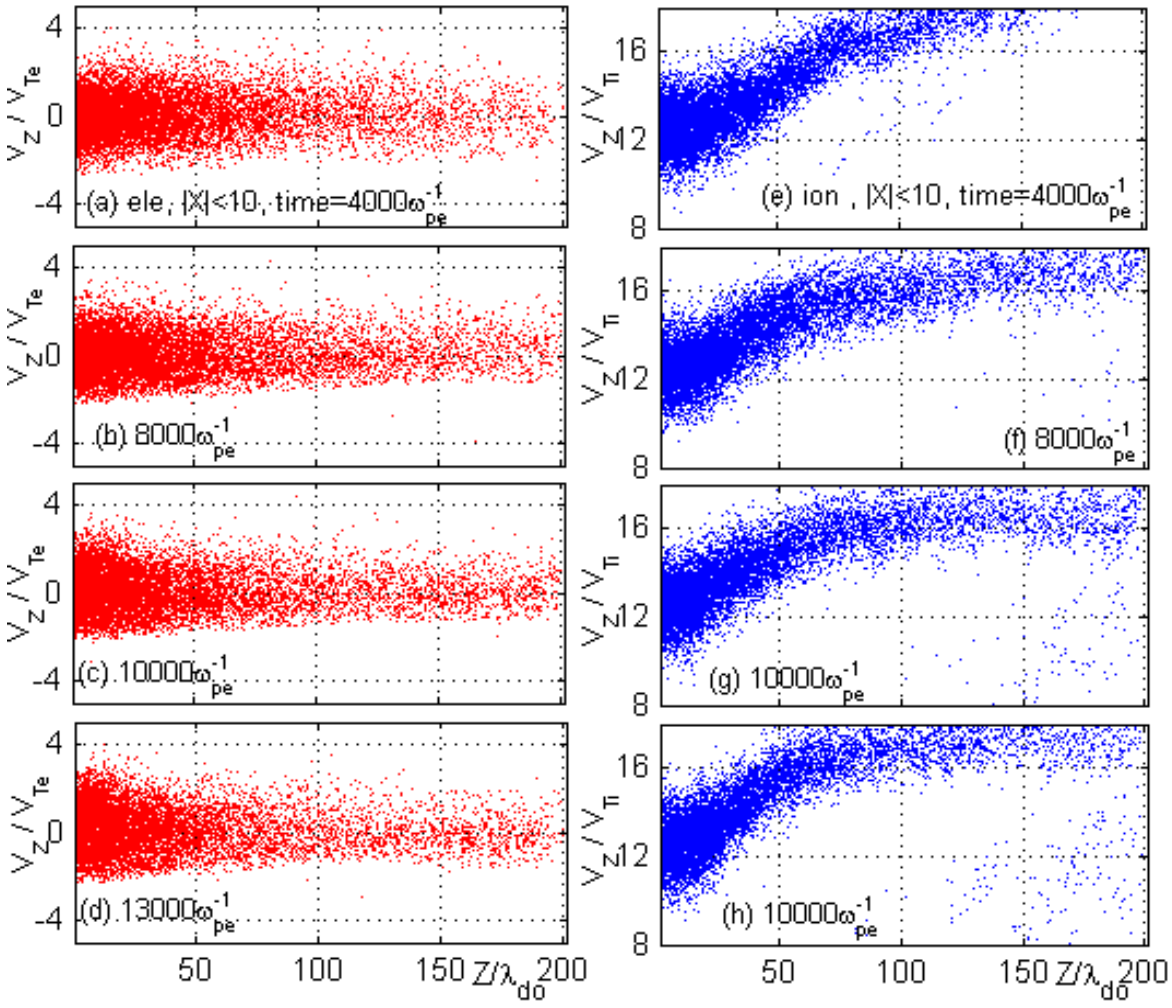

Figure 4.17: Z-V_Z phase plot for ions (blue) and electrons (red) at different times for the region |X|<10.

In Figure 4.18, X-V_Z phase plot of electrons and ions are shown. The ion injection velocity in the axial direction is marked by a dashed line. We can see that there is net axial acceleration in the ions for |X|<30.

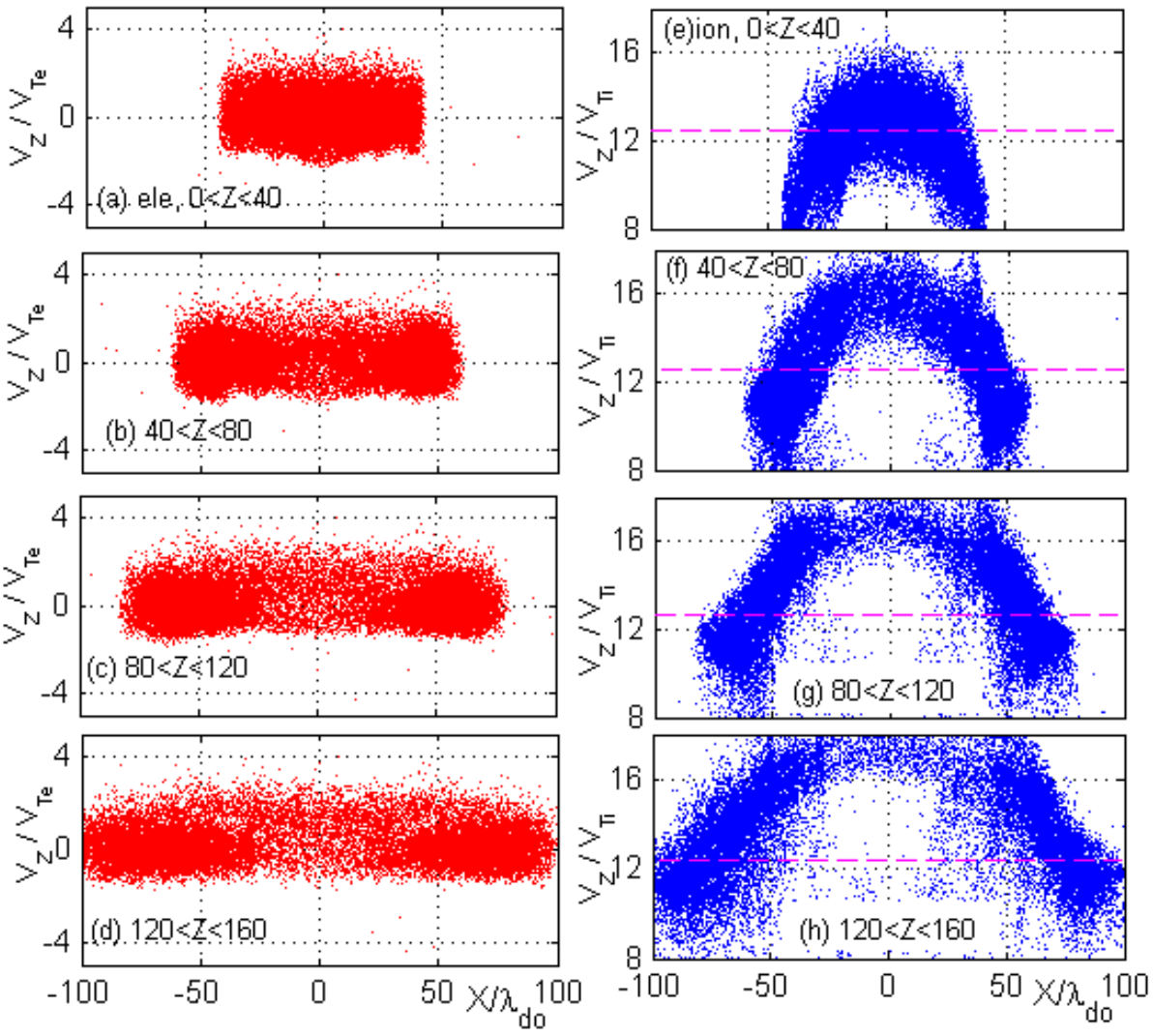

Figure 4.18: X-V_Z phase plot for ions (blue) and electrons (red) at different times for the region |X|<10

There are two populations of ions: a) ions in the conical surface and b) ions along axial direction (|X|<30, 0<Z<200). Only the axially accelerated ions in the central region of the simulation box (|X|<30, 0<Z<200) provide the useful thrust needed for the propulsion in the HDLT. Only a small portion of injected ions remain in the central region (|X|<30, 0<Z<200) because most of the ions flow into the cone. We can also note that the ions along the cone are not axially accelerated and hence these ions are not useful

for the thrust generation. Figure 4.19 shows the two-dimensional velocity distribution function of the ions before ($0 < z < 50$) and after ($80 < z < 120$) the acceleration by the double layer in the narrow axial region ($|x| < 10$). The ions injected at the PIW (Figure 4.19 (a)) have broad distributions covering the velocity range $10 < V_Z/V_{Ti} < 16$ and $|V_X| < 4V_{Ti}$. After the axial acceleration by the double layer, the mean axial velocity has increased to $V_z \sim 17\ V_{Ti}$ and the spread in $|V_X|$ has decreased to $\sim 3.0\ V_{Ti}$, indication that the accelerated ions in the axial region are a cold beam.

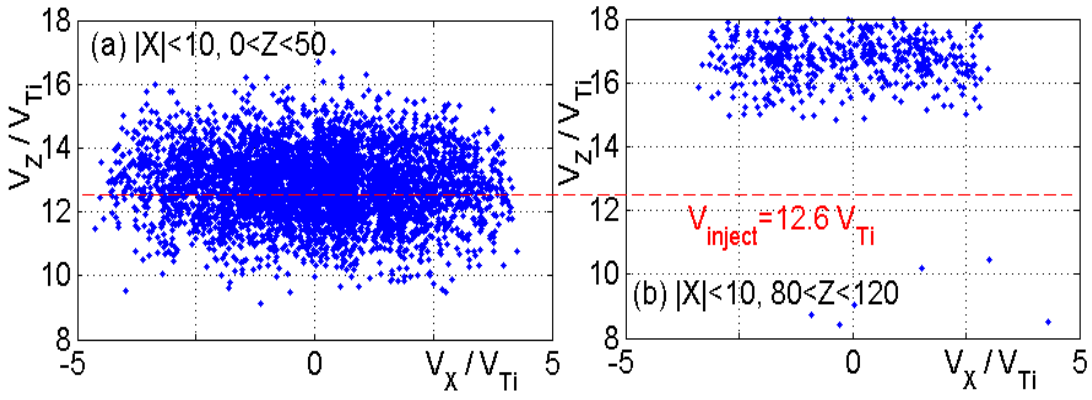

Figure 4.19: Comparison of V_Z -V_X phase space for ions in the region (a) below the DL ($0 < Z < 50$), (b) above the DL ($80 < Z < 120$); both for $|X| < 10$

4.2 VARYING THE DIVERGENCE OF MAGNETIC FIELD

We performed two simulations with different divergence in the magnetic field. In the first simulation, we placed the solenoid closer to the simulation box ($d = 15\lambda_{do}$) which produced high diverging magnetic field and in the second simulation, we placed the solenoid away from the simulation box ($d = 65\lambda_{do}$) which resulted in a less diverging magnetic field. In both simulations, we chose $N_X = N_Z = 100$. If the magnetic field is

diverging at a faster rate, then the conical density structure also diverges at a faster rate (Figure 4.21). This is because, electrons are always tied to the magnetic field and ions follow electrons. Rapidly diverging density structure results in rapid reduction of plasma density with increasing axial distance. As a result, we observe axially elongated double layer as in Figure 4.20. Same simulation with a less diverging magnetic field results in a shrunken double layer as in Figure 4.22. Also in a less diverging magnetic field, density may be higher in the conical surface (7<X<15, 20<Z<40) than at the source (|X|<20, 0<Z<5) as seen in Figure 4.23, but this is not the case with the high diverging case where density is always less in the surface of the cone compared to density at the source (Figure 4.21). Also, in high diverging case plasma exits the simulation box at a shorter axial distance, compared to low diverging case.

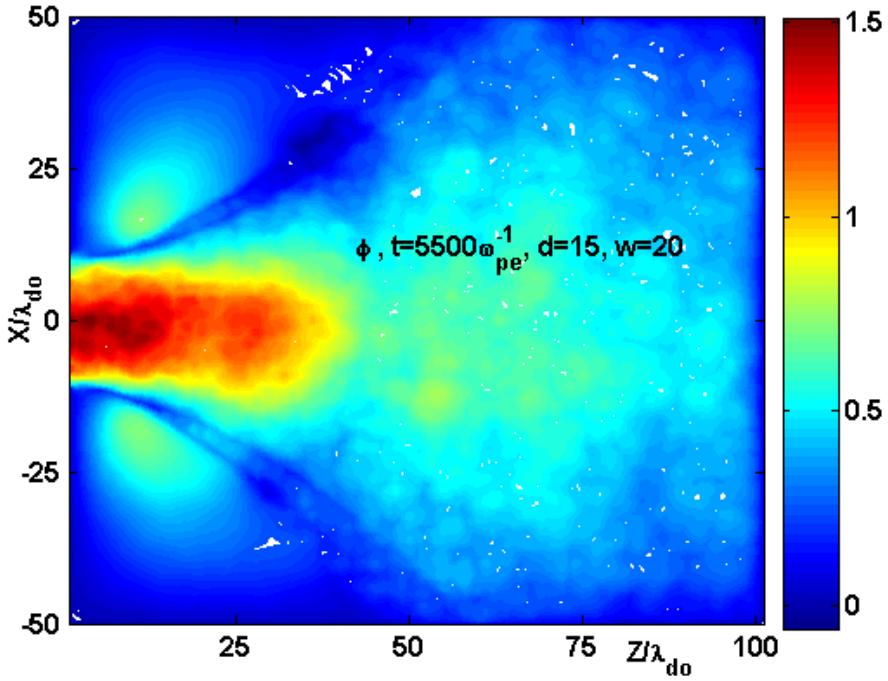

Figure 4.20: ϕ for high divergence in magnetic field $(N_X = N_Z = 100)$

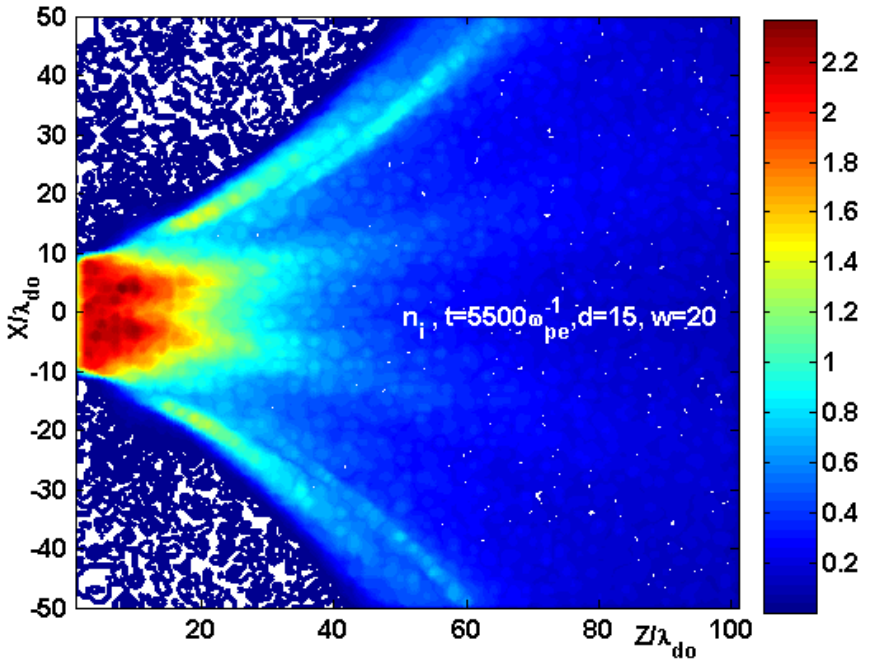

Figure 4.21: n_i for high divergence in magnetic field $(N_X = N_Z = 100)$

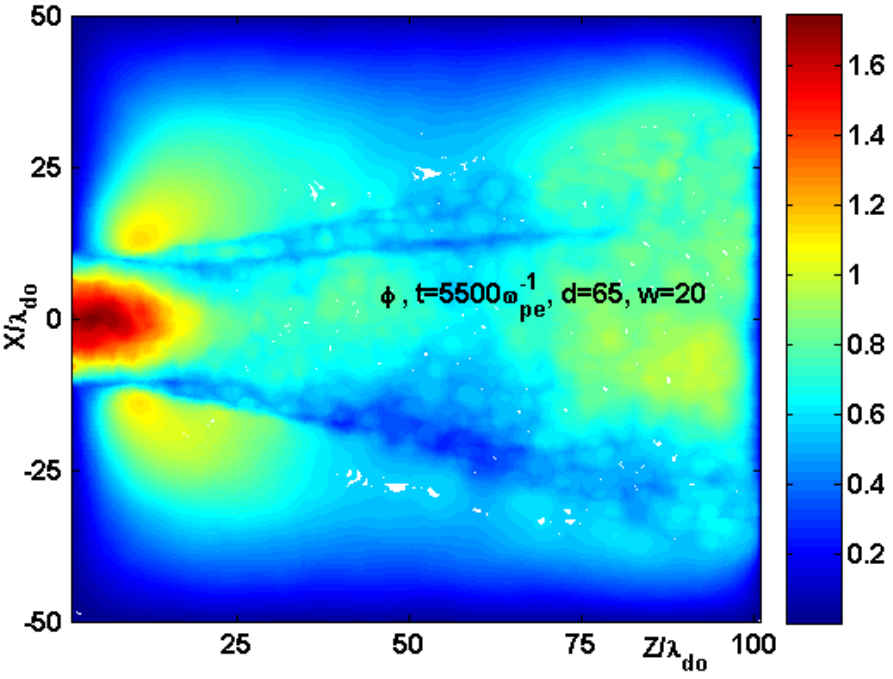

Figure 4.22: ϕ for low divergence in magnetic field $(N_X = N_Z = 100)$

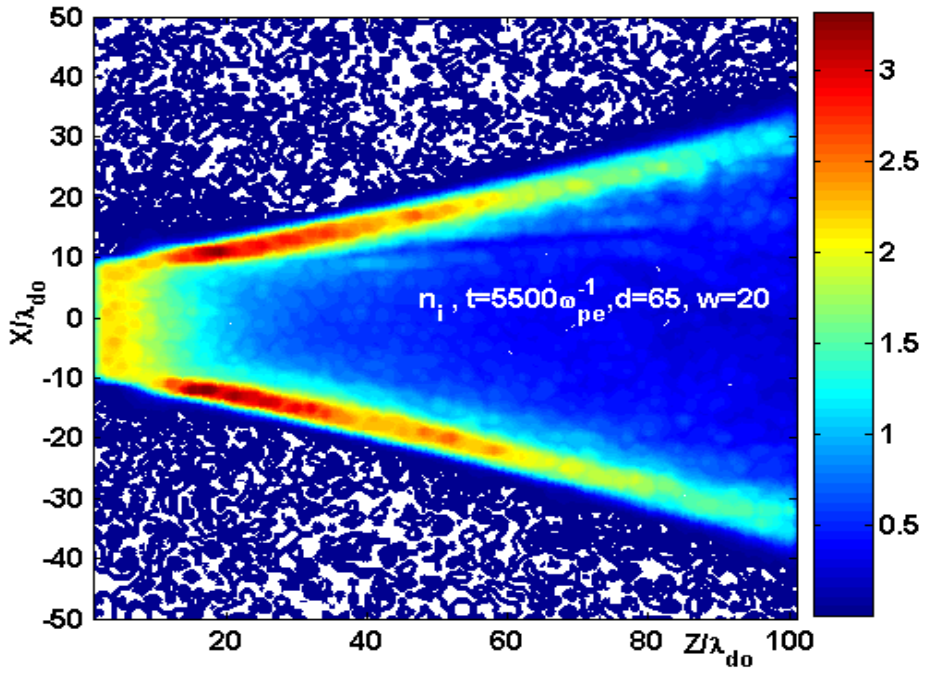

Figure 4.23: n_i for low divergence in magnetic field $(N_X = N_Z = 100)$

4.3 VARYING THE WIDTH OF PIW

A broader PIW injects more particles into the simulation box. hence, simulation with larger PIW reaches steady state slower than the simulation with narrow PIW. We investigate the effect of widening or narrowing the PIW width on the DL. Length of simulation box is fixed ($N_X = N_Z = 201$). The first simulation has a PIW width of w=40 and the second simulation has w=60. Figure 4.24 shows the electric potential for w=40 and Figure 4.25 shows the electric potential for w=60. We can notice that the potential drop across the DL is same in both the figures. The length of the DL is $50\lambda_{do}$ in both the cases.

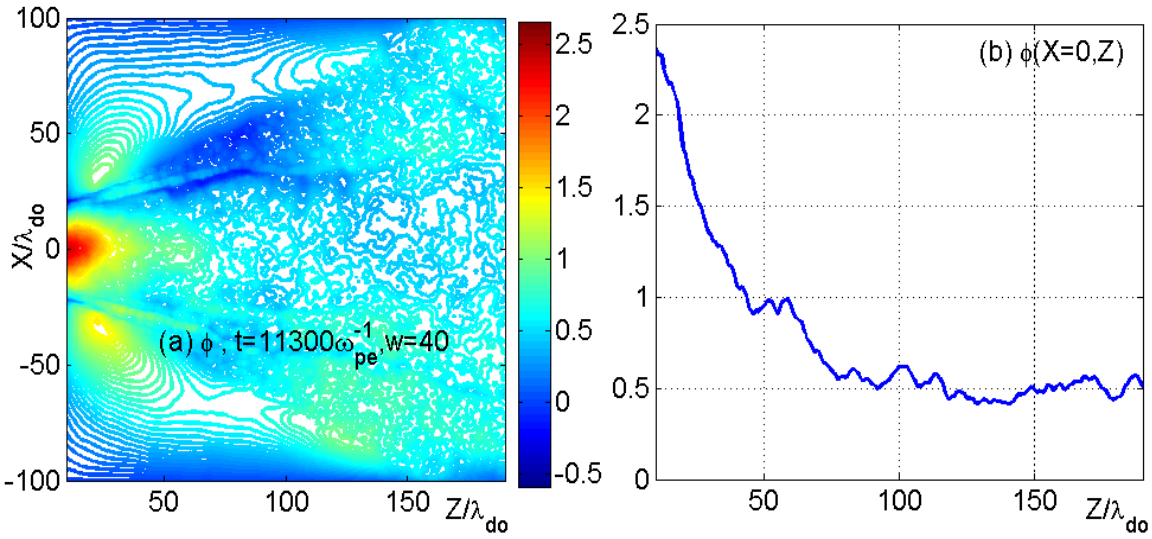

Figure 4.24: (a) Color map of ϕ for w=40 at t=11300 ω_{pe}^{-1} and (b) $\phi(X=0,Z)$.

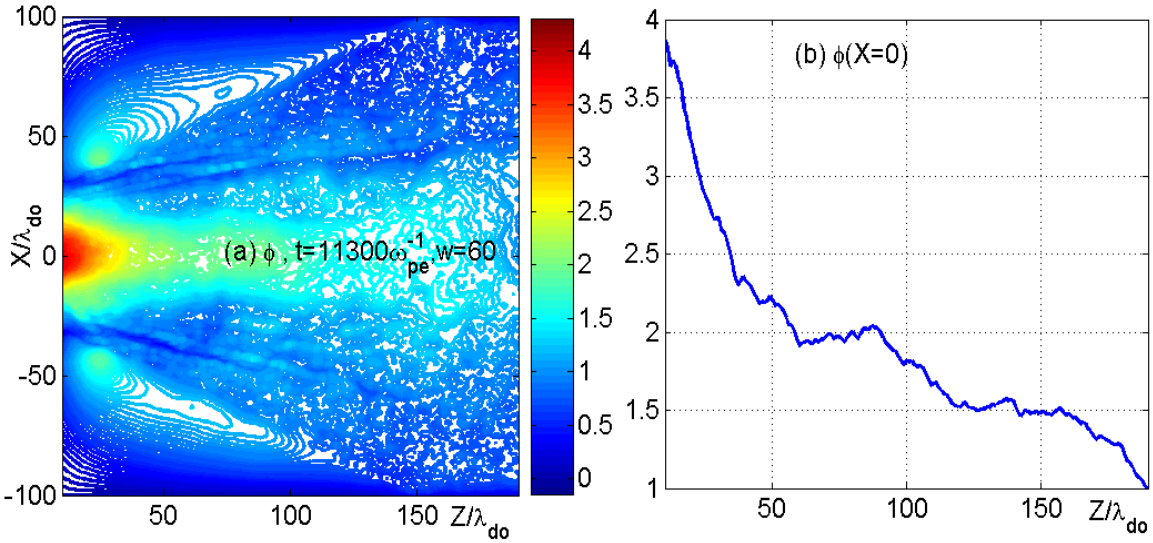

Figure 4.25: (a) Color map of ϕ for w=60 at t=11300 ω_{pe}^{-1} and (b) $\phi(X=0,Z)$.

4.4 COMPARISONS WITH ANU EXPERIMENTS

In this section, we briefly compare our simulation results with the experiments of ANU group [3, 14]. Figure 4.26 shows the electric potential distribution near the interface of source and diffusion chamber observed by Charles in the Helicon Plasma Device [3]. Figure 4.27 shows the potential distribution near the PIW from our simulation. By visually inspecting both the figure, we can see that they have similar structures such as: (a) both figures have U-shaped double layer anchored to the PIW, (b) both figures have side lobe structures as discussed in section 4.1. Next we compare the density structure. Figure 4.28 shows the density profile in the actual experiment, while Figure 4.5 shows the density profile in our simulation. Notice that in both case, we observe a conical structure in the density. Figure 4.29 and Figure 4.30 shows the perpendicular and parallel electric field observed in the experiment. From Figure 4.31 (d), the maximum parallel electric field E_z in our simulation is $0.04(T_e/\lambda_{do})$. Substituting the experimental parameters such as T_e =8eV and λ_{do}=0.13mm, we get maximum E_z=1000 V/m, which is in excellent agreement with Figure 4.30. Figure 4.29 show that the maximum radial electric field in the experiment is $E_\perp \sim$ 2200 V/m. In our simulation, $E_\perp \sim 0.1(T_e/\lambda_{do}) = 2{,}500$ V/m as seen from Figure 4.31(b). These values of the simulated and measured electric fields in a CFDL are in remarkably good agreements. Figure 4.32 shows electron energy distribution functions near the cone surface ($30 < x < 50$ and $30 < z < 70$). We can notice that, electron energy distribution in the cone is developing into two population; colder population has temperature $T_1 \sim 0.42T_e$ and the warmer one has $T_2 \sim 0.6\ T_e$. The electron energy distribution in our simulation has qualitatively same

features as that of experiments as seen from Figure 4.33. The energetic tail in the simulation develops due to electron heating by the ion beam driven instabilities. The electrons in the energetic tail are the hot electrons seen in Figure 4.16 (a) to (d).

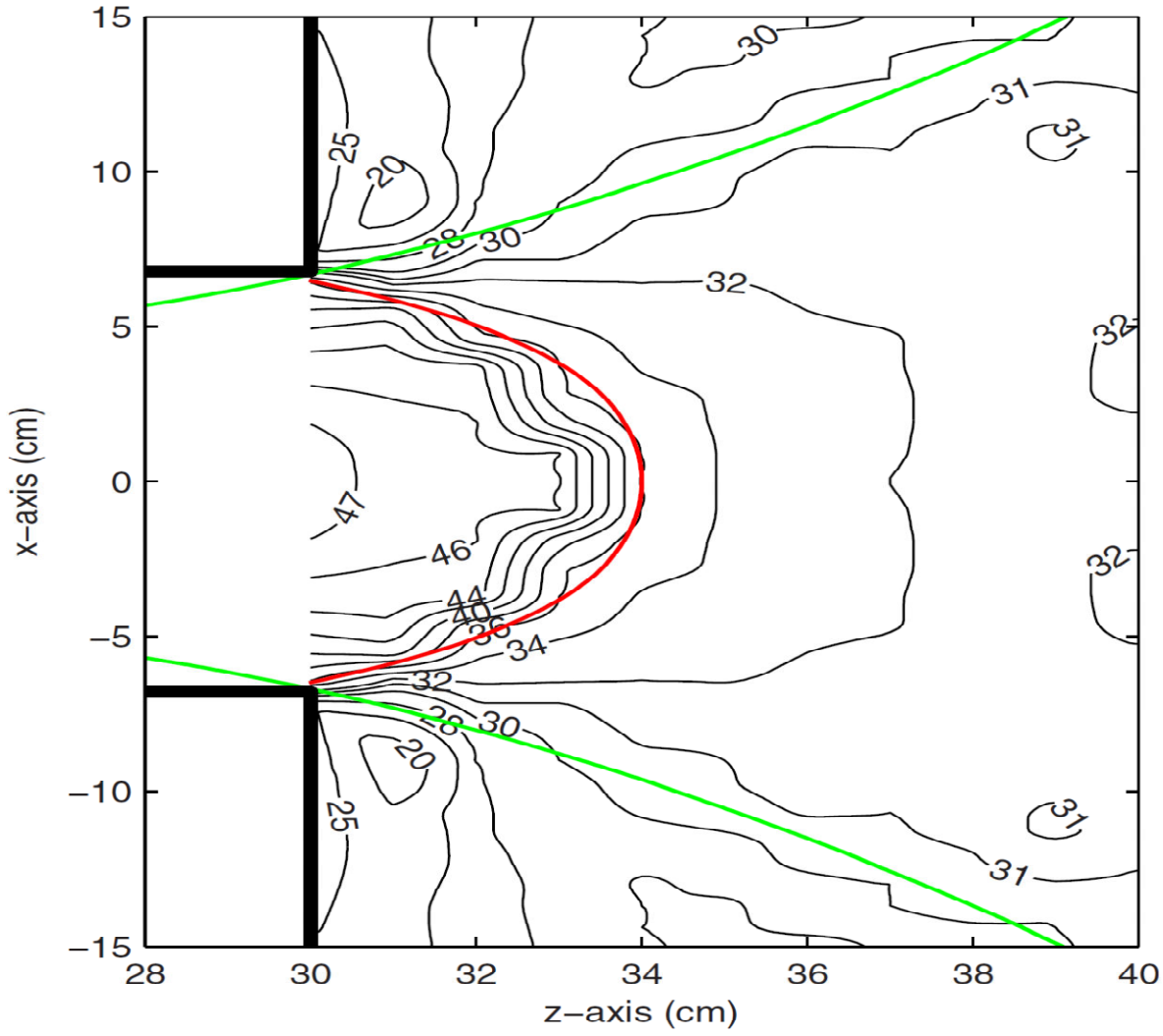

Figure 4.26: Equipotential contours observed in the Helicon Plasma Device. Reprinted Figure 2 with permission from C. Charles, High density conics in a magnetically expanding helicon plasma, Vol. 96, 051502, 2010. Copyright 2010, American Institute of Physics.

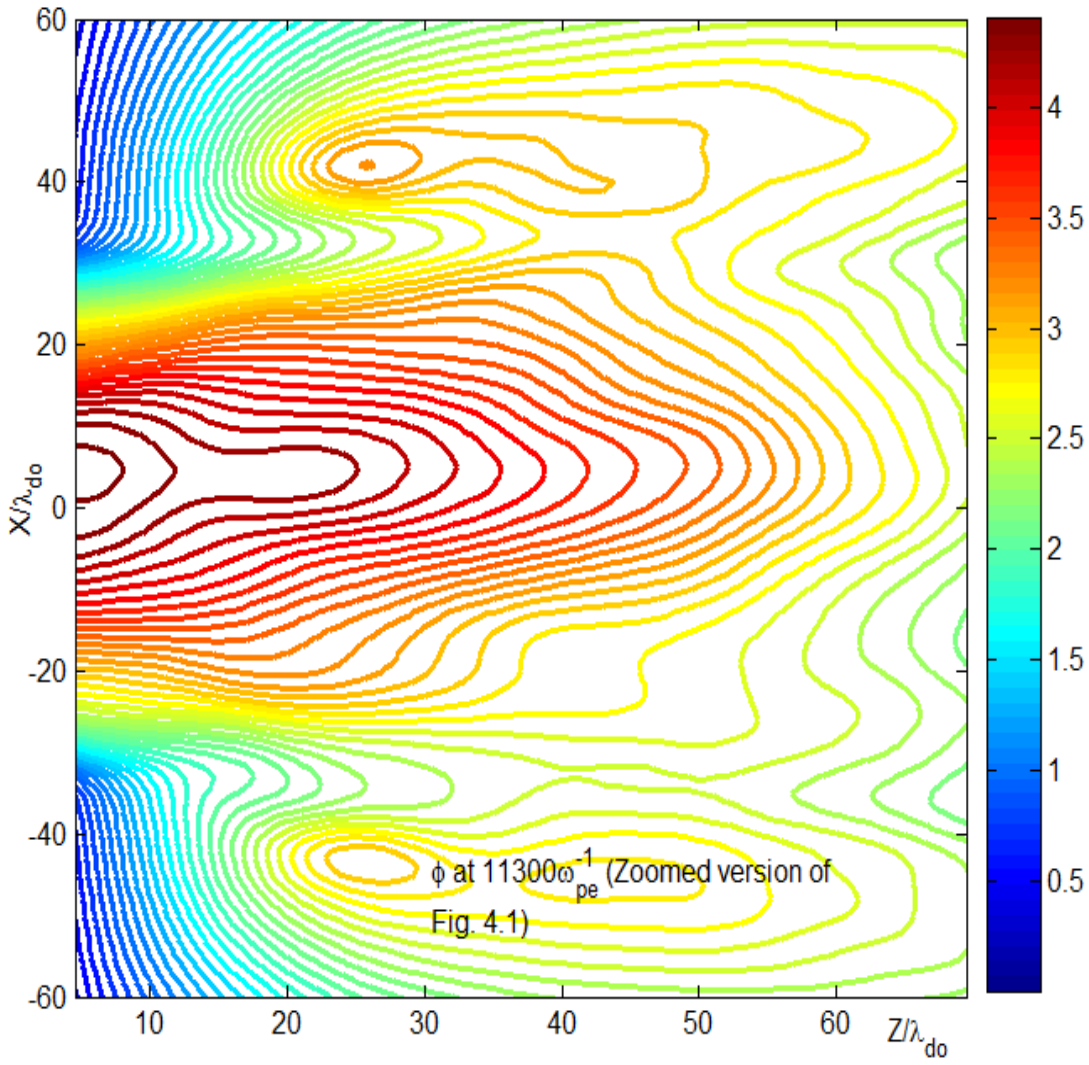

Figure 4.27: Equipotential contour map of ϕ near the PIW

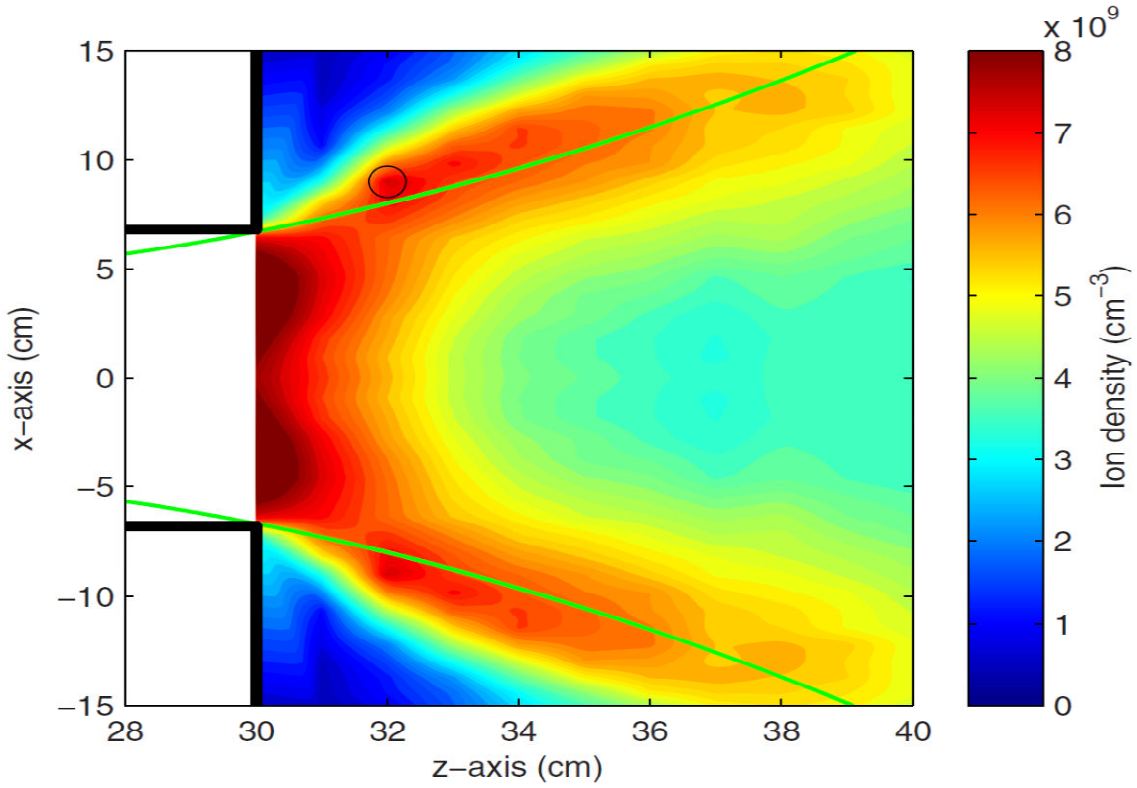

Figure 4.28: Contours of ion density observed in the HPD. Reprinted Figure3 with permission from C. Charles, High density conics in a magnetically expanding helicon plasma, Vol. 96, 051502, 2010. Copyright 2010, American Institute of Physics.

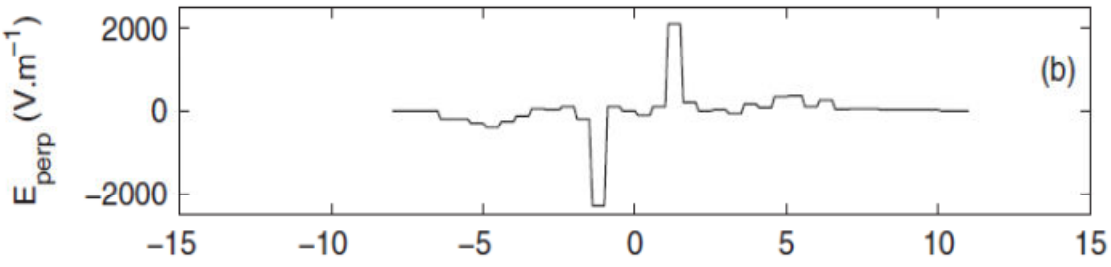

Figure 4.29: Radial electric field derived from the measured electric potential. Reprinted Figure 4(b) with permission from [C. Charles, R.W. Boswell and R. Hawkins, Oblique Double Layers: A Comparison between Terrestrial and Auroral Measurements, PRL 103, 095001, 2009]. Copyright (2009) by the American Physical Society.

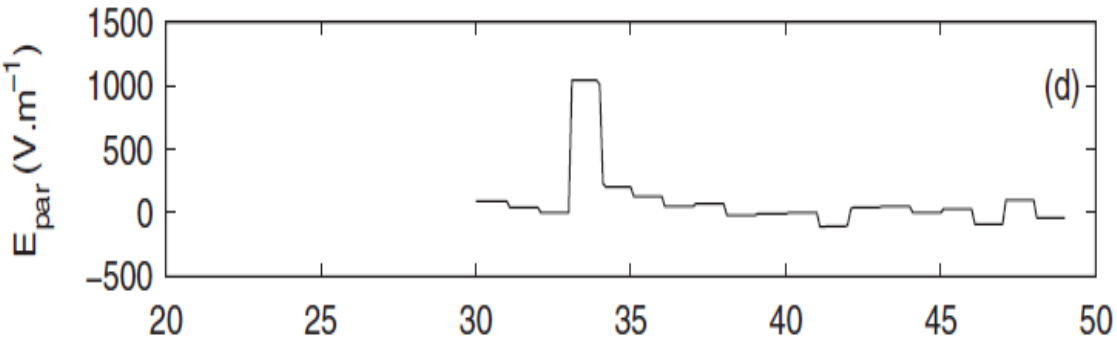

Figure 4.30: Parallel Electric Field derived from the measured Electric Potential. Reprinted Figure 4(d) with permission from [C. Charles, R.W. Boswell and R. Hawkins, Oblique Double Layers: A Comparison between Terrestrial and Auroral Measurements, PRL 103, 095001, 2009]. Copyright (2009) by the American Physical Society.

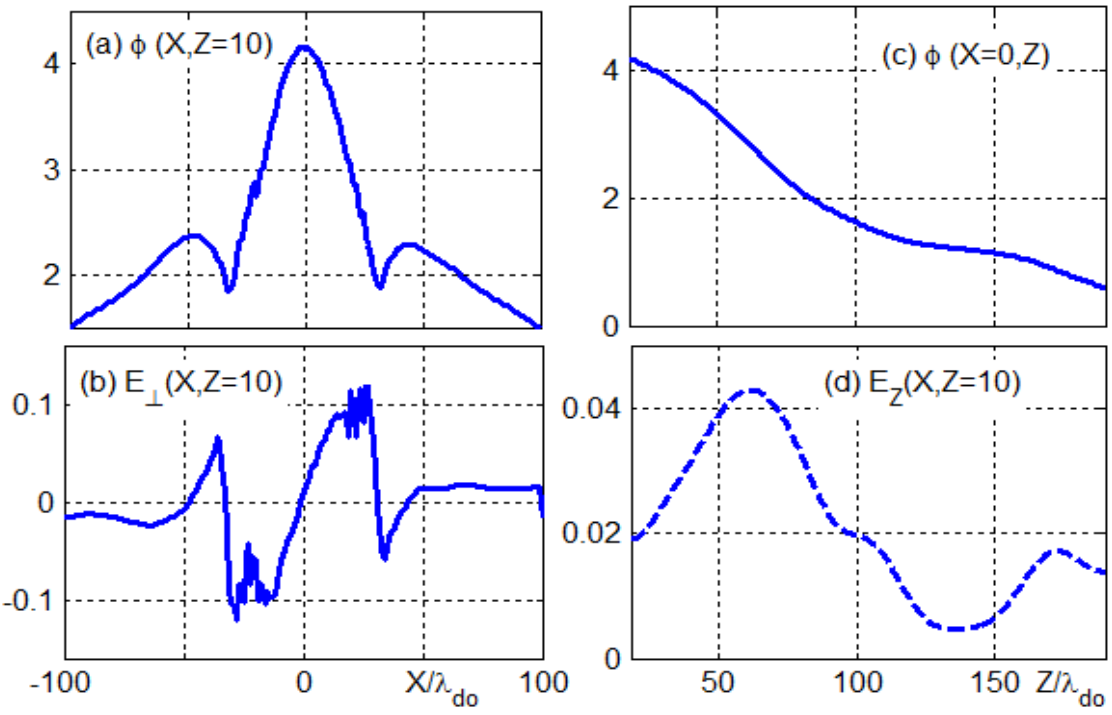

Figure 4.31: (a) $\phi(X, Z = 10)$,(b) $E_{\perp}(X, Z = 10)$,(c) $\phi(X = 0, Z)$ and (d) $E_Z(X = 0, Z)$; all at time=11300 ω_{pe}^{-1}

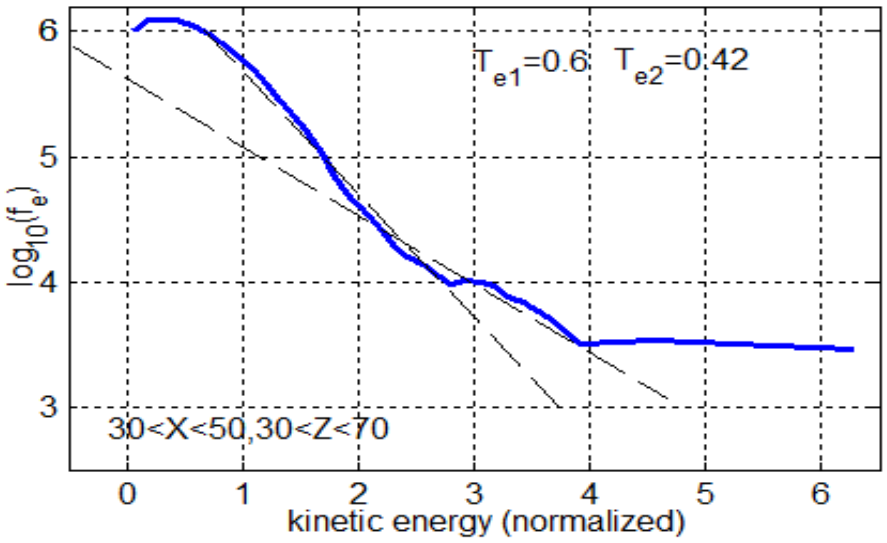

Figure 4.32: Electron energy distribution functions at the surface of the cone (30 < X <50 and 30 < Z< 70) for w=60, d=65, and $N_X = N_Z = 201$

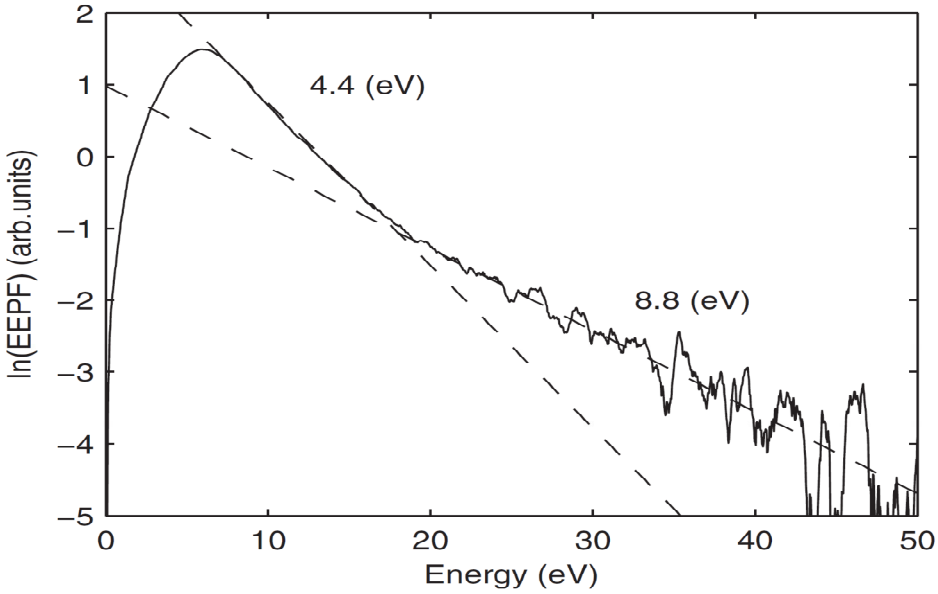

Figure 4.33: Electron Energy Distribution in the high density conic. Reprinted Figure 4 with permission from C. Charles, High density conics in a magnetically expanding helicon plasma, Vol. 96, 051502, 2010. Copyright 2010, American Institute of Physics.

CHAPTER 5

CONCLUSIONS

5.1 DISCUSSION AND CONCLUSIONS

In this thesis, two-dimensional electrostatic particle in cell simulation method has been applied to the study of double layer formation in diffusion chamber of the helicon plasma device. Poisson equation was solved using successive over relaxation method. Magnetic field of a solenoid was calculated using Biot Savart's law as described in Chapter 3. In Chapter 4, the numerical simulation results were presented. The main results of this thesis are the following. We theoretically verified the formation of U-shaped double layer in a Helicon Plasma Device (HPD). The results of the simulations reveal that the fields and the plasma in the HPD double layers are dominated by the kinetic behavior of the plasma expanding in a highly diverging magnetic field. One dimensional models as in [13, 21] fails to account the effect of perpendicular acceleration of ions shown in Figure 4.15 (b). Right at the injection, where the source plasma flows into the simulation box, the magnetized electrons and unmagnetized ions tend to flow differently, causing large perpendicular electric fields. Magnetized electron experience J_d x B force near the PIW due to the generation of perpendicular electric fields. The J_d x B force then pushes electrons into the cone. Electrons which are then tied to the magnetic field lines move in a conical form. Ions are pulled by the $E_\perp$, thus forming conical density structure in HPD

as shown in Figure 4.5 and 4.6. Vortexes in ion flow resulting from perpendicular acceleration of ions were shown in Figure 4.16. These structures are yet to be measured in HPD. Our simulations revealed that ions in the vicinity of the conical surfaces are much warmer in perpendicular direction compared to those flowing in the axial direction after acceleration in the double layer. Dumbbell structures of electron flow as in Figure 4.16 show that the conical surface consists of heated electrons in radial direction. We found that integral of density along axial direction was approximately conserved as in Figure 4.7. This indicates that plasma from the source self consistently distributes into the conical structure. The presence of high frequency and low frequency plasma oscillations were observed in the electric potential ϕ as shown in Figure 4.9 and 4.10. By averaging over one ion acoustic period, most of these fluctuations were removed. Dependence of ϕ and conical density structure on the divergence of the magnetic field was presented in Section 4.2. We found that the length of double layer depends on the magnetic field divergence. In the high diverging magnetic field, DL was elongated in axial direction compared to low diverging case. Also in Figure 4.25, we observed that the potential drop in the double layer ϕ_{DL} is invariant of PIW width. We have approximated cylindrical geometry of the HPD to rectangular coordinates. Despite this simplification, we are able to observe most of the experimentally measured features as discussed in section 4.4.

In summary, by means of Particle-in-Cell (PIC) simulations, we have verified the formation of electric double layers and conical density structures as observed in the experiments [3]. Some new features such as vortexes in ion flow and oscillations in electric potential are predicted by the simulations. The effect of instabilities on the performance of Helicon Double Layer Thruster remains to be studied.

5.2 RECOMMENDATIONS FOR FUTURE WORK

The first extension of this work would be to solve this problem in cylindrical coordinate system and to incorporate the effect of ion neutral collision in PIC code. Second possible extension would be to convert the problem to 3-dimensions. This requires more computational resources and hence parallelizing the code would be the fourth extension of this work. Plasma oscillations and effect of plasma instability can be studied in detail. This requires a larger simulation box. In this work, we have modeled only the diffusion region of the Helicon Plasma Device. Modeling the entire HPD including the source chamber and the helical antenna would be an interesting problem.

APPENDIX A

2D ELECTROSTATIC PIC CODE

```
CCCCCCCCCCCCCCCCCCCCCCCCCCCCCCCCCCCCCCCCCCCCCCCCCCCCCCCCCC
C 2-d Electro static code to implement diffusion region of
C Helicon plasma device. Numerical simulation of current free
C double layers.
CCCCCCCCCCCCCCCCCCCCCCCCCCCCCCCCCCCCCCCCCCCCCCCCCCCCCCCCCC
C Basic blocks of the code
C SET   - Initialization of ambient magnetic field
C COIL - Calculates magnetic field of a single circular coil
C MOVEE- Solves the equation of motion for electrons
C MOVEI- Solves the equation of motion for ions
C BEGIN- Injects particles through the PIW
C POISSON- Solves poisson equation
C INITIA- Initializes the simulation box with background plasma
CCCCCCCCCCCCCCCCCCCCCCCCCCCCCCCCCCCCCCCCCCCCCCCCCCCCCCCCCC
INCLUDE 'bounds.h'
REAL ION
COMMON/PAR/ELE(NM_PRTS,5),ION(NM_PRTS,5)
COMMON/ARRAY1/PHI(X_GRD,Y_GRD)
COMMON/EFIELD/EX(X_GRD,Y_GRD),EY(X_GRD,Y_GRD)
COMMON/ARRAY/RHO(X_GRD,Y_GRD),RHOE(X_GRD,Y_GRD),
RHOI(X_GRD,Y_GRD)
COMMON/VEX/XX(X_GRD),YY(Y_GRD)
COMMON/TIM/ TIME,TPI,PI
COMMON/ANUM/ NX,NY,NX1,NY1,MAIN,NIJ,GAP1,GAP2,GD
COMMON/VARP/ RATO,DELT
COMMON/FLUXB/BZM(X_GRD,Y_GRD),BYM(X_GRD,Y_GRD),
BXM(X_GRD,Y_GRD),
&  BYMC(X_GRD,Y_GRD),BXMC(X_GRD,Y_GRD)
COMMON/AMIS/ ISEED,DY,DX,NIID,NEED,NSUME,NSUMI
COMMON/ANUM1/N_COIL,RADIUS
INTEGER IND,KVAR1,KVAR3,KVAR2,T_HIS
REAL EL(NM_PRTS,5),IN(NM_PRTS,5)
REAL PAVG(X_GRD,Y_GRD)
REAL Phis1(300000,10)
nit =300000
NX=X_GRD
NY=Y_GRD
NX1=NX-1
NY1=NY-1
```

```
N_COIL=250
PI=3.14159265358979
ISEED=987654321
TPI=2.*PI
P0=0.
SCALE=10
NIJ=100
RATO = 1.0/1600.
DELT=TPI/64.
TSTART = 0
GAP1=(INT(Nx1/2)+1)-30
GAP2=(INT(Nx1/2)+1)+30
GD=INT(GAP2-GAP1)
TMAX =1
ITST = INT(TSTART)
c      No of time steps=NIT
c      NIT tells you how long your code is going to run
CCCCCCCCCCCCCCCCCCCCCCCCCCCCCCCCCCCCCCCCCCCCCCCCCCCCCCCCCC
NIID=0
NEED=0
CALL SET
CALL OUT2DR('BY',1,NX,NY,BYM)
CALL OUT2DR('BX',1,NX,NY,BXM)
CALL INITIA
TIME=TSTART
LWRTE = 1
LC = 0
LFD=0
T_HIS=0
c     how often you write data files is given by LF*DELT
LF=2000
LAC=10
CCCCCCCCCCCCCCCCCCCCCCCCCCCCCCCCCCCCCCCCCCCCCCCCCCCCCCCCCC
DO 1111 I=1,NX
DO 1111 J=1,NY
EX(I,J)=0.
EY(I,J)=0.
PAVG(I,J)=0.
1111   CONTINUE
OPEN(UNIT=95,FILE='phi1a',STATUS='NEW')
OPEN(UNIT=96,FILE='phi1b',STATUS='NEW')

DO 1 MAIN=0,NIT
TIME=TIME+DELT
T_HIS=T_HIS+1
LC = LC + 1
```

```
LFD=LFD+1
CCCCCCCCCCCCCCCCCCCCCCCCCCCCCCCCCCCCCCCCCCCCCCCCCCCCCC
CCCC
CALL BEGIN
CALL DENS
CALL POISSON
C time history of electric potential
phis1(T_HIS,1)=MAIN
phis1(T_HIS,2)=phi((Nx1/2)+1,5)
phis1(T_HIS,3)=phi((Nx1/2)+1,20)
phis1(T_HIS,4)=phi((Nx1/2)+1,40)
phis1(T_HIS,5)=phi((Nx1/2)+1,60)
phis1(T_HIS,6)=phi((Nx1/2)+1,90)
phis1(T_HIS,7)=phi((Nx1/2)+1,120)
phis1(T_HIS,8)=phi((Nx1/2)+1,140)
phis1(T_HIS,9)=phi((Nx1/2)+1,150)
phis1(T_HIS,10)=phi((Nx1/2)+1,170)
WRITE(95,*)(phis1(T_HIS,J),J=1,5)
WRITE(96,*)(phis1(T_HIS,J),J=6,10)
DO I=1,X_GRD
DO J=1,Y_GRD
PAVG(I,J)=PHI(I,J)+PAVG(I,J)
END DO
END DO
CCCCCCCCCCCCCCCCCCCCCCCCCCCCCCCCCCCCCCCCCCCCCCCCCCCCCC
CALL FIELD
CALL MOVEI
CALL MOVEE
IF(LFD.EQ.LF)THEN
IND=MAIN/LF
KVAR1=NIID/20
KVAR2=NEED/20
KVAR3=1
DO L=1,KVAR1
IF(KVAR3.LT.NIID) THEN
DO J=1,5
IN(L,J)=ION(KVAR3,J)
END DO
KVAR3=KVAR3+20
END IF
END DO
KVAR3=1
DO L=1,KVAR2
IF(KVAR3.LT.NEED) THEN
DO J=1,5
EL(L,J)=ELE(KVAR3,J)
```

```
END DO
KVAR3=KVAR3+20
END IF
END DO
DO I=1,X_GRD
DO J=1,Y_GRD
PAVG(I,J)=PAVG(I,J)/LF
END DO
END DO
CALL OUT2DR('pavg',IND,NX,NY,PAVG)
CALL OUTINFO ('info',IND,TIME,NEED,NIID)
CALL OUT2DR('phi_',IND,NX,NY,PHI)
CALL OUT2DR('rhoi',IND,NX,NY,RHOI)
CALL OUT2DR('rhoe',IND,NX,NY,RHOE)
CALL OUT2DR('rho_',IND,NX,NY,RHO)
CALL OUTPRT ('ele_',IND,KVAR2,EL)
CALL OUTPRT ('ion_',IND,KVAR1,IN)
LFD=0
DO I=1,X_GRD
DO J=1,Y_GRD
PAVG(I,J)=0.0
END DO
END DO
ENDIF
1     CONTINUE
CLOSE(95)
CLOSE(96)
STOP
END
C ************************************************
SUBROUTINE FIXFILENM(NAMEIN,NAMEOUT)
CHARACTER*9 NAMEIN,NAMEBUF,NAMEOUT
NAMEBUF = NAMEIN
DO 3 I=1,LEN(NAMEBUF)
IF (NAMEBUF(I:I) .EQ. ' ') NAMEBUF(I:I) = '0'
IF (NAMEBUF(I:I) .EQ. '+') NAMEBUF(I:I) = '_'
3     CONTINUE
NAMEOUT = NAMEBUF
RETURN
END
C ***************************************************************
SUBROUTINE OUTPRT (FNAME,IDX_NM,IPRT,ARRY)
INCLUDE 'bounds.h'
REAL ARRY(NM_PRTS,5)
CHARACTER*9 NAME
CHARACTER *4 FNAME
```

```
WRITE(NAME,'(A4,A1,I4)')FNAME,'_',IDX_NM
CALL FIXFILENM(NAME,NAME)
OPEN(UNIT=2,FILE=NAME,STATUS='OLD',ERR=2)
CLOSE(2)
OPEN(UNIT=2,FILE=NAME,STATUS='OLD',DISP='DELETE')
CLOSE(2)
2     OPEN(UNIT=2,FILE=NAME,STATUS='NEW')
DO 1 I=1,IPRT
WRITE(2,*)(ARRY(I,J),J=1,5)
1       CONTINUE
CLOSE(2)
RETURN
END
C ***************************************************************
SUBROUTINE OUTINFO (FNAME,IND,TIME,NEED,NIID)
CHARACTER*9 NAME
CHARACTER *4 FNAME
WRITE(NAME,'(A4,A1,I4)')FNAME,'_',IDX_NM
CALL FIXFILENM(NAME,NAME)
OPEN(UNIT=2,FILE=NAME,STATUS='OLD',ERR=2)
CLOSE(2)
OPEN(UNIT=2,FILE=NAME,STATUS='OLD',DISP='DELETE')
CLOSE(2)
2     OPEN(UNIT=2,FILE=NAME,STATUS='NEW')
WRITE(2,*),IND,TIME,NEED,NIID
CLOSE(2)
RETURN
END
C ***************************************************************
SUBROUTINE OUT2DR (FNAME,IDX_NM,IX,IY,ARRY)
INCLUDE 'bounds.h'
REAL ARRY(X_GRD,Y_GRD)
CHARACTER*9 NAME
CHARACTER *4 FNAME
WRITE(NAME,'(A4,A1,I4)')FNAME,'_',IDX_NM
CALL FIXFILENM(NAME,NAME)
OPEN(UNIT=2,FILE=NAME,STATUS='OLD',ERR=2)
CLOSE(2)
OPEN(UNIT=2,FILE=NAME,STATUS='OLD',DISP='DELETE')
CLOSE(2)
2     OPEN(UNIT=2,FILE=NAME,STATUS='NEW')
DO 1 I=1,IX
DO 154 J=1,IY
WRITE(2,*) I,J,ARRY(I,J)
154    CONTINUE
1     CONTINUE
```

```
CLOSE(2)
RETURN
END
C     ************************************************************
SUBROUTINE SET
C     ************************************************************
INCLUDE 'bounds.h'
REAL ION
COMMON/PAR/ELE(NM_PRTS,5),ION(NM_PRTS,5)
COMMON/ARRAY1/PHI(X_GRD,Y_GRD)
COMMON/EFIELD/EX(X_GRD,Y_GRD),EY(X_GRD,Y_GRD)
COMMON/ARRAY/RHO(X_GRD,Y_GRD),RHOE(X_GRD,Y_GRD),
RHOI(X_GRD,Y_GRD)
COMMON/VEX/XX(X_GRD),YY(Y_GRD)
COMMON/TIM/ TIME,TPI,PI
COMMON/ANUM/ NX,NY,NX1,NY1,MAIN,NIJ,GAP1,GAP2,GD
COMMON/VARP/ RATO,DELT
COMMON/FLUXB/BZM(X_GRD,Y_GRD),BYM(X_GRD,Y_GRD),
BXM(X_GRD,Y_GRD),
&  BYMC(X_GRD,Y_GRD),BXMC(X_GRD,Y_GRD)
COMMON/AMIS/ ISEED,DY,DX,NIID,NEED,NSUME,NSUMI
COMMON/ANUM1/N_COIL,A,RADIUS
REAL BXQ1(X_GRD,Y_GRD),BYQ1(X_GRD,Y_GRD)
REAL BXQ2(X_GRD,Y_GRD),BYQ2(X_GRD,Y_GRD)
REAL BXQ3(X_GRD,Y_GRD),BYQ3(X_GRD,Y_GRD)
REAL BXQ4(X_GRD,Y_GRD),BYQ4(X_GRD,Y_GRD)
REAL BXQ5(X_GRD,Y_GRD),BYQ5(X_GRD,Y_GRD)
REAL BXQ6(X_GRD,Y_GRD),BYQ6(X_GRD,Y_GRD)
REAL BXQ7(X_GRD,Y_GRD),BYQ7(X_GRD,Y_GRD)
REAL BXQ8(X_GRD,Y_GRD),BYQ8(X_GRD,Y_GRD)
REAL BXQ9(X_GRD,Y_GRD),BYQ9(X_GRD,Y_GRD)
REAL BXQ10(X_GRD,Y_GRD),BYQ10(X_GRD,Y_GRD)
REAL BXQ11(X_GRD,Y_GRD),BYQ11(X_GRD,Y_GRD)
REAL BXQ12(X_GRD,Y_GRD),BYQ12(X_GRD,Y_GRD)
REAL BXQ13(X_GRD,Y_GRD),BYQ13(X_GRD,Y_GRD)
REAL BXQ14(X_GRD,Y_GRD),BYQ14(X_GRD,Y_GRD)
REAL BXQ15(X_GRD,Y_GRD),BYQ15(X_GRD,Y_GRD)
REAL BXQ16(X_GRD,Y_GRD),BYQ16(X_GRD,Y_GRD)
REAL BXQ17(X_GRD,Y_GRD),BYQ17(X_GRD,Y_GRD)
REAL BXQ18(X_GRD,Y_GRD),BYQ18(X_GRD,Y_GRD)
REAL FACTOR
REAL S1,S2,S3,S4,S5,S6,S7,S8,S9
REAL F1,F2,F3,F4,F5,F6,F7,CLSP,F8,F9
S1=100.0    ! distance between simulation box and the solenoid
CLSP=0.1    ! Coil spacing
S2=S1+CLSP
```

```
S3=S2+CLSP
S4=S3+CLSP
S5=S4+CLSP
S6=S5+CLSP
S7=S6+CLSP
S8=S7+CLSP
S9=S8+CLSP
F1=S9
F2=F1+CLSP
F3=F2+CLSP
F4=F3+CLSP
F5=F4+CLSP
F6=F5+CLSP
F7=F6+CLSP
F8=F7+CLSP
F9=F8+CLSP
DX = 1
DY = 1
DO  J=1,NY
YY(J)=DY*FLOAT(J-1)
END DO
DO  I=1,NX
XX(I)=DX*FLOAT(I-1)
END DO
do J=1,NY
do I=1,NX
bzm(i,j)=0.0
bym(i,j)=0.0
bxm(i,j)=0.0
end do
end do
DO I=1,Y_DIM
DO J=1,Z_DIM
BYMC(I,J)=0.0
BXMC(I,J)=0.0
END DO
END DO
CALL COIL(S1)
DO I=1,Y_DIM
DO J=1,Z_DIM
BYQ1(I,J)=BYMC(I,J)
BXQ1(I,J)=BXMC(I,J)
END DO
END DO
CALL COIL(S2)
DO I=1,Y_DIM
```

```
DO J=1,Z_DIM
BYQ2(I,J)=BYMC(I,J)+BYQ1(I,J)
BXQ2(I,J)=BXMC(I,J)+BXQ1(I,J)
END DO
END DO
CALL COIL(S3)
DO I=1,Y_DIM
DO J=1,Z_DIM
BYQ3(I,J)=BYMC(I,J)+BYQ2(I,J)
BXQ3(I,J)=BXMC(I,J)+BXQ2(I,J)
END DO
END DO
CALL COIL(S4)
DO I=1,Y_DIM
DO J=1,Z_DIM
BYQ4(I,J)=BYMC(I,J)+BYQ3(I,J)
BXQ4(I,J)=BXMC(I,J)+BXQ3(I,J)
END DO
END DO
CALL COIL(S5)
DO I=1,Y_DIM
DO J=1,Z_DIM
BYQ5(I,J)=BYMC(I,J)+BYQ4(I,J)
BXQ5(I,J)=BXMC(I,J)+BXQ4(I,J)
END DO
END DO
CALL COIL(S6)
DO I=1,Y_DIM
DO J=1,Z_DIM
BYQ6(I,J)=BYMC(I,J)+BYQ5(I,J)
BXQ6(I,J)=BXMC(I,J)+BXQ5(I,J)
END DO
END DO
CALL COIL(S7)
DO I=1,Y_DIM
DO J=1,Z_DIM
BYQ7(I,J)=BYMC(I,J)+BYQ6(I,J)
BXQ7(I,J)=BXMC(I,J)+BXQ6(I,J)
END DO
END DO
CALL COIL(S8)
DO I=1,Y_DIM
DO J=1,Z_DIM
BYQ8(I,J)=BYMC(I,J)+BYQ7(I,J)
BXQ8(I,J)=BXMC(I,J)+BXQ7(I,J)
END DO
```

```
END DO
CALL COIL(S9)
DO I=1,Y_DIM
DO J=1,Z_DIM
BYQ9(I,J)=BYMC(I,J)+BYQ8(I,J)
BXQ9(I,J)=BXMC(I,J)+BXQ8(I,J)
END DO
END DO
CALL COIL(F1)
DO I=1,Y_DIM
DO J=1,Z_DIM
BYQ10(I,J)=BYMC(I,J)+BYQ9(I,J)
BXQ10(I,J)=BXMC(I,J)+BXQ9(I,J)
END DO
END DO
CALL COIL(F2)
DO I=1,Y_DIM
DO J=1,Z_DIM
BYQ11(I,J)=BYMC(I,J)+BYQ10(I,J)
BXQ11(I,J)=BXMC(I,J)+BXQ10(I,J)
END DO
END DO
CALL COIL(F3)
DO I=1,Y_DIM
DO J=1,Z_DIM
BYQ12(I,J)=BYMC(I,J)+BYQ11(I,J)
BXQ12(I,J)=BXMC(I,J)+BXQ11(I,J)
END DO
END DO
CALL COIL(F4)
DO I=1,Y_DIM
DO J=1,Z_DIM
BYQ13(I,J)=BYMC(I,J)+BYQ12(I,J)
BXQ13(I,J)=BXMC(I,J)+BXQ12(I,J)
END DO
END DO
CALL COIL(F5)
DO I=1,Y_DIM
DO J=1,Z_DIM
BYQ14(I,J)=BYMC(I,J)+BYQ13(I,J)
BXQ14(I,J)=BXMC(I,J)+BXQ13(I,J)
END DO
END DO
CALL COIL(F6)
DO I=1,Y_DIM
DO J=1,Z_DIM
```

```
BYQ15(I,J)=BYMC(I,J)+BYQ14(I,J)
BXQ15(I,J)=BXMC(I,J)+BXQ14(I,J)
END DO
END DO
CALL COIL(F7)
DO I=1,Y_DIM
DO J=1,Z_DIM
BYQ16(I,J)=BYMC(I,J)+BYQ15(I,J)
BXQ16(I,J)=BXMC(I,J)+BXQ15(I,J)
END DO
END DO
CALL COIL(F8)
DO I=1,Y_DIM
DO J=1,Z_DIM
BYQ17(I,J)=BYMC(I,J)+BYQ16(I,J)
BXQ17(I,J)=BXMC(I,J)+BXQ16(I,J)
END DO
END DO
CALL COIL(F9)
DO I=1,Y_DIM
DO J=1,Z_DIM
BYQ18(I,J)=BYMC(I,J)+BYQ17(I,J)
BXQ18(I,J)=BXMC(I,J)+BXQ17(I,J)
END DO
END DO
DO I=1,NX
DO J=1,NY
BYM(I,J)=BYQ17(I,J)
BXM(I,J)=BXQ17(I,J)
END DO
END DO
FACTOR=BYM(101,1)
DO I=1,NX
DO J=1,NY
BYM(I,J)=3.0*BYM(I,J)/FACTOR
BXM(I,J)=3.0*BXM(I,J)/FACTOR
END DO
END DO
RETURN
END
C    ***************************************************************
SUBROUTINE COIL (PARA)
C    ***************************************************************
INCLUDE 'bounds.h'
REAL ION
COMMON/PAR/ELE(NM_PRTS,5),ION(NM_PRTS,5)
```

```
COMMON/ARRAY1/PHI(X_GRD,Y_GRD)
COMMON/EFIELD/EX(X_GRD,Y_GRD),EY(X_GRD,Y_GRD)
COMMON/ARRAY/RHO(X_GRD,Y_GRD),RHOE(X_GRD,Y_GRD),
RHOI(X_GRD,Y_GRD)
COMMON/VEX/XX(X_GRD),YY(Y_GRD)
COMMON/TIM/ TIME,TPI,PI
COMMON/ANUM/ NX,NY,NX1,NY1,MAIN,NIJ,GAP1,GAP2,GD
COMMON/VARP/ RATO,DELT
COMMON/FLUXB/BZM(X_GRD,Y_GRD),BYM(X_GRD,Y_GRD),
BXM(X_GRD,Y_GRD),
&  BYMC(X_GRD,Y_GRD),BXMC(X_GRD,Y_GRD)
COMMON/AMIS/ ISEED,DY,DX,NIID,NEED,NSUME,NSUMI
COMMON/ANUM1/N_COIL,A,RADIUS
REAL BYC(X_GRD,Y_GRD),BZC(X_GRD,Y_GRD)
REAL  BXC(X_GRD,Y_GRD),Y2D(X_GRD,Y_GRD),Z2D(X_GRD,Y_GRD)
REAL PHIANG(N_COIL),XC(N_COIL),YC(N_COIL),RZ(N_COIL)
REAL RY(N_COIL),RX(N_COIL),DLX(N_COIL),DLY(N_COIL)
REAL XCROSS(N_COIL),YCROSS(N_COIL),ZCROSS(N_COIL)
REAL R(N_COIL),BXC1(N_COIL),BYC1(N_COIL),BZC1(N_COIL)
REAL YP(Y_DIM)
REAL ZP(Z_DIM)
INTEGER K,L
REAL PARA
PHIANG(1)=-PI/2.
RADIUS=66.  ! Radius of the coil
DO I=2,N_COIL
PHIANG(I)=PHIANG(I-1)+(2.*PI/(FLOAT(N_COIL-1)))
END DO
DO I=1,N_COIL
XC(I)=RADIUS*COS(PHIANG(I))
YC(I)=RADIUS*SIN(PHIANG(I))
RZ(I)=0.0
RY(I)=0.0
RX(I)=0.0
DLX(I)=0.0
DLY(I)=0.0
XCROSS(I)=0.0
YCROSS(I)=0.0
ZCROSS(I)=0.0
R(I)=0.0
END DO
DO I=1,Y_DIM
YP(I)=-FLOAT(NX1/2)+FLOAT(I-1)
END DO
DO I=1,Z_DIM
ZP(I)=FLOAT(I)-1.+PARA
```

```
END DO
DO I=1,Y_DIM
DO J=1,Z_DIM
Y2D(I,J)=0.0
Z2D(I,J)=0.0
END DO
END DO
DO I=1,Y_DIM
DO J=1,Z_DIM
Y2D(I,J)=YP(I)
END DO
END DO
DO I=1,Y_DIM
DO J=1,Z_DIM
Z2D(I,J)=ZP(J)
BXC(I,J)=0.0
BYC(I,J)=0.0
BZC(I,J)=0.0
BYMC(I,J)=0.0
BXMC(I,J)=0.0
END DO
END DO
CCCCCCCCCCCCCCCCCCCCCCCCCCCCCCCCCCCCCCCCCCCCCCCCCCCCC
DO 20 K=1,Y_DIM
DO 30 L=1,Z_DIM
CCCCCCCCCCCCCCCCCCCCC
DO I=1,N_COIL-1
RX(I)=-0.5*(XC(I)+XC(I+1))
RY(I)=(Y2D(K,L)-(0.5*(YC(I)+YC(I+1))))
RZ(I)=Z2D(K,L)
DLX(I)=XC(I+1)-XC(I)
DLY(I)=YC(I+1)-YC(I)
END DO
RX(N_COIL)=-0.5*(XC(N_COIL)+XC(1))
RY(N_COIL)=(Y2D(K,L)-(0.5*(YC(N_COIL)+YC(1))))
RZ(N_COIL)=Z2D(K,L)
DLX(N_COIL)=-XC(N_COIL)+XC(1)
DLY(N_COIL)=-YC(N_COIL)+YC(1)
DO I=1,N_COIL
XCROSS(I)=DLY(I)*RZ(I)
YCROSS(I)=-DLX(I)*RZ(I)
ZCROSS(I)=(DLX(I)*RY(I))-(DLY(I)*RX(I))
R(I)=SQRT(RX(I)**2+RY(I)**2+RZ(I)**2)
END DO
DO I=1,N_COIL
BXC1(I)=(1/(4*PI*(R(I)**3)))*XCROSS(I)
```

```
BYC1(I)=(1/(4*PI*(R(I)**3)))*YCROSS(I)
BZC1(I)=(1/(4*PI*(R(I)**3)))*ZCROSS(I)
END DO
BXC(K,L)=0.0
BYC(K,L)=0.0
BZC(K,L)=0.0
DO I=1,N_COIL
BXC(K,L)=BXC(K,L)+BXC1(I)
BYC(K,L)=BYC(K,L)+BYC1(I)
BZC(K,L)=BZC(K,L)+BZC1(I)
END DO
CCCCCCCCCCCCCCCCCCCCCCCCCCCCCCCCCCCCCCCCCCCCCCCCCCCCCCCCCCCCCCCCC
30      CONTINUE
20      CONTINUE
CCCCCCCCCCCCCCCCCCCCCCCCCCCCCCCCCCCCCCCCCCCCCCCCCCCCCCCCCCCCCCCCC
DO  I=1,Y_DIM
DO  J=1,Z_DIM
BYMC(I,J)=BZC(I,J)
BXMC(I,J)=BYC(I,J)
END DO
END DO
RETURN
END
CCCCCCCCCCCCCCCCCCCCCCCCCCCCCCCCCCCCCCCCCCCCCCCCCCCCCCCCCCCCCCCCC
SUBROUTINE INITIA
CCCCCCCCCCCCCCCCCCCCCCCCCCCCCCCCCCCCCCCCCCCCCCCCCCCCCCCCCCCCCCCCC
INCLUDE 'bounds.h'
REAL ION
COMMON/PAR/ELE(NM_PRTS,5),ION(NM_PRTS,5)
COMMON/ARRAY1/PHI(X_GRD,Y_GRD)
COMMON/EFIELD/EX(X_GRD,Y_GRD),EY(X_GRD,Y_GRD)
COMMON/ARRAY/RHO(X_GRD,Y_GRD),RHOE(X_GRD,Y_GRD),
RHOI(X_GRD,Y_GRD)
COMMON/VEX/XX(X_GRD),YY(Y_GRD)
COMMON/TIM/ TIME,TPI,PI
COMMON/ANUM/ NX,NY,NX1,NY1,MAIN,NIJ,GAP1,GAP2,GD
COMMON/VARP/ RATO,DELT
COMMON/FLUXB/BZM(X_GRD,Y_GRD),BYM(X_GRD,Y_GRD),
BXM(X_GRD,Y_GRD),
&  BYMC(X_GRD,Y_GRD),BXMC(X_GRD,Y_GRD)
COMMON/AMIS/ ISEED,DY,DX,NIID,NEED,NSUME,NSUMI
COMMON/ANUM1/N_COIL,A,Z_DIMA,Z_ACT,RADIUS
INTEGER NIN
C SIGMA FOR COLD E
SIGMA=1.
C  COLD IONS
```

```
SIGMA1=40.
VELMASS=1./RATO
VDRIFT=0.05
NIN=3000
NSUME = NEED
CCCCCCCCCCCCCCCCCCCCCCCCCCCCCCCCCCCCCCCCCCCCCCCCCCCCCCCCCCCCCCCCCCCC
C                  ELECTRONS
CCCCCCCCCCCCCCCCCCCCCCCCCCCCCCCCCCCCCCCCCCCCCCCCCCCCCCCCCCCCCCCCCCCC
DO 14 L=NEED+1,NEED+NIN
NSUME = NSUME + 1
ELE(L,1)= XX(NX)*RAN(ISEED)
ELE(L,2)= YY(NY)*RAN(ISEED)
VPAR = (1.414/SQRT(SIGMA))*SQRT(-LOG(1-RAN(ISEED)))
TPAR = TPI*RAN(ISEED)
ELE(L,3) = VPAR*SIN(TPAR)
VPAR = (1.414/SQRT(SIGMA))*SQRT(-LOG(1-RAN(ISEED)))
TPAR = TPI*RAN(ISEED)
ELE(L,4) =(VPAR*SIN(TPAR))
ELE(L,4)=ELE(L,4)
ELE(L,5) = VPAR*COS(TPAR)
ELE(L,2)=ELE(L,2)+DELT*ELE(L,4)
14     CONTINUE
NEED=NSUME
CCCCCCCCCCCCCCCCCCCCCCCCCCCCCCCCCCCCCCCCCCCCCCCCCCCCCCCCCCCCCCCCCCCC
C                    IONS
CCCCCCCCCCCCCCCCCCCCCCCCCCCCCCCCCCCCCCCCCCCCCCCCCCCCCCCCCCCCCCCCCCCC
NSUMI=NIID
DO 314 L=NIID+1,NIID+NIN
NSUMI = NSUMI + 1
ION(L,1)= XX(NX)*RAN(ISEED)
ION(L,2)= YY(NY)*RAN(ISEED)
VPAR = (1.414/SQRT(SIGMA1*VELMASS))*SQRT(-LOG(1-RAN(ISEED)))
TPAR = TPI*RAN(ISEED)
ION(L,3) = VPAR*SIN(TPAR)
VPAR = (1.414/SQRT(SIGMA1*VELMASS))*SQRT(-LOG(1-RAN(ISEED)))
TPAR = TPI*RAN(ISEED)
ION(L,4) = (VPAR*SIN(TPAR))+VDRIFT
ION(L,5) = VPAR*COS(TPAR)
ION(L,2)=ION(L,2)+DELT*ION(L,4)
314    CONTINUE
NIID=NSUMI
RETURN
END
CCCCCCCCCCCCCCCCCCCCCCCCCCCCCCCCCCCCCCCCCCCCCCCCCCCCCCCCCCCCCCCCCCCC
SUBROUTINE BEGIN
CCCCCCCCCCCCCCCCCCCCCCCCCCCCCCCCCCCCCCCCCCCCCCCCCCCCCCCCCCCCCCCCCCCC
```

```
INCLUDE 'bounds.h'
REAL ION
COMMON/PAR/ELE(NM_PRTS,5),ION(NM_PRTS,5)
COMMON/ARRAY1/PHI(X_GRD,Y_GRD)
COMMON/EFIELD/EX(X_GRD,Y_GRD),EY(X_GRD,Y_GRD)
COMMON/ARRAY/RHO(X_GRD,Y_GRD),RHOE(X_GRD,Y_GRD),
RHOI(X_GRD,Y_GRD)
COMMON/VEX/XX(X_GRD),YY(Y_GRD)
COMMON/TIM/ TIME,TPI,PI
COMMON/ANUM/ NX,NY,NX1,NY1,MAIN,NIJ,GAP1,GAP2,GD
COMMON/VARP/ RATO,DELT
COMMON/FLUXB/BZM(X_GRD,Y_GRD),BYM(X_GRD,Y_GRD),
BXM(X_GRD,Y_GRD),
&  BYMC(X_GRD,Y_GRD),BXMC(X_GRD,Y_GRD)
COMMON/AMIS/ ISEED,DY,DX,NIID,NEED,NSUME,NSUMI
COMMON/ANUM1/N_COIL,A,Z_DIMA,Z_ACT,RADIUS
C SIGMA FOR COLD E
SIGMA=1.
C  COLD IONS
SIGMA1=40.
VELMASS=1./RATO
VDRIFT=0.05
NINJC=100*GD
NSUME = NEED
CCCCCCCCCCCCCCCCCCCCCCCCCCCCCCCCCCCCCCCCCCCCCCCCCCCCCCCCCCCCCC
C                 ELECTRONS
CCCCCCCCCCCCCCCCCCCCCCCCCCCCCCCCCCCCCCCCCCCCCCCCCCCCCCCCCCCCCC
DO 14 L=NEED+1,NEED+NINJC
NSUME = NSUME + 1
ELE(L,1)= XX(GAP1)+(XX(GD)*RAN(ISEED))
ELE(L,2)= YY(1)+DY*RAN(ISEED)
VPAR = (1.414/SQRT(SIGMA))*SQRT(-LOG(1-RAN(ISEED)))
TPAR = TPI*RAN(ISEED)
ELE(L,3) = 0.0
VPAR = (1.414/SQRT(SIGMA))*SQRT(-LOG(1-RAN(ISEED)))
TPAR = TPI*RAN(ISEED)
ELE(L,4) =(VPAR*SIN(TPAR))
ELE(L,4)=ELE(L,4)
ELE(L,5) = 0.0
ELE(L,2)=ELE(L,2)+DELT*ELE(L,4)
14    CONTINUE
NEED=NSUME
CCCCCCCCCCCCCCCCCCCCCCCCCCCCCCCCCCCCCCCCCCCCCCCCCCCCCCCCCCCCCC
C                   IONS
CCCCCCCCCCCCCCCCCCCCCCCCCCCCCCCCCCCCCCCCCCCCCCCCCCCCCCCCCCCCCC
NSUMI=NIID
```

```
DO 314 L=NIID+1,NIID+NINJC
NSUMI = NSUMI + 1
ION(L,1)= XX(GAP1)+(XX(GD)*RAN(ISEED))
ION(L,2)= YY(1)+DY*RAN(ISEED)
VPAR = (1.414/SQRT(SIGMA1*VELMASS))*SQRT(-LOG(1-RAN(ISEED)))
TPAR = TPI*RAN(ISEED)
ION(L,3) = 0.0
VPAR = (1.414/SQRT(SIGMA1*VELMASS))*SQRT(-LOG(1-RAN(ISEED)))
TPAR = TPI*RAN(ISEED)
ION(L,4) = (VPAR*SIN(TPAR))+VDRIFT
ION(L,5) = 0.0
ION(L,2)=ION(L,2)+DELT*ION(L,4)
314    CONTINUE
NIID=NSUMI
RETURN
END
C ***************************************************************
SUBROUTINE DENS
C ***************************************************************
INCLUDE 'bounds.h'
REAL ION
INTEGER SIGR,SIGT
COMMON/PAR/ELE(NM_PRTS,5),ION(NM_PRTS,5)
COMMON/ARRAY1/PHI(X_GRD,Y_GRD)
COMMON/EFIELD/EX(X_GRD,Y_GRD),EY(X_GRD,Y_GRD)
COMMON/ARRAY/RHO(X_GRD,Y_GRD),RHOE(X_GRD,Y_GRD),
RHOI(X_GRD,Y_GRD)
COMMON/VEX/XX(X_GRD),YY(Y_GRD)
COMMON/TIM/ TIME,TPI,PI
COMMON/ANUM/ NX,NY,NX1,NY1,MAIN,NIJ
COMMON/VARP/ RATO,DELT
COMMON/FLUXB/BZM(X_GRD,Y_GRD),BYM(X_GRD,Y_GRD),
BXM(X_GRD,Y_GRD),
&  BYMC(X_GRD,Y_GRD),BXMC(X_GRD,Y_GRD)
COMMON/AMIS/ ISEED,DY,DX,NIID,NEED,NSUMI,NSUME
DIMENSION RHOEB(X_GRD,Y_GRD),RHOIB(X_GRD,Y_GRD)
COMMON/ANUM1/N_COIL,A,Z_DIMA,Z_ACT,RADIUS
DO  J=1,NY
DO  I=1,NX
RHOE(I,J)=0.0
RHOI(I,J)=0.0
RHO(I,J)=0.0
RHOEB(I,J)=0.0
RHOIB(I,J)=0.0
END DO
END DO
```

```
DO  L=1,NEED
NII=INT(ELE(L,2)/DY)+1
NJ=INT(ELE(L,1)/DX)+1
SIGR=+1
SIGT=+1
DELA=ABS(ELE(L,1)-XX(NJ))
DELB=ABS(ELE(L,2)-YY(NII))
A1=DELA*DELB
A2=DX*DELB-A1
A3=DY*DELA-A1
TOTA=DX*DY
A4=TOTA-(A1+A2+A3)
RHOEB(NJ+SIGR,NII+SIGT)=RHOEB(NJ+SIGR,NII+SIGT)+A1/TOTA
RHOEB(NJ,NII+SIGT)=RHOEB(NJ,NII+SIGT)+A2/TOTA
RHOEB(NJ+SIGR,NII)=RHOEB(NJ+SIGR,NII)+A3/TOTA
RHOEB(NJ,NII)=RHOEB(NJ,NII)+A4/TOTA
END DO
DO  L=1,NIID
NII=INT(ION(L,2)/DY)+1
NJ=INT(ION(L,1)/DX)+1
SIGR=+1
SIGT=+1
DELA=ABS(ION(L,1)-XX(NJ))
DELB=ABS(ION(L,2)-YY(NII))
A1=DELA*DELB
A2=DX*DELB-A1
A3=DY*DELA-A1
TOTA=DX*DY
A4=TOTA-(A1+A2+A3)
RHOIB(NJ+SIGR,NII+SIGT)=RHOIB(NJ+SIGR,NII+SIGT)+A1/TOTA
RHOIB(NJ,NII+SIGT)=RHOIB(NJ,NII+SIGT)+A2/TOTA
RHOIB(NJ+SIGR,NII)=RHOIB(NJ+SIGR,NII)+A3/TOTA
RHOIB(NJ,NII)=RHOIB(NJ,NII)+A4/TOTA
END DO
NIJE=NIJ
DO  J=1,NY
DO  I=1,NX
RHOIB(I,J)=RHOIB(I,J)/NIJE
RHOEB(I,J)=RHOEB(I,J)/NIJE
END DO
END DO
DO  J=1,NY
DO  I=1,NX
RHOI(I,J)=RHOIB(I,J)
RHOE(I,J)=RHOEB(I,J)
END DO
```

```
END DO
DO  J=1,NY
DO  I=1,NX
RHO(I,J)= RHOI(I,J)-RHOE(I,J)
END DO
END DO
C     NEW BOUNDARY CONDITION TO UNMASK ELECTRIC FIELD
DO I=1,NX
RHO(I,1)=-RHO(I,2)
END DO
RETURN
END
C    ***************************************************************
SUBROUTINE FIELD
C   ***************************************************************
INCLUDE 'bounds.h'
REAL ION
COMMON/PAR/ELE(NM_PRTS,5),ION(NM_PRTS,5)
COMMON/ARRAY1/PHI(X_GRD,Y_GRD)
COMMON/EFIELD/EX(X_GRD,Y_GRD),EY(X_GRD,Y_GRD)
COMMON/ARRAY/RHO(X_GRD,Y_GRD),RHOE(X_GRD,Y_GRD),
RHOI(X_GRD,Y_GRD)
COMMON/VEX/XX(X_GRD),YY(Y_GRD)
COMMON/TIM/ TIME,TPI,PI
COMMON/ANUM/ NX,NY,NX1,NY1,MAIN,NIJ
COMMON/VARP/ RATO,DELT
COMMON/FLUXB/BZM(X_GRD,Y_GRD),BYM(X_GRD,Y_GRD),
BXM(X_GRD,Y_GRD),
&  BYMC(X_GRD,Y_GRD),BXMC(X_GRD,Y_GRD)
COMMON/AMIS/ ISEED,DY,DX,NIID,NEED,NSUMI,NSUME
COMMON/ANUM1/N_COIL,A,Z_DIMA,Z_ACT,RADIUS
DO  J=2,NY1
DO  I=1,NX
EY(I,J)=-(PHI(I,J+1)-PHI(I,J-1))/(2.0*DY)
END DO
END DO
DO  J=1,NY
DO  I=2,NX1
EX(I,J)=-(PHI(I+1,J)-PHI(I-1,J))/(2.0*DX)
END DO
END DO
DO  J=1,NY
EX(1,J)=-(PHI(2,J)-PHI(1,J))/DX
EX(NX,J)=-(PHI(NX,J)-PHI(NX1,J))/DX
END DO
C   NEW BOUNDARY CONDITION TO UNMASK ELECTRIC FIELD
```

```
DO I=1,NX
EY(I,1)=RHO(I,1)
EY(I,NY)=-(PHI(I,NY)-PHI(I,NY1))/DY
END DO
RETURN
END
C*************************************************************
SUBROUTINE MOVEI
C*************************************************************
INCLUDE 'bounds.h'
REAL ION
INTEGER SIGT,SIGR
COMMON/PAR/ELE(NM_PRTS,5),ION(NM_PRTS,5)
COMMON/ARRAY1/PHI(X_GRD,Y_GRD)
COMMON/EFIELD/EX(X_GRD,Y_GRD),EY(X_GRD,Y_GRD)
COMMON/ARRAY/RHO(X_GRD,Y_GRD),RHOE(X_GRD,Y_GRD),
RHOI(X_GRD,Y_GRD)
COMMON/VEX/XX(X_GRD),YY(Y_GRD)
COMMON/TIM/TIME,TPI,PI
COMMON/ANUM/NX,NY,NX1,NY1,MAIN,NIJ,GAP1,GAP2,GD
COMMON/VARP/ RATO,DELT
COMMON/FLUXB/BZM(X_GRD,Y_GRD),BYM(X_GRD,Y_GRD),
BXM(X_GRD,Y_GRD),
&  BYMC(X_GRD,Y_GRD),BXMC(X_GRD,Y_GRD)
COMMON/AMIS/ISEED,DY,DX,NIID,NEED,NSUMO
COMMON/ANUM1/N_COIL,A,Z_DIMA,Z_ACT,RADIUS
REAL A(3,3),B(3),X(3)
DO 1 L=1,NIID
NII=INT(ION(L,2)/DY)+1
NJ=INT((ION(L,1))/DX)+1
SIGR=+1.
SIGT=+1.
DELA=ABS(ION(L,1)-XX(NJ))
DELB=ABS(ION(L,2)-YY(NII))
A1=DELA*DELB
A2=DX*DELB-A1
A3=DY*DELA-A1
A4=DX*DY-(A1+A2+A3)
TOTA=DX*DY
EXPF=(A1*EX(NJ+SIGR,NII+SIGT)+A2*EX(NJ,NII+SIGT)+
>         A3*EX(NJ+SIGR,NII)+A4*EX(NJ,NII))/TOTA
EYPF=(A1*EY(NJ+SIGR,NII+SIGT)+A2*EY(NJ,NII+SIGT)+
>         A3*EY(NJ+SIGR,NII)+A4*EY(NJ,NII))/TOTA
BYPF=(A1*BYM(NJ+SIGR,NII+SIGT)+A2*BYM(NJ,NII+SIGT)+
&        A3*BYM(NJ+SIGR,NII)+A4*BYM(NJ,NII))/TOTA
BXPF=A1*BXM(NJ+SIGR,NII+SIGT)+A2*BXM(NJ,NII+SIGT)+
```

```
&       A3*BXM(NJ+SIGR,NII)+A4*BXM(NJ,NII)/TOTA
RAT=RATO
C1=DELT*RAT
P=.5
C2=1-P
C3=C1*P
C4=C1*C2
BXM1=BXPF
BYM1=BYPF
BZM1=0.0
A(1,1) = 1.
A(1,2) = -C3*BZM1
A(1,3) = C3*BYM1
A(2,1) = C3*BZM1
A(2,2) = 1.
A(2,3) = -C3*BXM1
A(3,1) = -C3*BYM1
A(3,2) = C3*BXM1
A(3,3) = 1.
B(1)=ION(L,3) + ION(L,4)*C4*BZM1 - ION(L,5)*C4*BYM1
&           + C1*EXPF
B(2)=ION(L,4) + ION(L,5)*C4*BXM1 - ION(L,3)*C4*BZM1
&           + C1*EYPF
B(3)=ION(L,5) + ION(L,3)*C4*BYM1 - ION(L,4)*C4*BXM1
DET=A(1,1)*(A(2,2)*A(3,3) - A(2,3)*A(3,2))-
&         A(1,2)*(A(2,1)*A(3,3) - A(2,3)*A(3,1))+
&         A(1,3)*(A(2,1)*A(3,2) - A(2,2)*A(3,1))
DET1=B(1)*(A(2,2)*A(3,3) - A(2,3)*A(3,2))-
&         A(1,2)*(B(2)*A(3,3) - B(3)*A(2,3))+
&         A(1,3)*(B(2)*A(3,2) - B(3)*A(2,2))
DET2=A(1,1)*(B(2)*A(3,3) - B(3)*A(2,3))-
&         B(1)*(A(2,1)*A(3,3) - A(2,3)*A(3,1))+
&         A(1,3)*(B(3)*A(2,1) - B(2)*A(3,1))
DET3=A(1,1)*(A(2,2)*B(3) - B(2)*A(3,2))-
&         A(1,2)*(A(2,1)*B(3) - B(2)*A(3,1))+
&         B(1)*(A(2,1)*A(3,2) - A(2,2)*A(3,1))
ION(L,3)=DET1/DET
ION(L,4)=DET2/DET
ION(L,5)=DET3/DET
ION(L,1)=ION(L,1)+ION(L,3)*DELT
ION(L,2)=ION(L,2)+ION(L,4)*DELT
1     CONTINUE
DO  L=1,3000
IF(ION(L,2) .GT. YY(NY))THEN
ION(L,2) = YY(NY)
ION(L,4)=-ION(L,4)
```

```
ION(L,2) = ION(L,2)+ION(L,4)*DELT
ENDIF
IF(ION(L,2) .LT. YY(1))THEN
ION(L,2) = YY(1)
ION(L,4)=-ION(L,4)
ION(L,2) = ION(L,2)+ION(L,4)*DELT
ENDIF
IF(ION(L,1) .GT. XX(NX))THEN
ION(L,1) = XX(NX)
ION(L,3)=-ION(L,3)
ION(L,1) = ION(L,1)+ION(L,3)*DELT
ENDIF
IF(ION(L,1) .LT. XX(1) )THEN
ION(L,1) = XX(1)
ION(L,3)=-ION(L,3)
ION(L,1) = ION(L,1)+ION(L,3)*DELT
ENDIF
END DO
LI1=0
DO 111 L=3001,NIID
IF((ION(L,1) .GT. XX(NX)) .OR. (ION(L,1) .LT.XX(1)))GO TO 111
LI1 = LI1+1
DO 194 JA=1,5
ION(LI1+3000,JA) = ION(L,JA)
194      CONTINUE
111    CONTINUE
LI2 = 0
DO 93 L=3001,LI1+3000
IF((ION(L,2) .GT. YY(NY)) .OR. (ION(L,2) .LT.YY(2)))GO TO 93
LI2 = LI2+1
DO 94 JA=1,5
ION(LI2+3000,JA) = ION(L,JA)
94       CONTINUE
93    CONTINUE
NIID=LI2+3000
RETURN
END
C ***************************************************************
SUBROUTINE MOVEE
C ***************************************************************
INCLUDE 'bounds.h'
REAL ION
INTEGER SIGT,SIGR
COMMON/PAR/ELE(NM_PRTS,5),ION(NM_PRTS,5)
COMMON/ARRAY1/PHI(X_GRD,Y_GRD)
COMMON/EFIELD/EX(X_GRD,Y_GRD),EY(X_GRD,Y_GRD)
```

```
COMMON/ARRAY/RHO(X_GRD,Y_GRD),RHOE(X_GRD,Y_GRD),
RHOI(X_GRD,Y_GRD)
COMMON/VEX/XX(X_GRD),YY(Y_GRD)
COMMON/TIM/ TIME,TPI,PI
COMMON/ANUM/ NX,NY,NX1,NY1,MAIN,NIJ
COMMON/VARP/ RATO,DELT
COMMON/FLUXB/BZM(X_GRD,Y_GRD),BYM(X_GRD,Y_GRD),
BXM(X_GRD,Y_GRD),
&  BYMC(X_GRD,Y_GRD),BXMC(X_GRD,Y_GRD)
COMMON/AMIS/ ISEED,DY,DX,NIID,NEED,NSUMO
COMMON/ANUM1/N_COIL,A,Z_DIMA,Z_ACT,RADIUS
REAL A(3,3),B(3),X(3)
DO 1 L=1,NEED
NII=INT(ELE(L,2)/DY)+1
NJ=INT((ELE(L,1))/DX)+1
SIGR=+1.
SIGT=+1.
DELA=ABS(ELE(L,1)-XX(NJ))
DELB=ABS(ELE(L,2)-YY(NII))
A1=DELA*DELB
A2=DX*DELB-A1
A3=DY*DELA-A1
A4=DX*DY-(A1+A2+A3)
TOTA=DX*DY
EXPF=(A1*EX(NJ+SIGR,NII+SIGT)+A2*EX(NJ,NII+SIGT)+
>         A3*EX(NJ+SIGR,NII)+A4*EX(NJ,NII))/TOTA
EYPF=(A1*EY(NJ+SIGR,NII+SIGT)+A2*EY(NJ,NII+SIGT)+
>         A3*EY(NJ+SIGR,NII)+A4*EY(NJ,NII))/TOTA
BYPF=(A1*BYM(NJ+SIGR,NII+SIGT)+A2*BYM(NJ,NII+SIGT)+
&        A3*BYM(NJ+SIGR,NII)+A4*BYM(NJ,NII))/TOTA
BXPF=A1*BXM(NJ+SIGR,NII+SIGT)+A2*BXM(NJ,NII+SIGT)+
&        A3*BXM(NJ+SIGR,NII)+A4*BXM(NJ,NII)/TOTA
C---------------------------------------------------------------
C1=-DELT
P=.5
C2=1-P
C3=C1*P
C4=C1*C2
BXM1=BXPF
BYM1=BYPF
BZM1=0.0
A(1,1) = 1.
A(1,2) = -C3*BZM1
A(1,3) = C3*BYM1
A(2,1) = C3*BZM1
A(2,2) = 1.
```

```
A(2,3) = -C3*BXM1
A(3,1) = -C3*BYM1
A(3,2) = C3*BXM1
A(3,3) = 1.
B(1)=ELE(L,3) + ELE(L,4)*C4*BZM1 - ELE(L,5)*C4*BYM1
&          + C1*EXPF
B(2)=ELE(L,4) + ELE(L,5)*C4*BXM1 - ELE(L,3)*C4*BZM1
&          + C1*EYPF
B(3)=ELE(L,5) + ELE(L,3)*C4*BYM1 - ELE(L,4)*C4*BXM1
DET=A(1,1)*(A(2,2)*A(3,3) - A(2,3)*A(3,2))-
&         A(1,2)*(A(2,1)*A(3,3) - A(2,3)*A(3,1))+
&         A(1,3)*(A(2,1)*A(3,2) - A(2,2)*A(3,1))
DET1=B(1)*(A(2,2)*A(3,3) - A(2,3)*A(3,2))-
&         A(1,2)*(B(2)*A(3,3) - B(3)*A(2,3))+
&         A(1,3)*(B(2)*A(3,2) - B(3)*A(2,2))
DET2=A(1,1)*(B(2)*A(3,3) - B(3)*A(2,3))-
&         B(1)*(A(2,1)*A(3,3) - A(2,3)*A(3,1))+
&         A(1,3)*(B(3)*A(2,1) - B(2)*A(3,1))
DET3=A(1,1)*(A(2,2)*B(3) - B(2)*A(3,2))-
&         A(1,2)*(A(2,1)*B(3) - B(2)*A(3,1))+
&         B(1)*(A(2,1)*A(3,2) - A(2,2)*A(3,1))
ELE(L,3)=DET1/DET
ELE(L,4)=DET2/DET
ELE(L,5)=DET3/DET
C-----------------------------------------------------------------
ELE(L,1)=ELE(L,1)+ELE(L,3)*DELT
ELE(L,2)=ELE(L,2)+ELE(L,4)*DELT
1     CONTINUE
DO  L=1,3000
IF(ELE(L,2) .GT. YY(NY))THEN
ELE(L,2) = YY(NY)
ELE(L,4)=-ELE(L,4)
ELE(L,2) = ELE(L,2)+ELE(L,4)*DELT
ENDIF
IF(ELE(L,2) .LT. YY(1))THEN
ELE(L,2) = YY(1)
ELE(L,4)=-ELE(L,4)
ELE(L,2) = ELE(L,2)+ELE(L,4)*DELT
ENDIF
IF(ELE(L,1) .GT. XX(NX))THEN
ELE(L,1) = XX(NX)
ELE(L,3)=-ELE(L,3)
ELE(L,1) = ELE(L,1)+ELE(L,3)*DELT
ENDIF
IF(ELE(L,1) .LT. XX(1) )THEN
ELE(L,1) = XX(1)
```

```
ELE(L,3)=-ELE(L,3)
ELE(L,1) = ELE(L,1)+ELE(L,3)*DELT
ENDIF
END DO
LI3=0
DO 1111 L=3001,NEED
IF((ELE(L,1) .GT. XX(NX)) .OR. (ELE(L,1) .LT.XX(1)))GO TO 1111
LI3 = LI3+1
DO 1941 JA=1,5
ELE(LI3+3000,JA) = ELE(L,JA)
1941      CONTINUE
1111    CONTINUE
LI4 = 0
DO 931 L=3001,LI3+3000
IF((ELE(L,2) .GT. YY(NY)) .OR. (ELE(L,2) .LT.YY(2)))GO TO 931
LI4 = LI4+1
DO 941 JA=1,5
ELE(LI4+3000,JA) = ELE(L,JA)
941      CONTINUE
931    CONTINUE
NEED=LI4+3000
RETURN
END
CCCCCCCCCCCCCCCCCCCCCCCCCCCCCCCCCCCCCCCCCCCCCCCCCCCCCCCCCCCCCCC
C              SUBROUTINE POISSON
CCCCCCCCCCCCCCCCCCCCCCCCCCCCCCCCCCCCCCCCCCCCCCCCCCCCCCCCCCCCCCC
INCLUDE 'bounds.h'
REAL ION
COMMON/PAR/ELE(NM_PRTS,5),ION(NM_PRTS,5)
COMMON/ARRAY1/PHI(X_GRD,Y_GRD)
COMMON/EFIELD/EX(X_GRD,Y_GRD),EY(X_GRD,Y_GRD)
COMMON/ARRAY/RHO(X_GRD,Y_GRD),RHOE(X_GRD,Y_GRD),
RHOI(X_GRD,Y_GRD)
COMMON/VEX/XX(X_GRD),YY(Y_GRD)
COMMON/TIM/ TIME,TPI,PI
COMMON/ANUM/ NX,NY,NX1,NY1,MAIN,NIJ,GAP1,GAP2,GD
COMMON/VARP/ RATO,DELT
COMMON/FLUXB/BZM(X_GRD,Y_GRD),BYM(X_GRD,Y_GRD),
BXM(X_GRD,Y_GRD),
&  BYMC(X_GRD,Y_GRD),BXMC(X_GRD,Y_GRD)
COMMON/AMIS/ ISEED,DY,DX,NIED,NSUMI,NSUME
COMMON/ANUM1/N_COIL,A,Z_DIMA,Z_ACT,RADIUS
REAL T,W,W4,RMIN,RPHI
INTEGER NCOUNT
C    SET THE INITIAL GUESS EQUAL TO ZERO
DO I=1,NX
```

```
DO J=1,NY
PHI(I,J)=0.0
END DO
END DO
C     FIND THE OPTIMUM OVER RELAXATION FACTOR
PI=3.14159265358979
T=COS(PI/NX)+COS(PI/NY)
W=(8.0-SQRT(64.0- 16.0*T*T))/(T*T)
W4=W/4.0
C     ITERATION BEGINS
NCOUNT=0
DO U=1,4000
RMIN=0.0
NCOUNT=NCOUNT+1
DO I=2,NX1
DO J=2,NY1
RPHI=W4*(PHI(I+1,J)+PHI(I-1,J)+PHI(I,J+1)+PHI(I,J-1)
&       -4.0*PHI(I,J)+RHO(I,J))
RMIN=RMIN+ABS(RPHI)
PHI(I,J)=PHI(I,J)+RPHI
END DO
END DO
DO I=GAP1,GAP2
PHI(I,1)=PHI(I,2)+EY(I,1)
END DO
END DO
RL=RMIN/FLOAT(NX*NY)
CONTINUE
RETURN
END
C-------------------------------------------------------------------------------------------
C--To run on altix use "ifort -o somename.o fortranfilename.f -O3"
C--To run on DMC use
C "ifort -o somename.o fortranfilename.f -mcmodel=medium -shared-intel"
C-------------------------------------------------------------------------------------------
C       bounds.h file
C       PARAMETER (NM_PRTS=989096000)
C      PARAMETER(X_GRD=201,Y_GRD=201)
C      PARAMETER(Z_DIM=201,Y_DIM=201)
```

APPENDIX B

ELECTRON ENERGY DISTRIBUTION M-FILE

```
%-------------------------------------------------------------------
%---Electron energy calculation-------------------------------------
%-------------------------------------------------------------------
clc; close all; clear all
p1=importdata('J:\finalrun\data\ele__0064');
nobin=500; % number of bins in kinetic energy
X=p1(:,1)-100;
Y=p1(:,2);
VX=p1(:,3);
VY=p1(:,4);
VZ=p1(:,5);
V=sqrt((VX).^2+(VY).^2+(VZ).^2);
%-------------------------------------------------------------------
 KE=0.5.*(V.^2);
 Mn=min(KE);
 Mx=max(KE);
 LL=(abs(Mn)+abs(Mx))/nobin;
 %-------------------------------------------------------------------
%---BINNING PROCESS FOR KE AS IN THE IF LOOP---
%-------------------------------------------------------------------
vmid=0;
for o=1:nobin
FF=o-1;
num=1;
for i=1:length(KE)
        if((X(i)>=-20 && X(i)<=20))
         if((Y(i)>=170 && Y(i)<=190))
       if(KE(i)>=Mn+(FF*LL) && KE(i)<=Mn+(FF*LL)+LL)
        vmid=((Mn+(FF*LL))+(Mn+(FF*LL)+LL))/2;
        num=num+1;
       end
       end
       end
end
NP(o)=num-1;
ke(o)=vmid;
end
 K=0;
for i=1:nobin-1
```

```
   if ( NP(i)~=1.0 && NP(i)~=0.0 )
      K=K+1;
      NPnew(K)=NP(i);
      kenew(K)=ke(i);
   end
end
NPnew=NPnew./((max(ke)/nobin));
L=1;
M=length(NPnew);
%--------------------------------------------------------------------
Npnew=smooth(NPnew,'moving',6);
figure(1)
plot(kenew(L:M),log10(20.*Npnew(L:M)),'linewidth',2)
h=gca; % returns handle to current axis in the current
get(h,'FontSize') % displays the default Font size
set(h,'FontSize',12)
Xlabel('KE','fontsize',12)
Ylabel('log_{10}(N_e)','fontSize',12)
grid on
fh = figure(1); % returns the handle to the figure oject
set(fh, 'color', 'white'); % sets the color to white
```

REFERENCES

[1] N. Singh, "Current-free double layers: A review", Physics of plasmas, Vol. 18, 2011.

[2] N. Singh, "Comment on Oblique double layers: A Comparison between Terrestrial and Auroral measurements", Physical Review Letters, Vol. 106, 2011.

[3] C. Charles, "High density conics in a magnetically expanding helicon plasma", Applied Physics Letter, Vol. 96, 2010.

[4] C. Charles and R. W. Boswell, "Current-free double-layer formation in a high-density helicon discharge", Applied Physics Letter, Vol. 82, 2003.

[5] C. Charles, "Operating the helicon double layer thruster in a space simulation chamber", IEEE transactions on plasma science, Vol. 36, No. 4, August 2008.

[6] E. E. Scime, I. A. Biloiu, J. Carr, Jr., S. C. Thakur, M. Galante, A. Hansen, S. Houshmandyar, A. M. Keesee, D. McCarren, S. Sears, C. Biloiu, and X. Sun, " Time – resolved measurement of double layer evolution in expanding plasma" , Physics of Plasmas , Vol. 17, Issue 5, 2010.

[7] N. Plihon, P. Chabert, and C. S. Corr, "Experimental investigation of double layer in expanding plasmas" , Physics of Plasmas , Vol. 14, Issue 1, 2007.

[8] C. Charles and R. W. Boswell**, "**Effect of Exhaust Magnetic Field in a Helicon Double-Layer Thruster Operating in Xenon", IEEE transactions on plasma science, Vol. 36, p2141-2146, Oct 2008.

[9] E. Ahedo, P. Martinez-Cerezo, and M. Martinez-Sanchez, " One-dimensional model of the plasma flow in a hall thruster" , Physics of Plasmas, Vol. 8, Issue 6, 2001.

[10] C. Charles and R. W. Boswell, “Laboratory evidence of a supersonic ion beam generated by a current-free helicon double-layer”, Physics of Plasmas, Vol. 11, Issue 4, 2004.

[11] Francis F. Chen, “Physical mechanism of current free double layers”, Physics of Plasmas, Vol. 13, Issue 3, 2006.

[12] A. Meige and R. W. Boswell, “Electron energy distribution functions in low-pressure inductively coupled bounded plasmas”, Physics of Plasmas, Vol. 13, Issue 9, 2006.

[13] A. Meige, R. W. Boswell, C. Charles, Jean-Pierre Boeuf, G. Hagelaar, and M. M. Turner, “One-Dimensional Simulation of an Ion Beam Generated by a Current-Free Double-Layer**”,** IEEE transactions on plasma science, Vol. 33, NO. 2, April 2005.

[14] C. Charles, R. W. Boswell and R. Hawkins, “Oblique double layers: A Comparison between Terrestrial and Auroral measurements”, Physical Review Letter, Vol. 103, Issue 9, 2009.

[15] F. F. Chen, “Introduction to plasma physics and controlled fusion”, Plenum press, New York, 1984.

[16] H. Alfven, “On the theory of magnetic storms and aurorae”, Tellus, Vol. 10, Issue 1, p104–116, 1958.

[17] J. G. Andrews and J. E. Allen, “ Theory of a double sheath between Two Plasmas”, Proceedings of the Royal Society A, Vol. 320, No. 1543, 1971.

[18] M. A. Lieberman and C. Charles, “Theory for Formation of a Low-Pressure Current -Free Double Layer”, Physical Review Letters, Vol. 97, Issue 4, 2006.

[19] M. N. O. Sadiku, Numerical Techniques in Electromagnetics, Boca Raton, FL, CRC Press, 1993.

[20] N. Plihon, P. Chabert, and C. S. Corr, "Experimental investigation of double layers in expanding plasmas", Physics of Plasmas, Vol. 17, Issue 1, 2007.

[21] S. D. Baalrud, T. Lafleur, R. W. Boswell, and C. Charles, "Particle-in-cell simulations of a current-free double layer", Physics of Plasmas, Vol. 18, Issue 6, 2011.

[22] N. Singh and R. Schunk , "Numerical Calculations Relevant to the Initial Expansion of the Polar Wind" , Journal of Geophysical Research, Vol. 87, No. A11, PP. 9154-9170, 1982.

[23] C. K. Birdsall and A. B. Langdon, 1985 *Plasma Physics via Computer Simulation* (New York: McGraw-Hill).

[24] J P Verboncoeur, Particle simulation of plasmas: review and advances, 2005 *Plasma Phys. Control. Fusion* 47 A231.

[25] S. Rao and N. Singh, "Numerical Simulation of Current Free Double Layers created in a Helicon Plasma Device", submitted for publication.